Universidade de Aveiro Departamento de Física,
2017

Alexandre Pombo

Espectroscopia de "Q-balls" e construção de estrelas de bosões

Q-ball spectroscopy and construction of boson stars

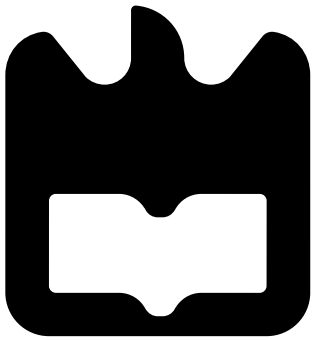

Alexandre Pombo

Espectroscopia de "Q-balls" e construção de estrelas de bosões

Q-ball spectroscopy and construction of boson stars

Dissertação apresentada à Universidade de Aveiro para cumprimento dos requesitos necessários à obteção do grau de Mestre em Mestrado em Física, realizada sob orientação científica do Prof. Dr. Carlos Alberto Ruivo Herdeiro, Investigador Principal do Departamento de Física da Universidade de Aveiro, e Dr. Eugen Radu, Investigador Principal de Física da Universidade de Aveiro.

O Júri / The jury

Presidente / President

Vitor Hugo da Rosa Bonifácio
Professor Auxiliar do Departamento de Física da Universidade de Aveiro

Vogais / Committee

Yves Brihaye
Professor de Física Teórica e Matemática da Universidade de Mons, Bélgica (examinador)

Carlos Alberto Ruivo Herdeiro
Professor Auxiliar com Agregação, equiparado a investigador principal (orientador)

Agradecimentos / Acknowledgements

Em primeiro lugar, queria agradecer ao meu orientador Prof. Dr. Carlos Herdeiro pela oportunidade de realizar o projecto de Mestrado nesta área sob a sua orientação científica, e pela paciência e disponibilidade apresentada. Queria ainda agradecer ao Dr. Eugen Radu pela orientação científica bem como pelo apoio técnico.
Ao Prof. Ricardo Dias e ao Prof. Manuel Barroso pelo suporte e orientação durante todo o curso de mestrado, bem como durante a licenciatura.
À Ema Valente por todo o carinho e apoio, fazendo-me uma pessoa melhor todos os dias. Mas acima de tudo, obrigado aos meus pais por me proporcionarem e apoiarem nesta aventura.

Resumo

Na ausência de efeitos gravitacionais, a dispersão da equação linear de Klein-Gordon pode ser contrabalançada pela introdução de auto-interações não-lineares do campo escalar. Quando ocorre o cancelamento de efeitos não lineares e dispersivos, ocorrem pacotes auto-reforçadas de ondas solitárias. Quando um único campo escalar complexo produz soluções solitónicas, eles são conhecidos como Q-balls. O tipo mais genérico de Q-balls possui uma rotação e uma carga elétrica e são denominados "gauged, spinning Q-balls".

Nesta tese, após uma breve introdução do modelo e algumas propriedades físicas e assintóticas, um método espectroscópico para decompor os vários campos das Q-ball é introduzido e os vários modos obtidos a partir dele são analisados. De modo a analisar estes, algumas quantidades físicas são estudadas e comparadas entre as diferentes soluções de parâmetros de Q-ball.

Numa segunda parte, consideraremos a existência de objetos bosónicos na presença de efeitos gravitacionais. A existência de "bolhas" localizadas, aproximadamente estacionárias, do campo gravitacional e eletromagnético clássico – geons – foi conjeturada há mais de meio século. Se se insistir em soluções estáticas, as configurações topologicamente triviais no eletro-vácuo são descartadas por teoremas de não-retorno para solitões. Mas os conceitos estacionários e assintoticamente planos de geons encontraram uma solução no vácuo escalar, onde podem existir "bolhas" de campo escalar localizados conhecidos como estrelas do bosões (escalares).

Nesta tese, um método de Runge-Kutta de quarta ordem, com uma rotina de shooting, foi implementado para obter o diagrama de fase para obter uma estrela de bosões no estado fundamental, bem como uma única solução para um estado excitado. Analisamos então o diagrama de fases obtido e algumas quantidades físicas obtidas a partir dele.

Abstract

In the absence of gravitational effects, the dispersiveness of the linear Klein-Gordon equation can be counter-balanced by introducing non-linear self-interactions of the scalar field. When cancellation of non-linear and dispersive effects occurs, self-reinforcing solitary wave packets emerge. If this solitary wave packets are formed by a single complex scalar field, a Q-ball is formed. The most generic type of Q-balls, known as gauged spinning Q-balls, possess a spinning phase and an electrical charge.

In this thesis, after a brief introduction of the model and some physical and asymptotical properties of Q-ball solutions, a spectroscopic method to decompose the several Q-ball fields is introduced, and used to obtained, and analise the latter's. To perform the spectroscopic analises and compare between the possible Q-ball solutions, some physical quantities – namely the electrical charge, Noether charge, energy, gyromagnetic factor and magnetic dipole moment – are retrieved.

In a second part, the existence of bosonic objects in the presence of gravitational effects is going to be considered. The existence of localized, approximately stationary, lumps of the classical gravitational and electromagnetic field – geons – was conjectured more than half a century ago. If one insists on exact stationarity, topologically trivial configurations in electro-vacuum are ruled out by no-go theorems for solitons. But stationary, asymptotically flat geons found a realization in scalar-vacuum, where everywhere non-singular, localized field lumps exist, known as (scalar) boson stars.

To numerically obtain the boson star solutions, a four order Runge-Kutta method with a shooting routine was implemented. With it, the phase parameter diagram for the fundamental state and single excited state, are obtained. We then analise the obtained phase diagram, study the different branches and some physical quantities.

Contents

List of Figures

List of Tables

Chapter 1

Introduction

In 1609 Galileu pointed his telescope for the first time at the night sky, opening a wonderful new window for the Human understanding. What he did not know, was that all the magnificent objects that where seen only account for $\sim 4.9\%$ of all the matter-energy content in our Universe.

In quantum mechanics there is an intrinsic property of quantum particles: their intrinsic angular momentum or *spin*. Its value divides particles into two groups: the fermions, with half integer spin, and the bosons, with integer spin.

While bosons follow the Bose-Einstein statistic, that does not restrict the occupation number of a given state, fermions follow the Fermi-Dirac statistic and obey the Pauli exclusion principle. At a given time, there can only be one fermion in a given quantum state. For the boson case, since they can occupy the same quantum state, they can bunch together creating lumps of coherent matter: *Bose-Einstein condensates*.

In particle physics, while the classical matter (quarks and leptons) are fermions, the force carriers (photons, gluons, ...), as well as the Higgs particle, are bosons. In the observable universe, every known astrophysical object is composed by fermions. Hypothetical structures, on the other hand, composed of bosons have been theoretically suggested, the simplest of which are *Q-balls* and *boson stars*. These are compatible with current observations as long as they only interact weakly with electromagnetic radiation, therefore, being dark matter.

In this dissertation our main objective will be to investigate such hypothetical bosonic objects. In the first chapter the Q-ball case will be considered. Q-balls consist of a large number of boson held together by non-linear self-interactions. In this chapter a set of solutions will be obtained, and a decomposition of the several fields that constitute the Q-ball will be performed. With the decomposition performed, one can obtain several of the characteristic quantities, and examine how they vary when changing the Q-ball solution parameters.

In the second chapter, self-gravitating bosonic objects, *boson stars*, will be treated. The discussion here follows from the work co-authored by the candidate and recently published in [1]. In this chapter spherically symmetric boson stars are obtained and analyzed. At last some general conclusion are performed.

In this work, basic knowledge of general relativity and quantum physics will be assumed as a prerequisite for the reader. All the expressions and equations will come in geometrized units and we will consider the metric signatures to be $(-,+,+,+)$, in standard spherical coordinates. Concerning the computational infrastructure, the Q-ball solutions are obtained by a commercial FORTRAN solver and the boson star solutions by a code written in C language. With the latter, one can achieve a machine precision of 10^{-16} and with the former 10^{-11}. The data treatment, including plots and decompositions, was carried out in MATHEMATICA. In all the presented plots, the mass and Noether charge values are normalized by the scalar field's mass.

Chapter 2

Q-balls

The familiar Klein-Gordon equation, with a simple mass term, on Minkowski spacetime, admits plane wave solutions. At any given time, a generic wave packet can be constructed as a superposition of these plane waves. The time evolution of such a wave packet, however, is generically dispersive, as the different plane waves have different phase velocities. In other words, even if the initial data forms a compact wave packet, the evolution does not preserve such "lump" of energy.

The dispersiveness of the linear Klein-Gordon equation can be counter-balanced by introducing non-linear terms in the wave equation, *i.e.*, self-interactions of the scalar field. When cancellation of non-linear and dispersive effects occurs, self-reinforcing solitary wave packets emerge: these are dubbed *solitons*. Solitons are, therefore, localized lumps of (in this case scalar field) energy which are dynamically sufficiently stable. They arise as solutions of partial differential wave equations and occur in a variety of physical systems.

Described for the first time in 1834 by John Scott Russel [2], solitons play an important role in several branches of science, namely fiber optics, biology, hydrodynamics and models of high energy physics. In the latter, they have been suggested in the early 1960s as a model of hadrons: the *Skyrme model* [3]. In the 1980s, Coleman observed that a single complex scalar field can yield solitonic solutions, when appropriate (non-renormalizable) self-interactions are included. Such solutions of a non-linear scalar field theory on Minkowski spacetime became known as *Q-balls* [4]. In 1988 Fireman *et al.* [5] and later in 1997 Kusenko *et al.* [6], speculated that dark matter might consist of Q-balls and that the latter play a role in baryogenesis.

Q-balls are non-topological solitons. This means that the existence of these lumps of energy does not rely on a non-trivial topological structure of the vacuum of the theory. They can be either spherically symmetric or spinning, gauged or ungauged. Some branches of Q-balls are stable. Dynamical properties of Q-balls have been study in [7, 8, 9]. Their stability is associated to a conserved global charge (*Noether charge, Q*), which justifies the name Q-balls. Stable Q-balls have the lowest energy per unit charge compared to any other configuration [4], due to this, in 1997 Dvali *et al.* [10] proposed the idea of Q-balls as power plants. In particular, there are excited states, labeled by a quantum number n, with a discrete energy spectrum, for fixed Noether charge. In this thesis, however, we shall focus on fundamental states ($n = 0$).

Q-balls emerge in models with a global $\mathbf{U}(1)$ symmetry. Considering a local or gauged $\mathbf{U}(1)$ symmetry, moreover, endows Q-balls with electric charge. A study of the gauged case without spin, has been performed in [11, 12, 13].

In the absence of interactions with fermions, there are three types of Q-ball stability: the stability with respect to (spontaneous) decay into free particles (quantum mechanical stability); the stability against (spontaneous) decay into Q-balls with a smaller charge (fission); and classical stability (against small perturbations). A detailed study of stability for non-spinning solutions can be found in [12, 14].

In this chapter, we will study the decomposition of Q-ball solutions in a spherical harmonic basis. With this decomposition, we aim at getting some insight on the structure of these solutions and how it depends on the solutions parameters. Our choice of basis arises from the possibility to separate the radial and angular variables in spherical coordinates – see *e.g.* [15]. In this work, the authors

were able to obtain (approximate) numerically spinning Q-ball solutions using the spherical harmonic basis. By contrast, in our work herein, the Q-ball solutions were obtained with a FORTRAN code that solves *exactly* (up to numerical error) the set of field equations. Q-ball solutions are, *a posteriori*, decomposed into the spherical harmonic basis – a kind of spectroscopic analysis to understand their structure. Thus, we call this procedure *Q-ball spectroscopy.*

After presenting the model, we shall explore three different types of solutions:

i) *ungauged (i.e. electrically uncharged), non-spinning (i.e. spherically symmetric)* Q-balls;

ii) *ungauged, spinning* Q-balls;

iii) and *gauged, spinning* Q-balls.

As a first step in the analysis, we obtain an analytical formula to decompose the scalar field into the spherical harmonic basis, and impose some restrictions and/or simplifications arising from the solutions symmetries. To check the correctness of the method, some accuracy and precision tests are performed.

At the beginning of each analysis, the reader will be introduced to the solution's parameters that we choose to study. This study will consist of three different values of the *scalar field frequency* ω, and it will be structured as follows. At first, we study the scalar field. In this part, the change in the scalar field profile, maximum values and *spectral functions* are analysed. For the latter, a detailed study is carried out, by analysing the contribution of each mode to the overall scalar field profile. This will allow to rank the importance of these individual modes and understand how many such modes need to be taken into account in order to reproduce the full solution with any chosen error.

For the gauged solutions, we shall also decompose the *electric potential* as a second part of our study. We perform a *multipolar decomposition*, retrieve the total electric charge from the monopole term and analyse the importance of the subsequent terms for the overall potential. We present some plots illustrating the electric field obtained from the full numerical solution and compare them to the multipolar decomposition.

For the gauged, spinning solutions, the presence of rotation together with an electric charge generates a magnetic field. Thus, as a last part of our study, the magnetic 3*-vector potential* is also considered and decomposed through its *asymptotic decay*, in order to obtain the leading magnetic dipole moment. This also allows us to obtain the *gyromagnetic factor*, as well as other quantities, that we shall attempt to interpret.

2.1 Model

Let us start by describing the model of a complex, self-interacting scalar field. The corresponding Lagrangian density will have solutions describing (un)gauged, (non-)spinning Q-balls, and reads

$$L = -\frac{1}{4}F_{\mu\nu}F^{\mu\nu} + D_\mu\Phi\, D^\mu\Phi^* - U(|\Phi|) \ , \tag{2.1}$$

where $F_{\mu\nu} \equiv \partial_\mu A_\nu - \partial_\nu A_\mu$ corresponds to the Maxwell tensor; $\Phi(t, r, \theta, \phi)$ denotes the complex scalar field, and $D_\mu \equiv \partial_\mu - ig_e A_\mu$ is the covariant derivative with *gauge coupling constant* g_e. The self-interaction potential, $U(|\Phi|)$, will have to obey a set of conditions presented below.

The most generic case describes *gauged, spinning* Q-balls. These possess a spinning phase along the z-axis, where the field must vanish. For this case, the ansatz is taken to be

$$\Phi(t, r, \theta, \phi) = \varphi(r, \theta)e^{i\omega t + im\phi} \ , \tag{2.2}$$

where $\varphi \equiv \varphi(r, \theta)$ is a real function, ω is the scalar field frequency, and we shall always take for our illustration purpose $m = 1$, even though solutions with any $m \in \mathbb{Z}$ exist. This is the rotation "quantum" number. The 4-vector potential, possesses both an electric component – the electric potential $V(r, \theta)$ – and a magnetic component – described by the potential function $\vec{A}(r, \theta)$ –

$$A_\mu dx^\mu = V(r, \theta)dt + A_\phi(r, \theta)\sin\theta d\phi \ . \tag{2.3}$$

Concerning the non-renormalizable self-interaction potential, it is assumed to possess a global minimum at $\Phi = 0$, $U(0) = 0$. On the other hand, a boundary condition is assumed: $U \to \infty$ when $|\Phi| \to \infty$. In addition, the potential must fulfill two extra conditions: it has to possess a stable region at $\Phi = 0$, and this stable region must not be too shallow. These requirements are enforced by the conditions [4]

$$\omega_+^2 \equiv \frac{1}{2}\partial_\Phi^2 U(0) > 0 \; ; \tag{2.4}$$

$$\omega_-^2 \equiv \frac{1}{2}\partial_\Phi^2 U(0) > min\left[\frac{U(|\Phi|)}{\Phi^2}\right]_\Phi \; . \tag{2.5}$$

Observe that the second condition *excludes* a simple mass-term type potential: $U_2 = \mu^2|\Phi|^2$. The only possible renormalizable potential allowed in a scalar field model, $U_{24} = c_1|\Phi|^2 + c_2|\Phi|^4$, can obey these conditions *but only* if $c_2 < 0$, which implies the potential is not bounded from below, and it does not obey the boundary condition above. Thus, non-renormalizable potentials have to be considered. From the previous conditions, there are several possibilities for U which admit Q-ball solutions. With this in mind and to compare with the work done in [15], we will choose the potential to be the following polynomial in $|\Phi|^2$:

- $U_{246} \equiv U(|\Phi|) = c_1|\Phi|^2 + c_2|\Phi|^4 + c_3|\Phi|^6$.

A comparative representation of the three presented self-interaction potentials (U_2, U_{24}, U_{246}) can be observe in Fig. 2.1. We emphasize that U_{246} is the simplest potential that allows Q-ball solutions. But many other possibilities exist (see [16, 17, 18]).

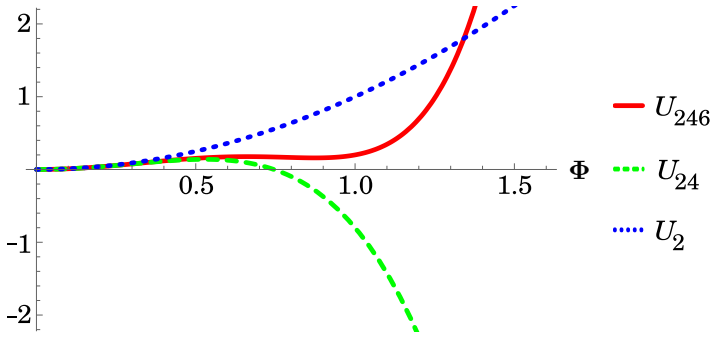

Figure 2.1: Illustrative graphical representation of the potentials, U_{246} (red solid line); U_{24} (green dashed line); and U_2 (blue dotted line). We have taken $c_1,\ c_3 > 0$ and $c_2 < 0$.

In the potential U_{246}, $c_1,\ c_2$ and c_3 are real constants. Conditions (2.4) and (2.5) then require c_1 and c_3 to be positive, and c_2 to be negative. Consequently, U will have a global minimum at $\Phi = 0$, only if $c_1 > (c_2)^2/4$. In our numerical calculations, we have chosen to use

$$c_1 = 1.0 \; , \qquad c_2 = -1.8 \; , \qquad c_3 = 1.0 \; . \tag{2.6}$$

These values are taken for convenience and our results are not qualitatively sensitive to these choices. The choice of $c_1 = 1.0$ implies we are working with a unit mass. Thus, $\omega_+^2 = \mu^2 = c_1 = 1$. Then, the condition $c_1 > (c_2)^2/4$ implies $-2 < c_2 < 0$. We choose $c_2 = -1.8$ to have a sufficiently deep potential well near the local minimum, but keeping the global minimum at $\Phi = 0$. Finally, c_3 is set to unity for convenience. Observe that, from condition (2.5), it follows that for the ungauged, non-spinning case, $\omega_-^2 = \omega_+^2\left(1 - (c_2)^2/4c_3\right) = 0.4359$.

The field equations derived from the Lagrangian (2.1) assume the form

$$\partial^\mu F_{\mu\nu} = ig_e\left[(D_\nu\Phi)^*\Phi - \Phi^*(D_\nu\Phi)\right] \; , \tag{2.7}$$

$$D_\mu D^\mu \Phi = -\frac{\partial U}{\partial|\Phi|^2}\Phi \; . \tag{2.8}$$

The corresponding field energy-momentum tensor reads

$$T_{\mu\nu} = (D_\mu\Phi)^*(D_\nu\Phi) + (D_\nu\Phi)^*(D_\mu\Phi) + F_{\mu\gamma}F_{\nu\lambda}\,g^{\gamma\lambda} + g_{\mu\nu}L \ . \tag{2.9}$$

Using the ansatz (2.2)-(2.3), this implies that the total energy is

$$\begin{aligned} E = \int d^3x\, T_{00} = 4\pi \int_0^\infty dr\, r^2 \int_0^\pi d\theta \sin\theta \Bigg(U(\varphi) + (\partial_r\varphi)^2 + \frac{(\partial_\theta\varphi)^2}{r^2} + \frac{|\vec{E}|^2 + |\vec{B}|^2}{2} \\ + \varphi^2 \left[(\omega + g_e V)^2 + \Big(\frac{m}{r\sin\theta} + g_e A_\phi \Big)^2 \right] \Bigg) \ . \end{aligned} \tag{2.10}$$

A local gauge transformation reads $\Phi \to \Phi e^{ig_e\alpha}$ and $A_\mu \to A_\mu + \partial_\mu\alpha$, where $\alpha \equiv \alpha(x^\mu)$. From the $\mathbf{U}(1)$ invariance of the Lagrangian (2.1), two conserved charges emerge: an *electric charge* Q_e, associated to the *local* $\mathbf{U}(1)$ symmetry, calculated from the electric potential $V(r,\theta)$; and a *Noether charge* Q, that exists even for a *global* $\mathbf{U}(1)$ symmetry. These are related as:

$$Q = \int d^3x\, j_0 = \frac{1}{g_e} \oint \vec{\xi}\cdot d\vec{S} \equiv \frac{4\pi Q_e}{g_e} \ , \tag{2.11}$$

where $j_\mu = i\big[(D_\mu\Phi)^*\Phi - \Phi^*(D_\mu\Phi)\big]$, is the conserved Noether current associated with the (global) $\mathbf{U}(1)$ symmetry. One could face this as follows. The complexity of the field, yields a global (Noether charge), with an associated continuity equation. This charge is a particle conservation number. Gauging this symmetry, endows the scalar particles with electric charge and an associated flux, and therefore a Gauss law. The total angular momentum comes as

$$J = \int d^3x\ T_{0\phi} = \oint \left(\frac{m}{g_e} - A_\phi \right) \vec{\xi}\cdot d\vec{S} \equiv \frac{4\pi Q_e m}{g_e} = mQ \ . \tag{2.12}$$

From these theoretical considerations, fundamental gauged, spinning Q-ball solutions are energy minima, for a given Noether charge Q, which sets both the angular momentum J, as $J = mQ$, and the electric charge Q_e, as $Q_e = g_eQ/4\pi$. Therefore, for the fundamental state, it is possible to obtain a 3-parameter family of solutions, parameterized by (ω, g_e, m), for which the energy E, the Noether charge Q and the electric charge Q_e are finite.

2.1.1 Specialising for ungauged, spinning Q-balls

It is worth specializing the above general theory for the case of *ungauged*, spinning Q-balls, as we will use such relations below. These arise when $g_e = 0$ and $m \neq 0$. When g_e is null, the Maxwell and scalar fields decouple, allowing both equations to be solved individually. Here we shall be only interested in the scalar field equation. The Lagrangian (2.1) reduces to

$$L = \partial_\mu\Phi\,\partial^\mu\Phi^* - U(|\Phi|) \ . \tag{2.13}$$

The $\mathbf{U}(1)$ symmetry is now only a global symmetry: $\Phi \to \Phi e^{i\alpha}$, where α is constant. The Lagrangian (2.13) is invariant under this symmetry, which yields a conserved Noether charge. Using the scalar field ansatz (2.2), the charge can be written as:

$$Q = \frac{1}{i}\int d^3x\ (\partial_0\Phi^*\Phi - \Phi^*\partial_0\Phi) = 2\omega \int d^3x\ \varphi^2 \ . \tag{2.14}$$

The equation of motion emerging from the Lagrangian (2.13) is simply the Klein-Gordon equation on Mikowsky space-time

$$\frac{1}{\sqrt{-g}}\partial_\mu\left[\sqrt{-g}\ g^{\mu\nu}\partial_\nu\right]\Phi = \frac{dU}{d\Phi^*} \ . \tag{2.15}$$

Using standard spherical coordinates, the metric determinant reads $g = -r^4\sin^2\theta$. If we now insert

the ansatz (2.2) into the Klein-Gordon equation (2.15), we obtain the non-linear $3+1$ dimensional PDE (Partial Differential Equation):

$$\left(\frac{\partial^2}{\partial r^2}+\frac{2}{r}\frac{\partial}{\partial r}+\frac{1}{r^2}\frac{\partial^2}{\partial\theta^2}+\frac{\cos\theta}{r^2\sin\theta}\frac{\partial}{\partial\theta}-\frac{m^2}{r^2\sin^2\theta}+\omega^2\right)\varphi=\frac{dU(\varphi)}{d\varphi}\ . \tag{2.16}$$

For concreteness also observe that the energy (2.10) reduces to

$$E=2\pi\int_0^\infty dr\,r^2\int_0^\pi d\theta\sin\theta\left[\omega^2\varphi^2+(\partial_r\varphi)^2+\frac{1}{r^2}(\partial_\theta\varphi)^2+\frac{m^2\varphi^2}{r^2\sin^2\theta}+U(\varphi)\right]\ . \tag{2.17}$$

2.1.2 Specialising for ungauged, non-spinning Q-balls

Finally, let us also explicitly consider the simplest ungauged, spherically symmetric Q-balls. That is, we take $g_e=0=m$. Although we shall not consider explicit numerical ungauged, spherical Q-balls in this work, they stand as the natural reference to introduce some concepts and to perform some comparisons.

With $g_e=0=m$, the ansatz (2.2) reduces to $\Phi=\varphi(r)e^{i\omega t}$, where the real amplitude satisfies the equation

$$\frac{d^2\varphi}{dr^2}+\frac{2}{r}\frac{d\varphi}{dr}+\omega^2\varphi=\frac{\partial U}{\partial\varphi}\ . \tag{2.18}$$

This equation, of course, is a special case of (2.16), when spherical symmetry holds and $\varphi(r,\theta)\equiv\varphi(r)$. Integrating in φ, this equation is equivalent to

$$\left(\frac{d\varphi}{dr}\right)^2+\omega^2\varphi^2-2U(\varphi)=\xi-4\int_0^r\frac{dr'}{r'}\left(\frac{d\varphi}{dr'}\right)^2\ , \tag{2.19}$$

which describes qualitatively a particle moving with friction in an 1D effective potential $U_{\mathit{eff}}(\varphi)=\omega^2\varphi^2-2U(\varphi)$, where the integration constant ξ plays the role of the total energy,

$$\xi=4\pi\int_0^\infty dr\,r^2\left[\omega^2\varphi^2+(\partial_r\varphi)^2+U(\varphi)\right]\ . \tag{2.20}$$

2.2 Physical and asymptotic behavior

In Sec. 2.1 the mathematical model for gauged, spinning Q-balls was presented. The generic model contains three parameters, (ω,g_e,m). Special cases include the ungauged, spinning Q-balls ($g_e=0$), the gauged unpinning Q-balls ($m=0$, which we will not consider explicitly) and the ungauged, non-spinning Q-balls ($g_e=0=m$). In this section, we aim at constructing and presenting a qualitative overview of each Q-ball type. The properties and behaviors presented are intended to build some physical insight on these solutions. In contrast to the analytical study, we shall start from the simplest case (the ungauged, non-spinning Q-ball) and progressively increase the generality of the solutions.

2.2.1 Ungauged, non-spinning Q-balls

For ungauged, non-spinning Q-balls, the effective potential is $U_{\mathit{eff}}\ (\varphi)=\omega^2\varphi^2-2U(\varphi)$, which is represented in Fig. 2.2. Recall the particle dynamics perspective introduced in Sec. 2.1.2. At "moment" $r=0$, we assume the particle is at rest at the position with "coordinate" φ_0, which is close to the U_{eff} global maximum. Then, it starts to move along φ, decreasing its potential energy, and dissipating some of its total energy. By fine tuning, it is possible to adjust φ_0 such that for $r\to\infty$, $\varphi\to 0$. The particle dissipates all its energy as it reach the local maximum of U_{eff}, at the origin of φ, where it rests [15]. If φ_0 is the minimum possible value of φ for which this is possible, the corresponding scalar field configuration is a *fundamental state*.

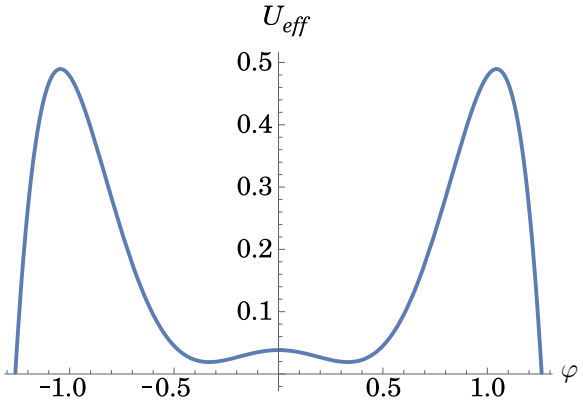

Figure 2.2: Graphical representation of the effective potential $U_{\mathit{eff}}(\varphi) = \omega^2\varphi^2 - 2U(\varphi)$.

If at "moment" $r = 0$, the particle starts, at rest, from a position $\varphi_1 > \varphi_0$, it will, generically, overshoot $\varphi = 0$. The particle will come to rest at some $\varphi \neq 0$, which implies a scalar field configuration that does not decay to zero at spatial infinity. But, for *a particular fine-tuned value* $\varphi_1 > \varphi_0$, the particle bounces back at some negative φ. That is, it climbs the potential barrier on the negative φ side, (dissipating some energy) and then drops. As it comes down the potential, the particle has already lost enough energy in order to reach the local maximum at $\varphi = 0$ with zero energy. In this way, one can obtain *excited Q-ball states*. This process gives solutions with one node, $n = 1$, and can be repeated for other excited state $n \in \mathbb{N}$ in an analogous fashion.

One can also use this particle dynamics analogy to understand, qualitatively, the change in the Q-ball solutions when varying ω. When $\omega \to \omega_+$, the minimum of the effective potential becomes shallower and moves closer to $\varphi = 0$. This implies that the value of φ_0 required to obtain the fundamental (and excited) Q-ball solutions becomes smaller, as the field has a smaller path to dissipate the initial energy, as to end up at $\varphi = 0$ at rest. Q-balls therefore decrease in amplitude, which tends to zero. By contrast, when $\omega \to \omega_-$, the effective potential maximum becomes smaller and at higher values of $|\varphi|$. Thus, φ_0 becomes larger and the particle spends more "time" at larger values of the field. Q-balls become more spatially extended, with broader peaks and higher field amplitudes; in the limit, the energy and Noether charge of the solutions tend to infinity.

2.2.2 Ungauged, spinning Q-balls

As already mentioned, solutions of ungauged, (un)spinning Q-balls – for which energy and Noether charge are finite – exist for a range of values of ω. We shall now use the spinning case to illustrate some further physical properties of the solutions.

Let us start by remarking on the solutions' stability. Fig. 2.3 exhibits the total energy, E, and Noether charge, Q, *vs.* the field frequency, ω, for spinning Q-balls with $m = 1$. The comparison between E and Q gives a simple necessary condition for stability, namely $E < Q$. The reasoning is that the energy of a bound Q-ball must be smaller than the energy of a collection of individual scalar particles. Since the mass of the individual particles has been set to unity and Q is a measure of the number of particles, this amounts to the condition above. From Fig. 2.3, it is then possible to conclude that this stability condition only holds for a certain frequency interval $\omega_- < \omega < \omega_{\rm eq}$, where $\omega_{\rm eq} = 0.8289$ is the solution for which $E = Q$ $\big($for the chosen potential parameters, *cf.* (2.6)$\big)$.

Fig. 2.3 shows that both E and Q present the same behavior: a divergence when $\omega \to 1$ and as ω decreases. The lower bound, was impossible to reach due its slow divergence as $\omega \to \omega_-$ (compared with the explosive one as $\omega \to \omega_+$).

As in the spherically symmetric case, it holds that $\omega_+^2 = \mu^2$, while ω_- is m-dependent. When ω tends to these extremal values, a divergence in the values of E and Q occurs. In between, there is a critical value, $\omega_{\rm crit}$ ($\omega_{\rm crit} = 0.92$ for $m = 1$), where a minimum of E and, simultaneously, Q is reached. This behavior is found for all m values, and it is qualitatively the same as in the non-spinning case.

The existence of a minimum value for the Noether charge, creates a restriction on the total angular momentum (J), by virtue of relation (2.12). Q-balls are not allowed to rotate arbitrarily slowly; there is a discrete spectrum of spinning excitations.

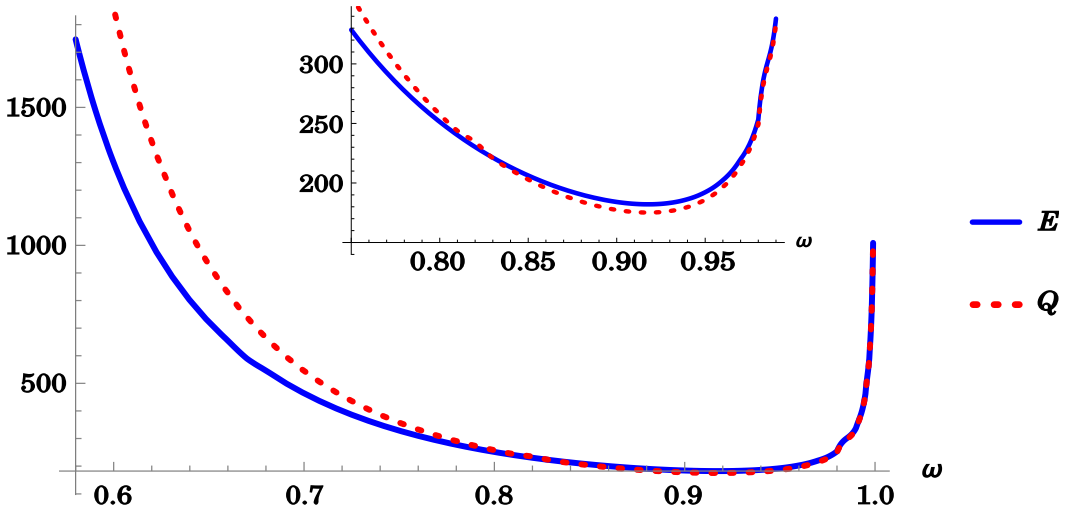

Figure 2.3: Fundamental ungauged, spinning ($m = 1$) Q-balls dependence with ω of energy, E, (blue solid line) and Noether charge, Q (red dashed line).

Let us briefly comment on their spatial distribution. As in the spherically symmetric case, spinning Q-balls become larger as ω tends to the limits of the allowed interval. For $\omega \to \omega_-$, they can be viewed as squashed spheroids, homogeneously filled inside. φ increases as we move away from the central axis, reaching a maximum at the surface of the spheroid, after which it rapidly goes to zero. Solutions with $\omega \to \omega_+$, also tend to large spheroids. This time, however, they are hollow and possess the maximum of the energy density at the surface – being close to zero everywhere else.

To analyze the behavior of the limiting Q-ball solutions, in the allowed frequency interval, we can decompose their energy in a sum of different contributions

$$E = 2\pi \int_0^\infty dr\, r^2 \int_0^\pi d\theta \sin\theta \left(E_\omega + E_r + E_\theta + E_S + E_U\right) \ , \tag{2.21}$$

where

$$E_\omega \equiv \omega^2\varphi^2 \ , \quad E_r \equiv (\partial_r\varphi)^2 \ , \quad E_\theta \equiv \frac{(\partial_\theta\varphi)^2}{r^2} \ , \quad E_S \equiv \frac{m^2\varphi^2}{r^2\sin^2\theta} \ \text{ and } \ E_U \equiv U(\varphi) \ . \tag{2.22}$$

In Fig. 2.4, we exhibit the integrated relative contribution of these five energy integral components. The figure shows that, as $\omega \to \omega_\pm$, the major contributors for the energy are the ones also present in the spherical symmetric case (E_ω, E_r and E_U). Even more, we can observe a small component that comes from E_S; the spinning energy (for $m = 1$) yields a small contribution for the total energy. However, since E_S is proportional to m^2, it will increase its relative weight as m increases.

At last, observe that, as $\omega \to 1$, E_ω and E_U tend to 50%. If this also holds for $\omega \to \omega_-$, extrapolating the E_ω and E_U curves in Fig. 2.4, one obtains $\omega_- \approx 0.42$. This can be compared with the *analytic* value for the non-spinning case, which is $\omega_- \simeq 0.4359$, *cf.* below (2.6). If this extrapolation is correct, we conclude that the Q-balls frequency window is only mildly sensitive to changing $m = 0$ to $m = 1$.

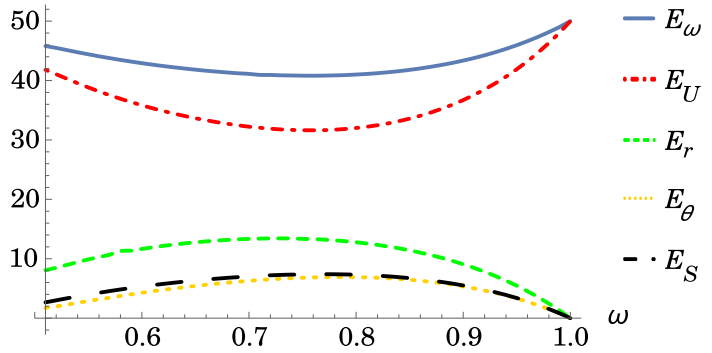

Figure 2.4: Energy integral components, in %, as a function of ω, for the ungauged spinning case.

2.2.3 Gauged, spinning Q-balls

As in the ungauged case, the solution dependence in ω will have a lower and higher bound. This time, however, there is an extra parameter, creating a three parameters solution (ω, g_e, m). For a given m, each value of g_e will possess a minimum [maximum] value of $\omega_-(g_e)$ $[\omega_+(g_e)]$, as well as the corresponding well-shaped energy and Noether charge curves.

For a given ω and m, increasing g_e from the ungauged case implies an increase of the solutions E and Q, until they diverge at some g_e^{max}. At this g_e^{max}, the electric repulsion dominates, the energy diverge, and the solitonic solutions are no longer possible.

Concerning the Q-balls spatial distribution, they exhibit a similar toroidal shape as in the previous case. As we increase g_e, due to the electric repulsion, Q-balls start to increase its radial distribution and decrease its local density. When g_e^{max} is reached, Q-balls are destroyed, indicating a limit for the charge density that a Q-ball can support.

The fact that there is a maximum value for the allowed charge of a gauged Q-ball, points to a fundamental difference relatively to the ungauged case. In the latter, it is possible to have a certain amount of Q-charge (*i.e.* a certain number of particles) occupying an arbitrarily small region of space. However, due to the electrical repulsion, that is impossible for gauged solutions. All these properties are going to be explicitly demonstrated in Sec. 2.4.

2.3 Multipolar decomposition

Gauged, spinning Q-balls are composed of three fields: the scalar field (φ), that will be subjected to a *spectral decomposition*; an electric field ($\vec{E}$) originated by the electric potential (V), on which we will perform a *multipolar decomposition*; and a magnetic field ($\vec{B}$) for which we will study the *asymptotic decay* of its vector potential ($\vec{A}$). Note that, in the ungauged spinning Q-ball, the two electromagnetic fields are absent and the scalar field is the only field that requires a decomposition.

As a further remark, observe that a spectral decomposition is also a multipolar decomposition; still, the different nomenclature helps us to distinguish the associated fields.

As already mentioned in Sec. 2, the decomposition of Q-ball solutions in *associated Legendre functions* $\left(\mathcal{P}_l^m(x)\right)$, grants the possibility to separate the radial and angular variables in spherical coordinates. Furthermore, since associated Legendre functions form a complete set, it is natural to expect that, by increasing the number of terms (l) in our expansion, one can obtain a series as close as desired to the exact solution. In this section, we shall present and test the decomposition procedures for each Q-ball field and how they depend on the number of terms l in each series.

2.3.1 Scalar field $\varphi(r,\theta)$

It is interesting to notice that (2.8) is symmetric under reflections in the xy-plane, *i.e.*, if $\varphi(r,\theta)$ is a solution, so it is $\varphi(r,\pi-\theta)$. In addition, due to the sole presence of odd powers of φ in the latter, $-\varphi(r,\theta)$ is also a solution. So, if $\varphi(r,\pi-\theta)$ is a solution, one has the freedom to choose the parity to be either $\varphi(r,\pi-\theta)=\varphi(r,\theta)$ [even] or $\varphi(r,\pi-\theta)=-\varphi(r,\theta)$ [odd].

In the case of $\mathcal{P}_l^m(x)$, they possess an even (odd) parity with respect to $\theta\to\pi-\theta$ for even (odd) values of $l+m$. In other words, the parity P of each associated Legendre function is $P=(-1)^{l+m}$. As a result, when the *spectral expansion* is performed, it will be divided into modes that change sign under the reflection, and modes that maintain it.

If m is fixed, there are two solutions with distinct parity P: one with $l=m+2k$ ($P=1$), and another with $l=m+2k+1$ ($P=-1$), where $k\in\mathbb{N}_0$. For the problem under analysis, we take $\varphi(r,\theta)=\varphi(r,\pi-\theta)$ and $m=1$, resulting in the cancellation of all odd terms in the expansion. In other word, we focus on even parity solutions.

To find the *spectral functions* $\boldsymbol{f}_l(r)$ at a given value r of each *spectral mode*, we have to take into account that the associated Legendre functions, $\mathcal{P}_l^m(x)$, form a complete set. The latter's possess the orthogonality condition

$$\int_{-1}^{+1} dx\,\mathcal{P}_l^m(x)\mathcal{P}_{l'}^m(x)=\frac{\delta_{ll'}}{c_{lm}}\ ,\qquad c_{lm}\equiv\frac{(2l+1)(l-m)!}{2(l+m)!}\ . \tag{2.23}$$

For a given $m\in\mathbb{N}_0$, such that $m\geqslant 0$ and $l\geqslant m$, the generic spectral expansion is

$$\varphi(r,\theta)=\sum_{l=m}^{\infty}\mathbf{f}_l(r)\,\sqrt{c_{lm}}\,\mathcal{P}_l^m(\cos\theta)\ , \tag{2.24}$$

where, for an arbitrary point r, $\mathbf{f}_l(r)$ is a constant that corresponds to the amplitude of the l^{th} associated Legendre function. To find such a constant, one has to perform the projection of φ into the associated Legendre function basis: $\mathbf{f}_l=(\mathcal{P}_l^m,\varphi)$. Here, the parentheses denote a scalar product. Explicitly, this scalar product is given by:

$$\begin{aligned}(\mathcal{P}_l^m,\varphi)\qquad &=2\int_0^{\frac{\pi}{2}}d\theta\sin\theta\ \varphi(r,\theta)\,\sqrt{c_{lm}}\,\mathcal{P}_l^m(\cos\theta)\\ &=2\sum_{l'=m}^{\infty}\mathbf{f}_{l'}(r)\int_0^{\frac{\pi}{2}}d\theta\sin\theta\,\sqrt{c_{l'm}}\,\mathcal{P}_{l'}^m(\cos\theta)\,\sqrt{c_{lm}}\,\mathcal{P}_l^m(\cos\theta)=\mathbf{f}_l(r)\ .\end{aligned} \tag{2.25}$$

The integration is performed until $\frac{\pi}{2}$, since we are focusing on even parity solutions. In the last step we have used (2.23). This gives us the formula for the generic spectral function $\mathbf{f}_l(r)$ such that (2.24) corresponds to the decomposition in associated Legendre functions of the numerical solution φ.

Accuracy test for an explicit example

In order to illustrate that the spectral decomposition is, indeed, able to correctly describe our numerical solution, we shall now provide an explicit example that it is able to recover the form and characteristic quantities of the numerically obtained $\varphi(r,\theta)$, for a sufficiently large number of terms. For our example, we take, as usual, $m=1$; thus, the only possible values for l are odd.

To numerically solve the field equations, we rely on a commercial FORTRAN solver, the CADSOL program package [19, 20]. The latter is designed to numerically solve non-linear systems of elliptic and parabolic PDEs, through a finite difference method with mesh refinement and automatic control of the consistency order. With this package one can numerically solve, with a typical precision of 10^{-11}, the field equations (2.7) and (2.8) for an even parity φ, in the $r\in[0,100]$ – with 300 points – and $\theta\in[0,\frac{\pi}{2}]$ – with 50 points – domain. The Klein-Gordon and Maxwell equations were solved numerically by imposing the boundary conditions

$$r=0:\ \partial_r V=A_\phi=\varphi=0\ ,\qquad r=\infty:\ V=A_\phi=\varphi=0\ , \tag{2.26}$$

$$\theta=0:\ \partial_\theta V=A_\phi=\varphi=0\ ,\qquad \theta=\frac{\pi}{2}:\ \partial_\theta V=\partial_\theta A_\phi=\partial_\theta\varphi=0\ . \tag{2.27}$$

Resorting to the CADSOL solver, say, the solution with $\omega = 0.70$ and $g_e = 0.010$. For these parameters, the maximum of the scalar field $\varphi_{max} = 0.9741$, occurs at $(r, \theta) = (3.7448, \frac{\pi}{2})$.

As a first error diagnosis, let us look at the energy and Noether charge convergence with the increase in the number of *spectral modes* l in the expansion. The energy and Noether charge calculated from the numerical data is $E = 467.9874$ and $Q = 549.6962$. The corresponding values of E and Q computed from considering a finite number of modes are given in Table 2.1.

Table 2.1: Energy, E, and Noether charge, Q, convergence with the increase in the number of spectral modes l, for a gauged spinning Q-ball solution, with $\omega = 0.70$, $g_e = 0.010$, $m = 1$.

	$l = 1$	$l = 1, 3$	$l = 1, 3, 5$	$l = 1, ..., 7$	$l = 1, ..., 9$	$l = 1, ..., 11$
E	461.5969	467.9043	467.9814	467.9858	467.9873	467.9874
Q	535.6637	548.9436	549.6305	549.6905	549.6937	549.6962

As the table shows, both E and Q tend to the respective numerical values as we increase the number of spectral modes. Taking only the first four modes ($l = 1, 3, 5, 7$) one already obtains a relative error smaller than 10^{-3}. Full agreement with the numerical result is obtained with six modes (relative error smaller than 10^{-6}).

For our second error diagnosis, we shall examine the spatial relative difference between the numerical values of φ, and the values obtained through the spectral expansion. For concreteness, we analyze this relative difference on the equatorial plane $\theta = \frac{\pi}{2}$, where the maximum of the scalar field profile exists – Fig. 2.5.

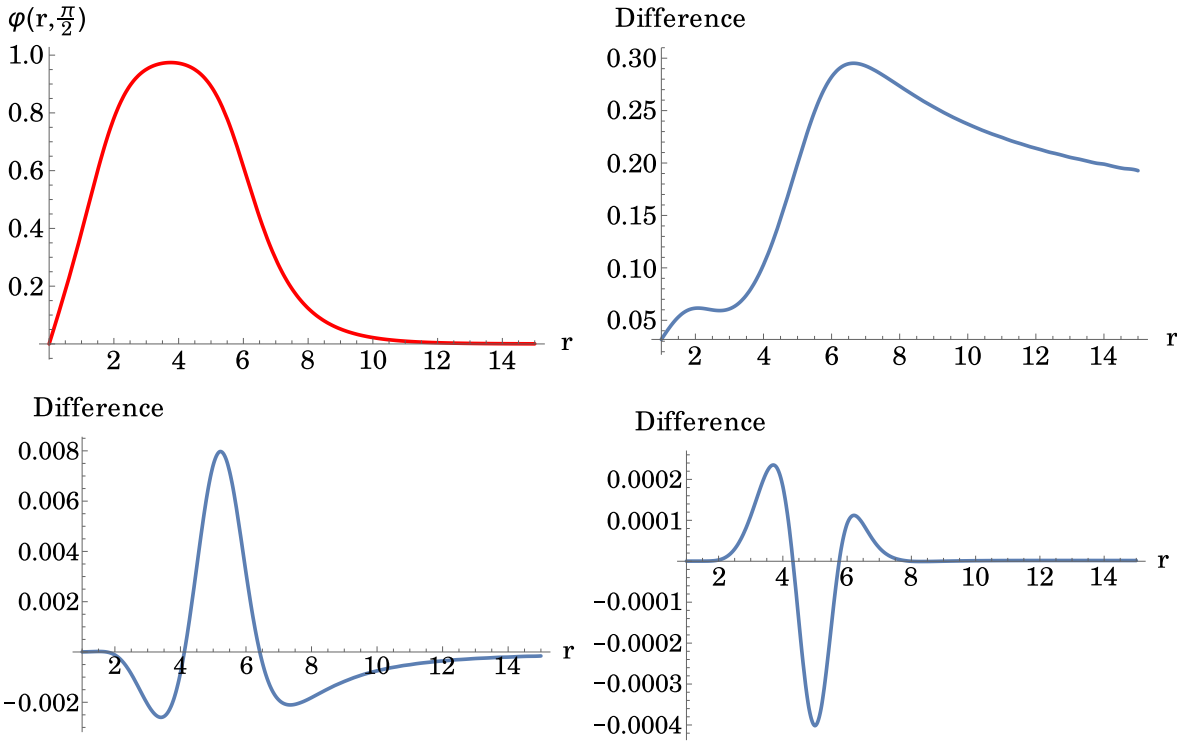

Figure 2.5: (Top left) radial profile of the numerically obtained $\varphi(r, \frac{\pi}{2})$. Relative difference between the numerical φ and the spectral expansion, as a function of $(r, \frac{\pi}{2})$ for (top right) $l = 1$; (bottom left) $l = 1, ..., 7$; (bottom right) $l = 1, ..., 11$ modes.

From Fig. 2.5 we observe that, for small and large values of r, the first four spectral functions are able to describe φ with a maximum of $\sim 10^{-2}$. If we now observe the radial profile of φ (top

left) and the evolution of the relative difference, it is possible to notice that the most difficult part to decompose is the maximum and the decaying tail, *i.e.*, it requires an increased amount of spectral functions to describe it. Even so, it is important to mention that with only four modes, the spectral decomposition is able to correctly describe the numeric φ with a relative error around 10^{-3}. Such a behavior, demonstrates the simplicity and power of decomposing this type of function into associated Legendre functions.

2.3.2 Electric potential $V(r,\theta)$

For the electric field, due to the scalar nature of its electric potential $V(r,\theta)$, it is possible to perform a (scalar) *multipolar expansion*. For our solutions, $V(r,\theta)$ presents axial symmetry, and its multipolar expansion can be performed in terms of associated Legendre functions with $m=0$ $\left[\mathcal{P}_l^{m=0}(x)\equiv\mathcal{P}_l(x)\right]$. Note that, as in the scalar field case, $V(r,\theta)$ is symmetric under reflections along the xy-plane, $\theta\to\pi-\theta$. This implies that $V(r,\theta)=V(r,\pi-\theta)$. Again, due to the well defined parity of $\mathcal{P}_l$, the odd terms (in l, with $m=0$) do not appear, and we only have to take into account the terms with an even parity.

For the electric potential, the multipolar expansion can be performed inside or outside the charge distribution. For a gauged, (non-)spinning Q-ball the charge distribution is non-zero everywhere, and hence, one uses the multipolar expansion inside the charge distribution

$$V(r,\theta)=\sum_{l=0}^{\infty} I_l r^l\,\sqrt{c_l}\,\mathcal{P}_l(\cos\theta)\equiv\sum_{l=0}^{\infty}\mathbf{V}_l(r)\,\sqrt{c_l}\,\mathcal{P}_l(\cos\theta)\ , \tag{2.28}$$

where I_l corresponds to the *internal multipole moment*, and $\mathbf{V}_l(r)\equiv I_l r^l$ is the *multipolar function*. The *standard (or external) multipole moment* (q_l) at some large radius is R, $I_l=q_l/R^{l+1}$; the large radius guarantees there is only a negligible amount of charge outside this radius (due to the rapid fall off of the field). The external multipole moment with $l=0$ is also denominated *monopole moment* and corresponds to the usual electric charge $q_0\equiv Q_e$.

Since $\mathcal{P}_l$ forms a complete set, it is possible to perform a projection of $V(r,\theta)$ into such a basis and obtain the multipolar functions at some radius r. The latter is given, as in the scalar field case (2.25), by $I_l r^l=(\mathcal{P}_l,V)$

$$(\mathcal{P}_l,V)=\int_0^{\frac{\pi}{2}}\ d\theta\sin\theta\,V(r,\theta)\,\sqrt{c_l}\,\mathcal{P}_l(\cos\theta)=I_l r^l=\mathbf{V}_l(r)\ . \tag{2.29}$$

On a side note, observe that the multipolar decomposition of an electric potential uses associated Legendre functions with $m=0$, while the spectral decomposition performed on the scalar field uses the same functions but with $m=1$. The relation between associated Legendre functions

$$\mathcal{P}_l^m(x)=(-1)^m(1-x^2)^{\frac{m}{2}}\frac{d^m}{dx^m}\big(\mathcal{P}_l(x)\big)\ , \tag{2.30}$$

would suggest the association on an electric field to the spectral modes of the scalar field. This naive association, however, does not occur. The fact that the electric field is a vector and that only one of its components (in θ) will have the same form as the scalar field, is already a good indication that no relation between the two quantities holds.

On the other hand, look at the Noether charge (2.11) – a measure of the number of particles in a soliton. One observes a dependence *only* on the electric monopole. This is no surprise; gauged solitons are an agglomerate of charged particles, each with a charge $q_{part}=\frac{4\pi Q_e}{Qg_e}$. While the electric monopole corresponds to the total charge present on a soliton, the higher multipoles are related to the charge distribution. The fact that the Noether charge is only connected to the monopole, is *per se*, a prove that the connection between the two series of associated Legendre functions are a mathematical relation and not a physical one.

Accuracy test for an explicit example

As in the spectral decomposition, to illustrate the ability of the multipolar decomposition to correctly decompose the numerically obtained electric potential, we shall now present an explicit example that the former is able to recover the form and characteristic quantities of the latter, when a sufficiently high order is considered.

Due to the axial symmetry, the only non-vanishing $\mathcal{P}_l^m$ terms are the ones with $m = 0$ and l even. For the same example as considered in Sec. 2.3.1 ($\omega = 0.70$ and $g_e = 0.010$), the maximum of the electric potential is $V_{max} = 0.1090$ at $(r, \theta) = (2.4397, \frac{\pi}{2})$. The electric charge obtained at infinity is $Q_e^{inf} = -0.4367$, with an electrostatic energy of $E_e = 0.3772$.

In Table 2.2, it is possible to observe that, as the number of multipoles increases, the electrostatic energy ($E_e = \int d^3x \frac{|\vec{E}|^2}{2}$) tends to stabilise and to the numerical value. The first multipole (monopole) is the main contributor, containing more than 99% of E_e. Taking only the first four multipoles ($l = 0, 2, 4, 6$), one already obtains a relative error smaller than 10^{-4}. With the first six modes, it is possible to obtain a relative error smaller than 10^{-7}.

Table 2.2: Electrostatic energy, E_e, convergence with the increase in the number of multipoles l in the multipolar decomposition for $\omega = 0.70$ and $g_e = 0.010$.

	$l = 0$	$l = 0, 2$	$l = 0, 2, 4$	$l = 0, ..., 6$	$l = 0, ..., 8$	$l = 0, ..., 10$
E_e	0.3768	0.3770	0.3771	0.3771	0.3772	0.3772

In Fig. 2.6 we consider the radial profile, and the relative difference between the numerical electric potential and the multipolar decomposition.

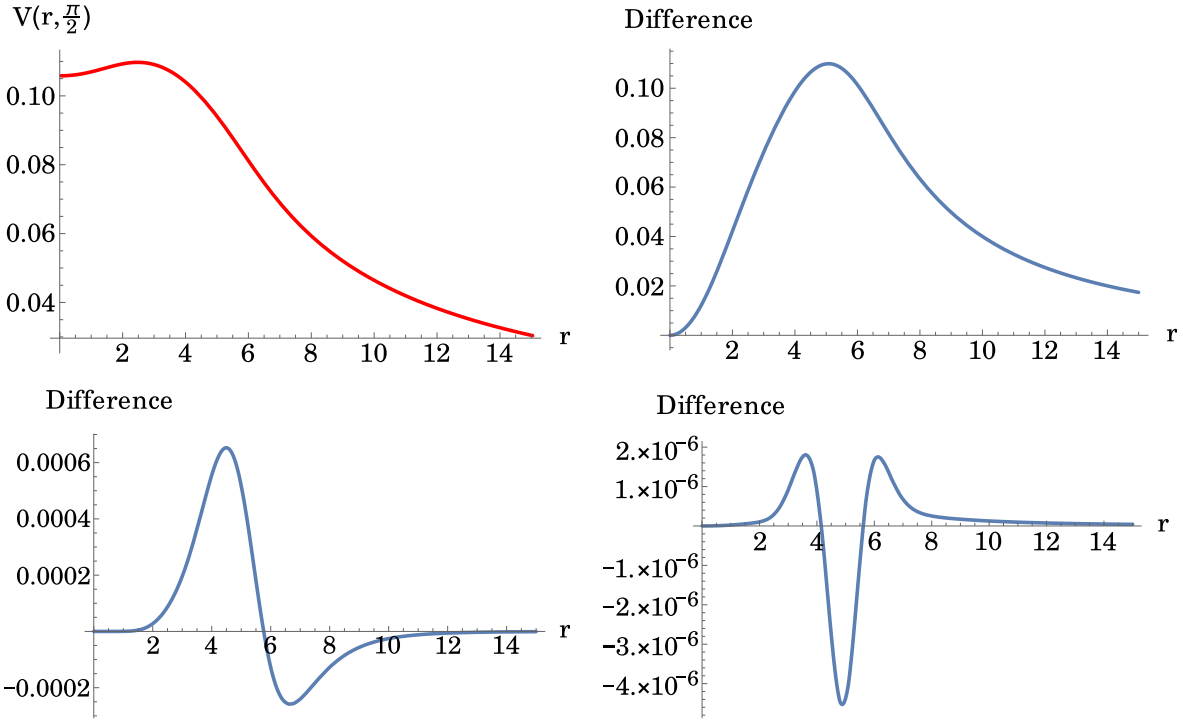

Figure 2.6: (Top right) radial profile of the numerical obtained $V(r, \frac{\pi}{2})$. Relative difference between the numerical V and the multipolar decomposition as a function of $(r, \frac{\pi}{2})$ for (top left) $l = 0$; (bottom left) $l = 0, ..., 6$; (bottom right) $l = 0, ..., 10$.

It is possible to observe that, an increase in the number of multipoles, corresponds to a decrease in

the relative difference. The multipolar expansion is therefore able to decompose the electric potential into the associated Legendre functions basis, with an error that can be as small as desired.

More quantitatively, observe that with the same amount of terms, the multipolar decomposition yields better results than the spectral decomposition. While in the spectral decomposition (Fig. 2.5) a four term series gives a mean error $\sim 10^{-3}$, the multipolar decomposition gives $\sim 10^{-4}$. Such difference is mainly caused by the associated Legendre functions that are used. At least for this example, it is less demanding, in terms of the expansion, to describe the $m = 0$ electric potential than the $m = 1$ scalar field profile. Concerning the spatial profile, the multipolar decomposition is already able to describe the numerical V for the small and large values of r, using only the first multipole (monopole term); it misses, however, the global maximum as well as the start of the decaying tail, where it reaches the greatest relative difference of 0.10. With the increase of the number of multipoles, this global maximum and radial decaying tail are captured and the relative difference decreases to 10^{-6}.

2.3.3 Potential function $\vec{A}(r, \theta)$

At last, the remaining field that requires a decomposition is the magnetic field $\vec{B}$. In contrast to the electric potential, the corresponding potential function, $\vec{A}$, is a vector field ($\vec{B} = \nabla \times \vec{A}$), which in turn requires a multipolar expansion with resort to *vector* spherical harmonics. Alternatively, note that each multipole decays with a different power of the radial component r (2.31). So, by resorting to a radial decay study, one can obtain for each mode the respective total multipole moment.

For our solutions, the magnetic field source consists on a distribution of rotating charges. As usually, in standard electromagnetism, there is no magnetic monopole term. The leading term will be a magnetic dipole (μ_B). To second non-trivial order, the corresponding potential function – the azimuthal component of the vector potential, A_ϕ – can be asymptotically decomposed into the dipole plus the quadrupole (q_B) term

$$A_\phi = \frac{\mu_B \sin\theta}{r} + \frac{q_B \sin\theta\cos\theta}{r^2} + \mathcal{O}\left(\frac{1}{r^3}\right) \ . \tag{2.31}$$

To obtain the values of μ_B and q_B, one can perform a numerical fit in r for every value of θ – a process easily done with some MATHEMATICA routines. With this numerical procedure, one gets for every discrete value of θ, the total amplitude of the radial component, *i.e.*, when we perform the numerical fit, let us say, for the dipole moment at given θ_0, the obtained radial amplitude corresponds to $\mu_B \sin\theta_0$. To obtain the multipole moments we are then required to divide the radial amplitude by the respective angular component. In principle, for every angular direction θ one should get the same value of μ_B and q_B. However, due to the limited numerical precision of our data, such a behavior does not exist, as we shall see in the concrete example below.

Accuracy tests for an explicit example

As already mentioned, for the potential function case an asymptotic decay fit will be performed. With this method, we are be able to avoid the more complex vectorial decomposition of a magnetic field into spherical harmonics. For the current example ($\omega = 0.70$ and $g_e = 0.010$) the total magnetic moment at infinity is $\mu_B^{inf} = -0.3115$.

Due to the limitations of this method, we are not able to perform a comparative analyses of the radial dependence between our expansion and the numerical data. So, to argue if our expansion was correctly performed, another type of tests are required.

First, let us compare the magnetic moments: the total magnetic dipole moment obtained at infinity from the numerical data is $\mu_B^{inf} = -0.3115$. With the asymptotic expansion, it is possible to obtain a value for the dipole moment of $\mu_B = -0.3114$, a close enough value (relative difference of 10^{-4}) taking into account the drawbacks of this method.

Even further, we obtained a value for the quadrupole moment of $q_B = -0.0691$, indicating – as expected from the axial symmetry – that the majority of our magnetic contribution comes from the

dipole term. In relation to the q_B, one does not possess a numerical value to compare with, however, it seems fruitful to obtain the quadrupole moment. Let us look at Fig. 2.7 where it is represented the values for the dipole moment as we change θ. In the latter, one can see a quick convergence to μ_B as $\theta \to \frac{\pi}{2}$.

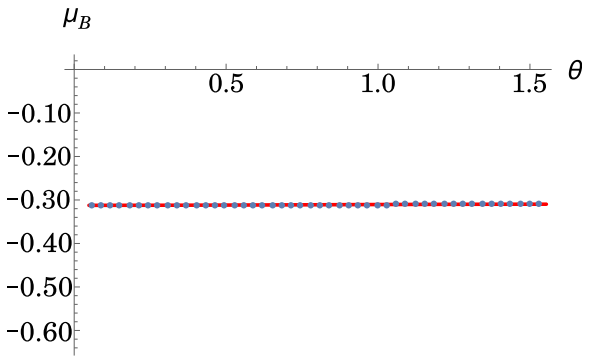

Figure 2.7: Dipole moment, μ_B, extracted from the numerical data for $(\omega = 0.70, g_e = 0.010)$. Solid red line: numerical fitting; dashed blue line: discrete numerical data.

The second condition to take into account is the monopole term. Due to the problem nature, there is no justification for the presence of a monopole term. However, since this is a numerical calculation, there is always some associated error, being the absence of a magnetic monopole a good test of our numerics. For this example the magnetic monopole term is $\sim 9.32 \times 10^{-9}$, a small enough value to be considered a numerical error and to conclude that this method gives good results at large radius.

2.4 Q-ball decomposition

In Sec. 2.3 it was shown how to obtain the spectral functions $\mathbf{f}_l$, the multipolar functions $\mathbf{V}_l$, and the magnetic moments μ_B and q_B. The convergence of each decomposition was also tested. It was observed that, for the spectral and multipolar decomposition, the first four terms are enough to obtain a good approximation. In relation to the magnetic field, we observed sensible results with asymptotic fitting, hence, we will use them.

In this section, the previous functions are used to decompose a selection of gauged, spinning Q-ball solutions. Each solution (ω, g_e) will have its own decomposition. We focus on three values of ω, each with three values of g_e. The selection of solutions corresponds to: (i) a solution in the lower stable region, with $\omega_1 = 0.60$; (ii) a solution at the minimum of the energy/charge, with $\omega_2 = 0.92$; (iii) and a solution near ω_+, with $\omega_3 = 0.999$. The choice of g_e will be ω dependent.

For simplification purposes, the radial dependence of the spectral and multipolar functions will be dropped $\big(\mathbf{f}_l(r) \equiv \mathbf{f}_l$ and $\mathbf{V}_l(r) \equiv \mathbf{V}_l\big)$, as well as the radial and angular dependency of the scalar field and electric potential $\big(\varphi(r,\theta) \equiv \varphi$ and $V(r,\theta) \equiv V\big)$.

2.4.1 Solutions with $\omega_1 = 0.60$

With $\omega_1 = 0.60$, an ungauged spinning Q-ball solution lies near the left divergence (see Fig. 2.3). The uncharged solution ($g_e = 0.0$) has $E = 1299.4703$ and $Q = 1859.0341$. When the gauge coupling constant g_e is introduced, gauged spinning Q-ball solutions are obtained. For the current scalar frequency ω_1, the maximum of g_e occurs around $g_e^{max} = 0.04$, and so, we will take the three values to be $g_e = \{0.0, 0.010, 0.035\}$.

Observe Fig. 2.8, it shows, for the three values of g_e, the 3D graphical representation of φ at $r = 10$ (left) and a radial cut at $\theta = \frac{\pi}{2}$ (right) of φ – the maximum of the scalar field profile exists at $\theta = \frac{\pi}{2}$.

In a first qualitative analysis, one can note that all solutions possess a broad peak that prolongates to $r \sim 10$.

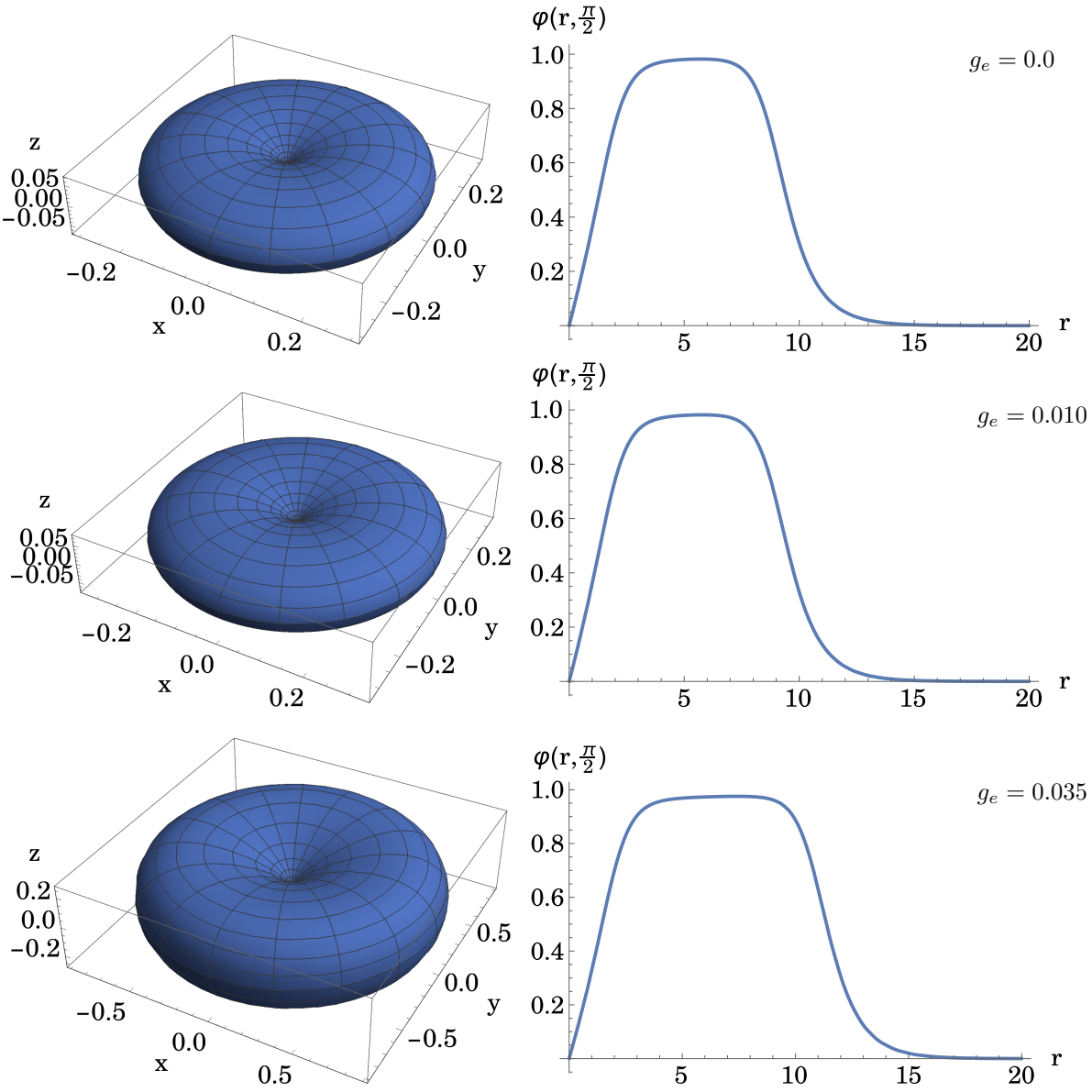

Figure 2.8: Graphical representation of φ for $\omega_1 = 0.60$ and (top) $g_e = 0.0$; (middle) $g_e = 0.010$, (bottom) $g_e = 0.035$. (Left panels) 3D graphical representation of φ at $r = 10$ – recall the axial symmetry; (right panels) radial profile with an angular cut at $\theta = \frac{\pi}{2}$.

As we focus on the shape of the scalar field (see Fig. 2.8), it is noticeable that an increase in g_e, originates a growth in the width of the peak and a small decrease in its amplitude, *i.e.*, the peak becomes bulkier. Indeed, the maximum amplitude is $\varphi_{max} = 0.9822$, occurring at $r = 5.713$ for $g_e = 0.0$; it is $\varphi_{max} = 0.9819$ at $r = 5.7916$ for $g_e = 0.010$; and it is $\varphi_{max} = 0.9754$ at $r = 7.4201$ for $g_e = 0.035$. For the latter, the maximum suffers a deviation of almost 50% and a decrease of 7% in relation to the ungauged, spinning solution (with the same ω_1).

With the addition of g_e, an electric field emerges inside the Q-balls. With the increase in g_e a repulsive electric force, proportional to the density of the scalar field and able to push it apart, emerges.

Even so, the number of particles also increases and consequently the self-interaction intensity, creating a wider and smaller peak.

Consider now the spectral decomposition of φ – Fig. 2.9. It is noticeable that the first spectral function ($\mathbf{f}_1$) is always negative and possess the greatest amplitude. Recall that $\mathcal{P}_1^1 = -(1-\cos^2\theta)^{\frac{1}{2}} \leqslant 0$. Thus the $\mathbf{f}_1$ gives a *positive* contribution to φ, indeed the leading one, *cf*. Fig. 2.8. The peak of this first spectral mode's spatial distribution shifts to greater r as g_e increases. Such a behavior, together with an increase in the broadness of the correspondent peak, follows the trend of the numeric φ.

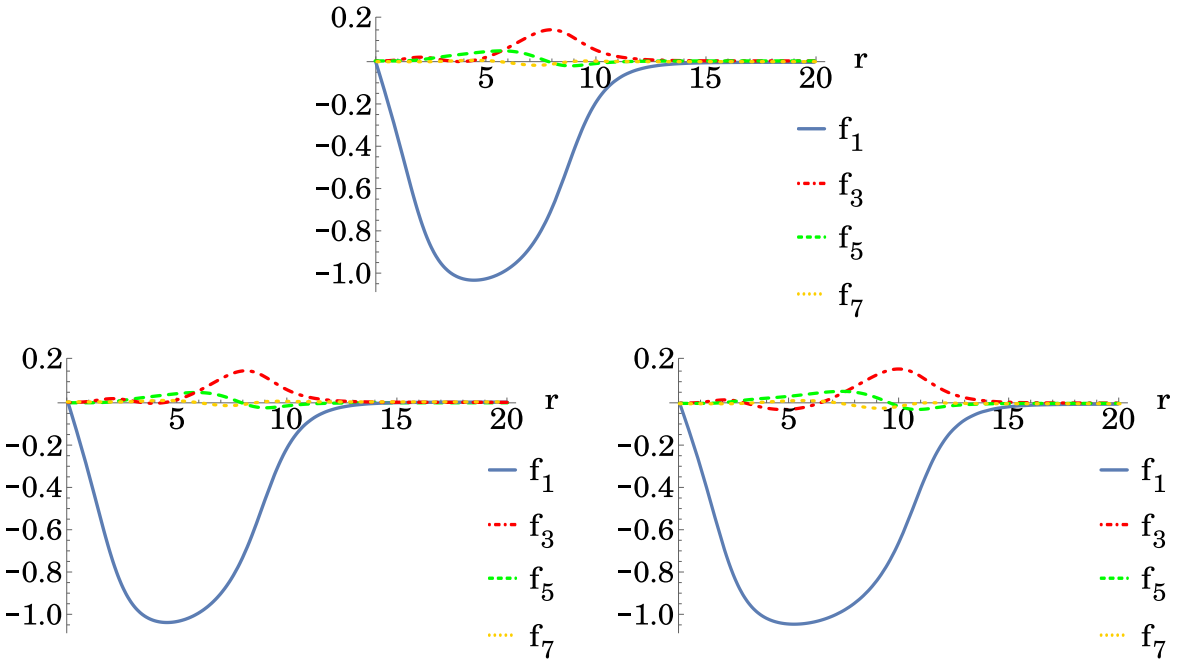

Figure 2.9: Spectral decomposition of the solution with $\omega_1 = 0.60$ into the first four spectral functions $\mathbf{f}_l$. (Top) $g_e = 0.0$; (bottom left) $g_e = 0.010$; (bottom right) $g_e = 0.035$.

The second spectral function ($\mathbf{f}_3$), on the other hand, is almost everywhere positive with the exception of a concavity in $r \sim 3$, where $\mathbf{f}_3$ takes some negative values. Such a behavior differs from $\mathbf{f}_1$, whose associated Legendre function does not change sign. This implies that, in that region, the contribution of $\mathbf{f}_3$ is small and tends to decrease (increase) the total amplitude of φ dependending on $\mathcal{P}_3^1$ being positive (negative). In the rest of the radial domain, the inverse behavior occurs. Concerning the g_e dependence of $\mathbf{f}_3$, one observes an increase of the negative concavity with its growth.

This variation with g_e is not a specific behavior of $\mathbf{f}_3$; we can observe that the third spectral function ($\mathbf{f}_5$) also possess a zero that changes with g_e. Also, different from the other values of ω (presented below), even if the major contribution comes from the first and second spectral functions, for some values of r, $\mathbf{f}_5$ possess a greater impact than $\mathbf{f}_3$.

At last, observe that the contribution of the fourth spectral function ($\mathbf{f}_7$) is really small; a result in agreement with the error study (Sec. 2.3.1). Moreover, the crescent g_e implies an increase in the $\mathbf{f}_5$ and $\mathbf{f}_7$ contributions.

If we now look at Table 2.3, where the Noether charge contribution of each $\mathbf{f}_l$ is presented, the same behavior as in Fig. 2.9 can be seen; $\mathbf{f}_1$ takes more than 90% of the Noether charge contribution, followed by $\mathbf{f}_3$ with $\sim 5\%$. In the spectral functions graphical representation (Fig. 2.9), the increase in g_e originates an increase in the impact of the higher $\mathbf{f}_l$. The first spectral function suffers a reduction of its Noether charge contribution, as the following modes suffer an increase. A fact easily verified in the total Noether charge contribution of the first four $\mathbf{f}_l$. The increase of g_e originates a reduction from 99.9809% for $g_e = 0.0$, to 99.5228% for $g_e = 0.035$. The higher modes are becoming more important.

Table 2.3: Relative Noether charge component of $\mathbf{f}_l$, in %, for $\omega_1 = 0.60$ and three different g_e values.

g_e	$\mathbf{f}_1$	$\mathbf{f}_3$	$\mathbf{f}_5$	$\mathbf{f}_7$	Total
0.0	94.4821	4.8731	0.5563	0.0694	99.9809
0.010	94.4577	4.8817	0.5680	0.0712	99.9786
0.035	93.9607	5.0898	0.7823	0.1200	99.5228

If we now focus our study in the energy portion of each $\mathbf{f}_l$ for $g_e = 0.0$, the calculation and analysis turns a little bit trickier due to the presence of cross terms. Such terms arise from the presence of 4 and 6 powers – in the potential U – and an angular derivative (∂_θ) of φ in the energy integral (2.17).

In Table 2.4 is introduced, for ω_1 and $g_e = 0.0$, the relative energy components of each spectral function (E_l) and correspondent mixing ($E_l \cdot E_{l'}$). The latter gives an idea of the coupling degree between the distinct $\mathbf{f}_l$.

For this analysis, all the different possible powers of $\mathbf{f}_l$ present on a given mix, are considered together. In other words, during the energy calculation, there will be cross terms with different powers of two (or more) modes that will be considered together (*e.g.* $\mathbf{f}_1^2 \cdot \mathbf{f}_3$ is considered together with $\mathbf{f}_1 \cdot \mathbf{f}_3^2$). Also, for simplicity, let us consider only the first three $\mathbf{f}_l$. Note that, this type of energy analyses, is only applicable to the ungauged, spinning Q-ball solutions since E is only spectral function dependent, *cf.* (2.17).

Table 2.4: Relative energy component of $\mathbf{f}_l$, in %, for $\omega_1 = 0.60$ and $g_e = 0.0$.

g_e	E_1	E_3	E_5	$E_1 \cdot E_3$	$E_1 \cdot E_5$	$E_3 \cdot E_5$	$E_1 \cdot E_3 \cdot E_5$	Total
0.0	98.9301	9.9613	1.8260	−7.6212	−1.7198	−0.0737	−1.0572	100.2475

As observable, if we sum the energy components of the "pure" spectral functions (without the mixing), the relative energy value is higher than 100% – look at $E_1 + E_2 = 108.8914$. Such an excess of energy is then compensated by the cross terms that are all negative. The latter's are mainly associated with the mixing coming from the high powers of φ – present in U – that allows the associated Legendre functions integral to be negative.

From the energy contribution of each $\mathbf{f}_l$, one can notice that, as with the Noether charge, the principal component is associated with the first spectral function, E_1. Even more, the mixing between the first and the second mode is the strongest ($E_1 \cdot E_3$); while the mixing between the second and the third spectral functions is the weaker ($E_3 \cdot E_5$). The latter is also surpassed by the three mixing term.

At last, the fact that the total energy contribution from the first three terms is higher than E, indicates the requirement of higher l spectral functions. In an naive observation, it seems that, the higher "pure" energy contributions decreases, and the energy excess will be mostly compensated by the mixing terms that include the first spectral function.

The electric component of a gauged, spinning Q-ball solutions $\big(g_e = \{0.010, 0.035\}\big)$, is described by an electric potential V, or an electric field $\vec{E}$. Fig. 2.10 shows the electric potential amplitude (left), as function of r and $\theta = \frac{\pi}{2}$, and the multipolar functions $\mathbf{V}_l$ (right). For the two values of g_e, we obtain a maximum amplitude of $|V_{max}| = 0.2624$ at $r = 2.8129$ for $g_e = 0.010$ and $|V_{max}| = 1.3101$ at $r = 3.0494$ for $g_e = 0.035$.

Let us start by observing the electric potential amplitude and multipolar functions. The former starts at a given amplitude, that increases with g_e, reaches a maximum amplitude ($|V_{max}|$) and then decays as $\frac{1}{r}$. Such a behavior is intrinsically different from the φ case (Fig. 2.8), besides not starting at zero for $r = 0$, the electric potential also possess a well shape that goes from $r = 0$ up to the position of $|V_{max}|$. The electric potential is connected to the scalar field by g_e, the former being created by the spatial charge distribution of the latter. So, the fact that there is no charge at $r = 0$, does not imply a null electric potential; the charge distribution around the origin creates a non-zero V value in relation to $r \to \infty$. V_{max} occurs at a smaller r than the maximum of the scalar field.

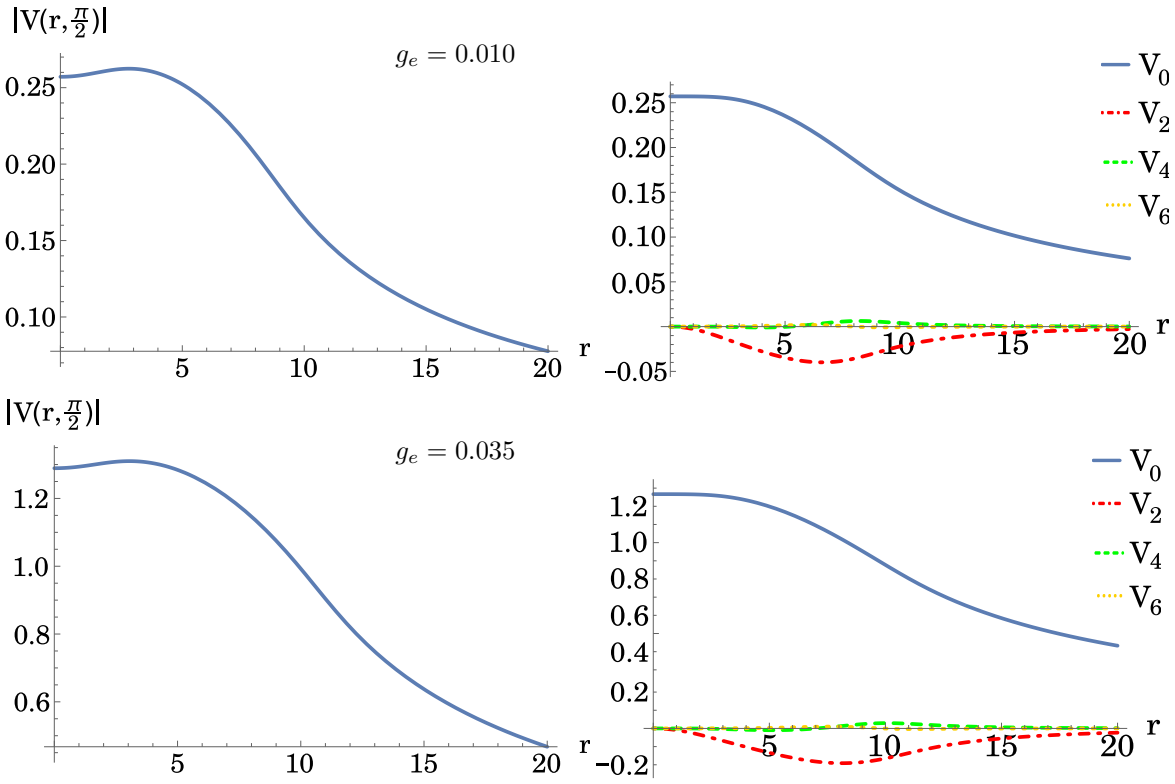

Figure 2.10: Electric potential V for $\omega_1 = 0.60$ and (top) $g_e = 0.010$; (bottom) $g_e = 0.035$. (Left) electric potential amplitude $\left|V(r, \frac{\pi}{2})\right|$; (right) first four multipolar functions $\mathbf{V}_l$ as a function of r.

Concerning the multipolar expansion, the major contribution comes from the *monopole function* ($\mathbf{V}_0$), being followed by the *quadrupole function* ($\mathbf{V}_2$). The latter possesses a constant negative sign due to the sign of $\mathcal{P}_2^0$, and plays an important role in the shape of V.

Observe the multipolar functions, Fig. 2.10 (right), $\mathbf{V}_0$ starts at the maximum for $r = 0$ and then decays. On the other hand, $\mathbf{V}_2$ starts at zero, reaches the maximum and then decays. Since $\mathcal{P}_2^0$ is negative, it originates a positive $\mathbf{V}_2$ contribution that is added to $\mathbf{V}_0$. The connection between the two different multipole behaviors will then be the main responsible for the well shape near the origin. At last, note that the radial dependence of a $\mathbf{V}_l$, possesses a similar behavior for the two values of g_e.

Since we have the first four multipolar functions, it is possible to perform a 2D-spacial comparison between the electric potential and the multipolar decomposition. To do so, let us plot in Fig. 2.11 a cut along the z-axis ($\phi = c^{te.}$) for: the electric field ($\vec{E}$) lines, the electric potential V, and the equipotential lines associated to the latter. Note that the outer blue region is not placed as a high electric potential, but as contrast to the yellow region.

In Fig. 2.11 (left) is graphically represented the electric potential, electric field and equipotential lines, obtained through the FORTRAN numerical code (for $z < 0$), and through the multipolar decomposition (for $z > 0$), using the first four $\mathbf{V}_l$. As observable, for ω_1 and $g_e = \{0.010, 0.035\}$, the two hemispheres are almost indistinguishable at naked eye. The equipotential lines possess a continuity at $z = 0$ and the electric potential seems to be perfectly symmetric under the xy-plane reflection. In relation to the electric field $\vec{E}$, at $r \approx 20$, there seems to exist a different concentration of lines between the two hemispheres (observe the corners). The difference is originated by the gradient of V, that is enhancing the small variations between the multipolar decomposition and the numerical V.

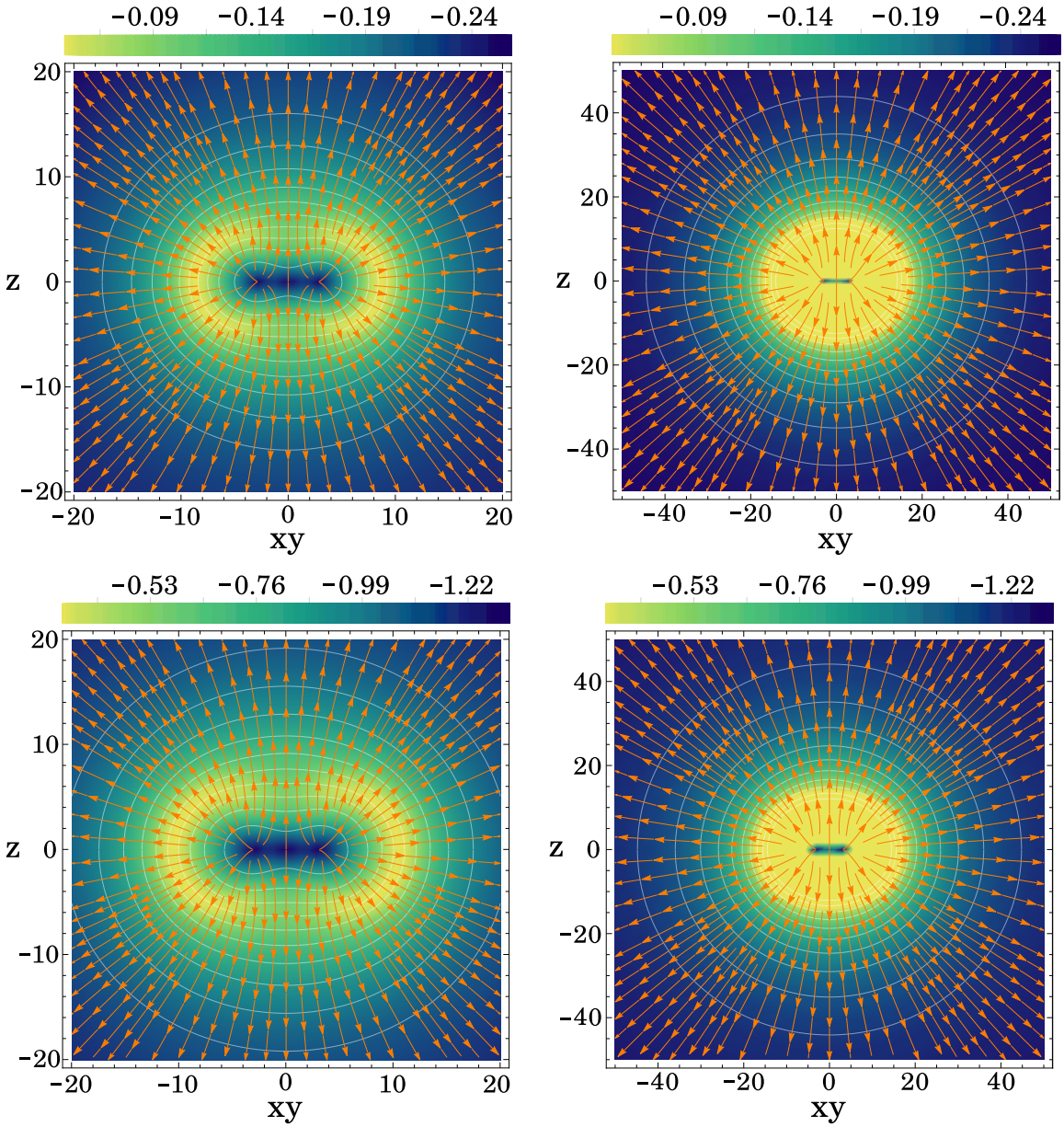

Figure 2.11: Graphical representation of the electric potential (color plot), equipotential lines, and electric field $\vec{E}$ lines for $\omega_1 = 0.60$ and (top) $g_e = 0.010$; (bottom) $g_e = 0.035$. (Left) composed graphic with the multipolar decomposition in the positive z-axis, and the numeric V in the negative z-axis. (Right) Zoom out of the numeric V. Outer blue region placed as contrast.

Concerning the spatial distribution of V and $\vec{E}$ in Fig. 2.11 (right), one observes a monopolar configuration tendency for large r (V tends to circular configuration and the main component of the electric field is radial). With the increase in the radial zoom in, however, a more complex form surge. If we start at r small, Fig. 2.11 (left), the electric potential amplitude is $V(0)$. The latter then increases in amplitude as r increases, reaches a maximum of V_{max} and decreases after that. The same well shape behavior as in Fig. 2.10 (left).

Due to the 2D-spatial representation, the quadrupole function contribution is easier to observe. For small azimuthal angles (θ) the $\mathcal{P}_2^0$ is positive, giving a negative net $\mathbf{V}_2$ contribution, and a consequent decrease in the electric potential amplitude. As θ increases, there is a change in $\mathcal{P}_2^0$ sign.

The latter becomes negative, which originates a positive $\mathbf{V}_2$ contribution, and a consequent increase in the electric potential amplitude. The connection between the angular behavior of the quadrupolar term and the spherical monopolar term, gives arise to the general "peanut" shape of V.

If we now plot, in a 3D form, two equipotential surfaces of V (for 99%, purple, and 50%, blue, of $|V_{max}|$) and the electric field lines, Fig. 2.12, one can see the same shape as in the 2D case. As r increases, the equipotential surfaces starts to become spheric (see blue surface) and the electric field lines purely radial. For r small, there is a toroidal region where $|V|$ is high (see purple surface). Inside and at the center of the latter, the electric potential is smaller, creating the "peanut" shape in the 2D representation and the 3D toroidal shape.

Concerning the change in V with the change in g_e, it is observable an increase in the toroidal region thickness for the larger g_e solution. The latter, due to the increase of the φ distribution and consequent increase in the V radial distribution, possess now a larger inner toroidal radius. Such a behavior corresponds to the 3D representation of the increased width of the peak in Fig. 2.11. Even that in the latter it is not easily observable, in the 3D representation such a difference is clear.

Comparing now the general behavior of the two g_e non-trivial values, one observes a similar shape. For the higher g_e note an increase in radial distribution and amplitude of V, and consequently an increase in the electric field lines.

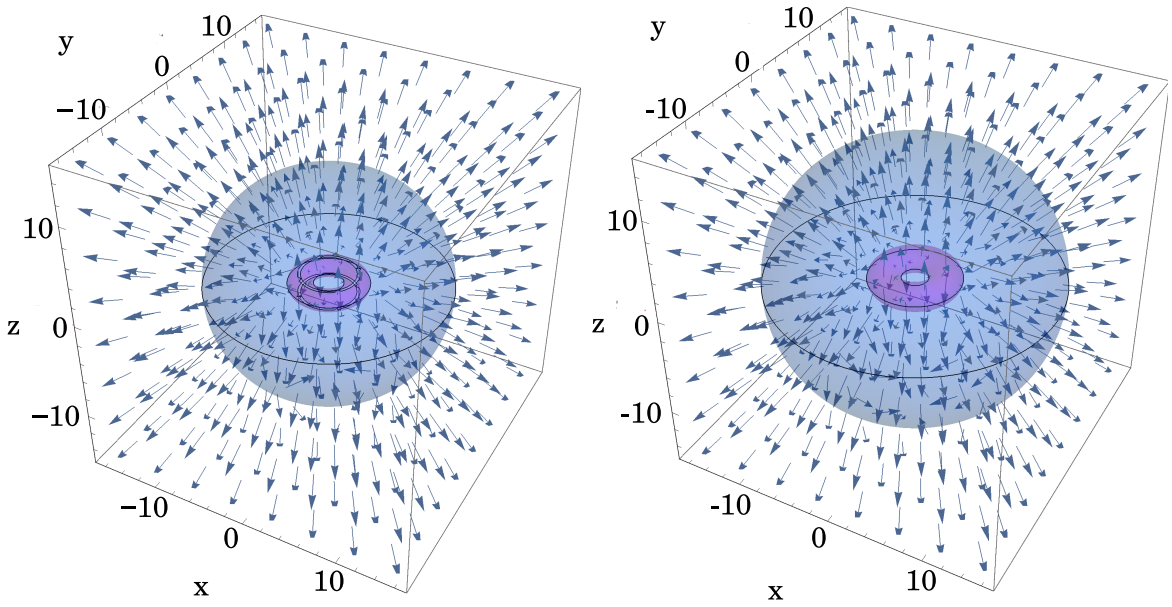

Figure 2.12: 3D graphical representation of the electric field and equipotential surfaces for $\omega_1 = 0.60$ and (right) $g_e = 0.010$; (left) $g_e = 0.035$. The equipotential surfaces represent 50% (blue) and 99% (violet) of $|V_{max}|$.

Finally, let us consider the magnetic field $\vec{B}$, Fig. 2.13. The main contribution for the shape of A_ϕ comes from the magnetic dipole, Table 2.5. The magnetic quadrupole, on the other hand, will be the responsible for increasing the radial distribution of $\vec{B}$ along the equatorial plane.

In the figure below, one can observe the comparative behavior of $\vec{B}$ (top) and the magnetic field originated trough the magnetic dipole (bottom). As noticeable, the magnetic field from A_ϕ possess a shape that tends to a magnetic dipole for large enough r. For the small r values, however, due to the finite size charge distribution, such a tendency does not hold. The interaction between the magnetic field and the latter gives rise to a more complex shape than the magnetic dipole. Let us not forget that, the dipole expansion is performed at infinity and lacks the real size of the magnetic source.

Concerning the magnetic quadrupole moment, the latter is smaller than the magnetic dipole moment. However, due to its spatial distribution, the latter will be the main responsible for the elongation

of the magnetic field lines at the equatorial (xy) plane. As already mentioned, due to the nature of the problem, the main component of the magnetic field is the dipole term. The quadrupole term will then be the reminiscent, at infinity, of the magnetic field lines coupling with the charge distribution and consequent complexity.

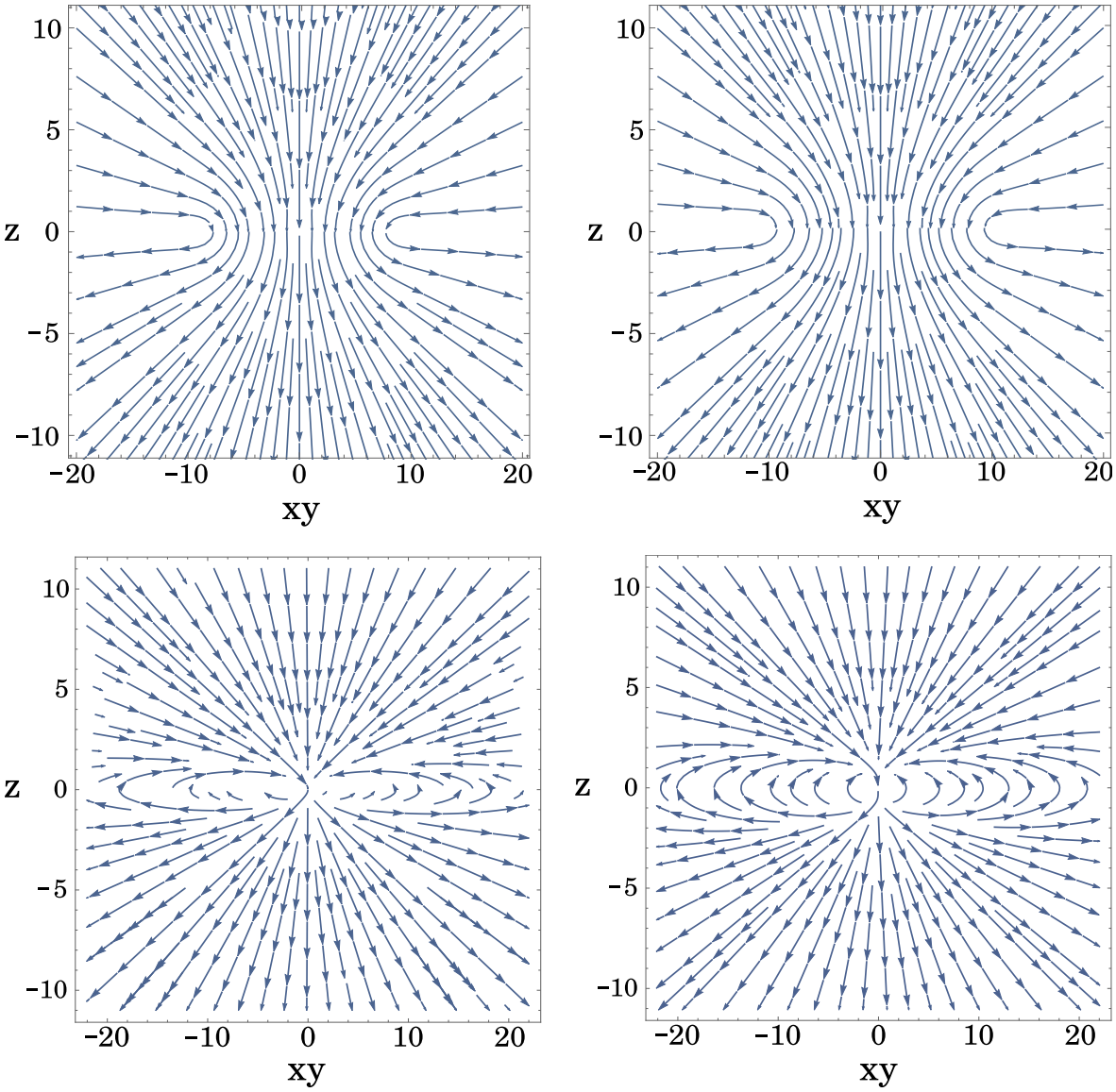

Figure 2.13: Magnetic field representation for the $\omega_1 = 0.60$ and (left) $g_e = 0.010$; (right) $g_e = 0.035$ solutions. (Top) Magnetic field obtained from the numeric A_ϕ; (bottom) magnetic field *solely* due to the μ_B, with the corresponding μ_B obtained from the numerical solution (see Table 2.5).

About the magnetic field evolution with the g_e increase, an increase in the magnetic field intensity occurs. Such a behavior is easily justified by the increase in the number of charged particles and the correspondent individual charge, besides the increase in the angular momentum $J = mQ$. Even so, the fact that the charge distribution for the large g_e is bigger than the smaller case, avoids a possible comparison between the two magnetic representations in Fig. 2.13.

If we then compare the magnetic characteristic quantities, one observes the general increase in the

dipole magnetic moment and the magnetic quadrupolar moment due to the increase in the magnetic field. Even so, such an increase is not equal to both the μ_B and q_B. The latter increases more with the increase of g_e than the former, it goes from 2.8× smaller than μ_B for $g_e = 0.010$, to 2.1× for $g_e = 0.035$. With the increase of the electric charge distribution, the quadrupole moment and higher modes that describes the more complex coupling between the latter and the originated magnetic field gain a more important role.

At last, let us compare some of the intrinsic quantities obtained from the three fields that characterize a(n) (un)gauged, spinning Q-ball. To do so, observe Table 2.5. For the Noether charge (number of particles), one obtains for $g_e = 0.0$, $Q = 1859.0341$; for $g_e = 0.010$, one has $Q = 1920.8682$, and for $g_e = 0.035$, we have $Q = 3267.3575$. This represents an increase in the number of scalar particles with the increase of g_e. There are more scalar particles, each with a greater charge, meaning a higher net electric charge Q_e. A similar trend can be observed for the energy: an increase of E with the increase of g_e. Since there is an increase in the number of particles present in the soliton, there is also an increase in the scalar energy (energy associated with the scalar field). Even more, since these particles are becoming more charged, both the electroestatic energy and magnetostatic energy increase, leading to an increase in the total energy.

Table 2.5: Characteristic quantities of a(n) (un)gauged, spinning Q-ball with $\omega_1 = 0.60$.

g_e	Q	E	Q_e	μ_B	q_B	γ_B
0.0	1859.0341	1299.4703	0.0	0.0	0.0	0.0
0.010	1920.8682	1344.2191	−1.5230	−1.2667	−0.4493	0.0116
0.035	3267.3575	2493.8413	−9.1052	−7.9258	−3.7330	0.0433

At last, note that all the electromagnetic characteristic quantities (Q_e, μ_B and γ_B) possess the same behavior. For the ungauged, spinning Q-ball, due to the absence of electrically charged particles, they are all zero. In the gauged spinning case, the values are around the same and present an increase with the increase in g_e. Such a similar behavior is not strange if we consider the relation between them: the magnetic moment is originated by the electric charge distribution; while the gyromagnetic factor relates the magnetic dipole moment and the angular momentum ($\gamma_B = \frac{|\mu_B|2M}{QJ}$). On a final note, observe that γ_B increases with the growth of g_e. For now it is not possible to conclude if γ_B tends for a given value, however, one observes that it is g_e dependent.

2.4.2 Solutions with $\omega_2 = 0.92$

Let us now decompose the (un)gauged, spinning Q-ball solution with $\omega_2 = 0.92$. In the latter, for the ungauged spinning case, both $E = 182.1101$ and $Q = 175.1926$ correspond to the energy and Noether charge minimum (see Fig. 2.3). Concerning the gauged, spinning Q-ball solution, the maximum value for the gauge coupling constant is located around $g_e^{max} = 0.18$. Hence, we will consider solutions with $g_e = \{0.0, 0.010, 0.150\}$.

In Fig. 2.14, it is shown, for the three values of g_e, the 3D graphical representation of φ and a radial cut of the latter at $\theta = \frac{\pi}{2}$. As observable, with the exception of a broad peak, the shape of φ follows the same template as in ω_1. The scalar field starts at zero for $r = 0$; with the increase of r, φ grows rapidly to φ_{max}, after which it decays exponentially.

Comparing with ω_1, the current Q-ball solutions present an increase in the maximum amplitude of φ and a decrease in the broadness of the peak, *i.e.*, the peak became sharper. Observe Fig. 2.14 and $\varphi_{max} = 0.6323$ at $r = 3.3320$ for $g_e = 0.0$; $\varphi_{max} = 0.6331$ at $r = 3.3305$ for $g_e = 0.010$, and $\varphi_{max} = 0.8144$ at $r = 3.2117$ for $g_e = 0.150$. Comparatively, the radial coordinate of φ_{max}, as well as the radial decaying tail (now $r \sim 7$) have suffered a reduction. The radial decaying tail also seems to be more gradual, implying a slower decay rate.

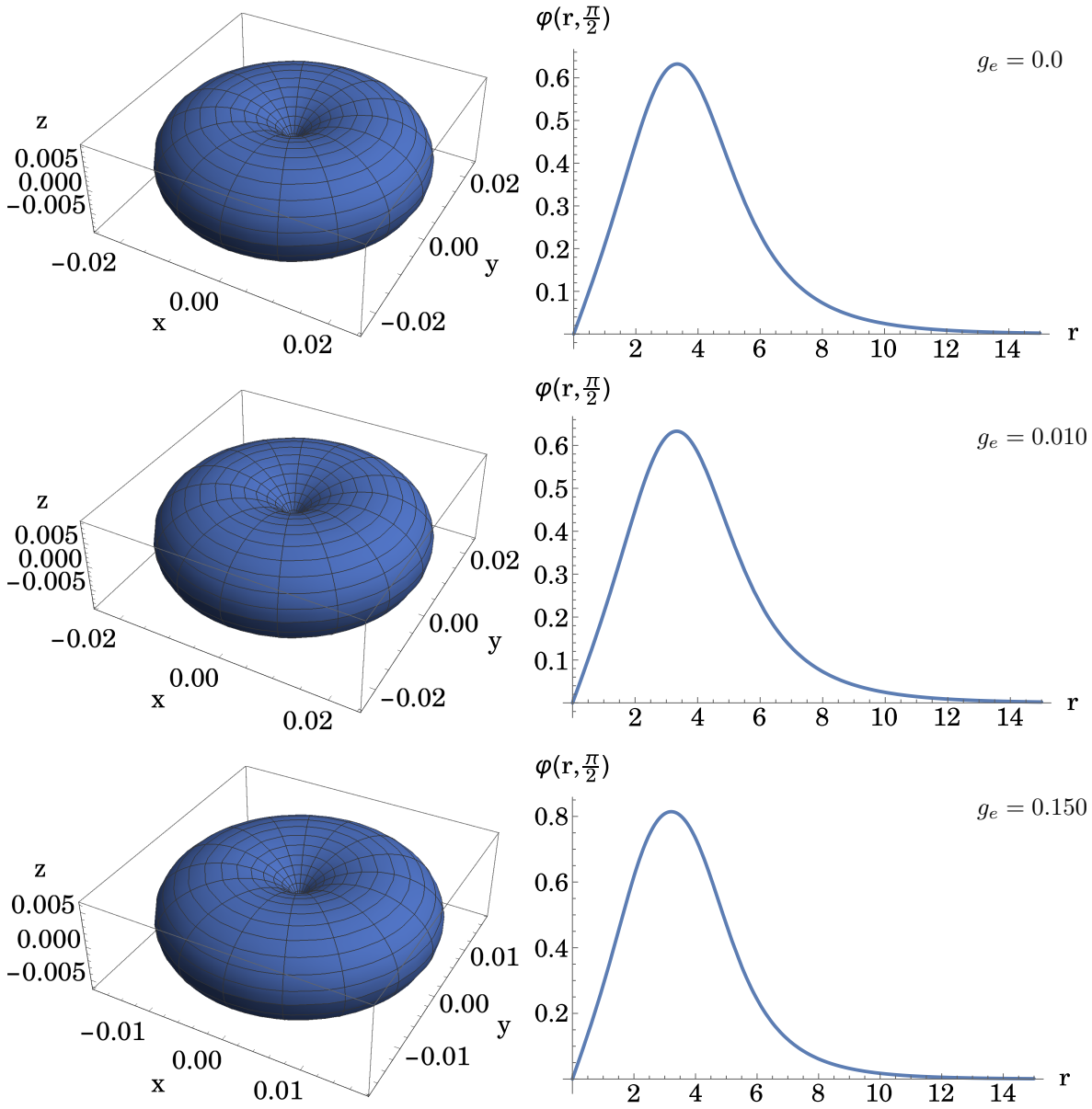

Figure 2.14: Graphical representation of φ for $\omega_2 = 0.92$ and (top) $g_e = 0.0$; (middle) $g_e = 0.010$, (bottom) $g_e = 0.150$. (Left panels) 3D graphical representation of φ at $r = 10$ – recall the axial symmetry; (right panels) radial profile with an angular cut at $\theta = \frac{\pi}{2}$.

In relation to the variation of φ with the change of g_e, for this parameter solutions, the latter possess a smaller impact in the scalar field spatial distribution than in the ω_1 case. For ω_2, the radial position of φ_{max} as changed less than 10% between the $g_e = 0.0$ and the $g_e = 0.150$ case, while for ω_1 the change between the maximum $g_e = 0.035$ and the ungauged case ($g_e = 0.0$) was around 50%. For ω_2, an increment of g_e implies an increase in φ_{max} and a decrease in the correspondent radial position. Such a behavior indicates that, for ω_2, the growth in the number of particles (Noether charge) associated with the increase of g_e, causes an increment in the attractive self-interaction that is superior than the increase in the electric repulsion. The Q-ball shrinks and becomes sharper.

In Fig. 2.15, one can observe the spectral functions $\mathbf{f}_l$ associated with the three current g_e. Again, the first spectral function ($\mathbf{f}_1$) is always negative, and, together with the second spectral function ($\mathbf{f}_3$), constitute the major contributors for the shape of φ.

The second spectral function has now lost the concave region as well the negative region associated with it. Since this region does not exist anymore, there is no need for the compensation from the third and fourth spectral functions, and hence they became smaller.

In relation to the higher spectral functions, the third spectral function ($\mathbf{f}_5$) has now a constant negative sign. About the fourth spectral function ($\mathbf{f}_7$), it is now almost constant and equal to zero. The higher spectral functions suffered a decrease in their amplitude and, consequently, in their impact.

At last, note that the maximum of $\mathbf{f}_3$ is always positioned at the right of the "maximum" (actually minimum) of $\mathbf{f}_1$. Such a behavior increases the size of the decaying tail.

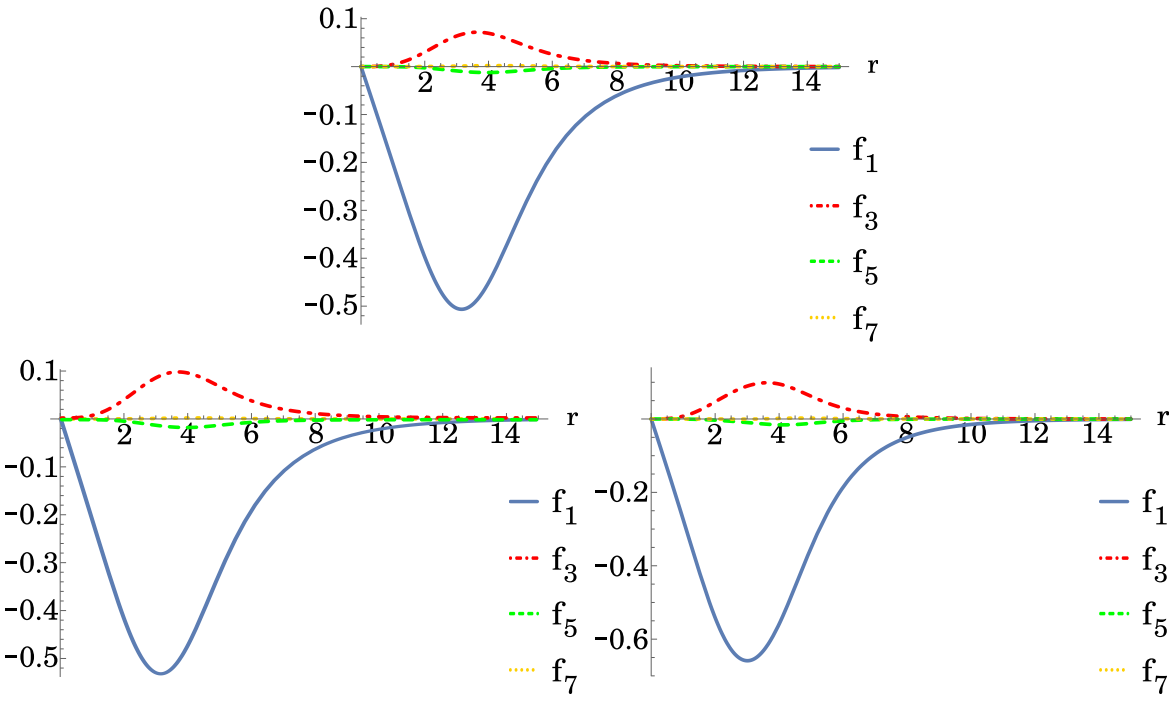

Figure 2.15: Spectral decomposition of the solution with $\omega_2 = 0.92$ into the first four spectral functions $\mathbf{f}_l$. (Top) $g_e = 0.0$; (bottom left) $g_e = 0.010$; (bottom right) $g_e = 0.150$.

For these parameters solutions, besides the change in the format of $\mathbf{f}_l$ from the change in the shape of φ, there is no noticeable alteration between the three g_e cases. However, as we look to the Noether charge component of each $\mathbf{f}_l$, Table 2.6, it is possible to observe an evolution of the individual contributions with the increase of g_e.

Table 2.6: Relative Noether charge component of $\mathbf{f}_l$, in %, for $\omega_2 = 0.92$ and three different g_e values.

g_e	$\mathbf{f}_1$	$\mathbf{f}_3$	$\mathbf{f}_5$	$\mathbf{f}_7$	Total
0.0	94.9834	4.6588	0.2142	0.0103	99.9239
0.010	94.9808	4.7894	0.2144	0.0080	99.9926
0.150	93.9229	5.8246	0.2451	0.0067	99.9993

As before, the first and second spectral functions, together, are responsible for more than 99% of Q. With just the first four $\mathbf{f}_l$ one could obtain a minimum of 99.9% of the Noether charge (for $g_e = 0.0$). In relation to the ω_1 solution, one can also observe that, an increase in g_e originates a decrease in the $\mathbf{f}_1$ contribution and an increase in the higher $\mathbf{f}_l$ contributions.

Different from the previous solutions, $\mathbf{f}_5$ and $\mathbf{f}_7$ have now a smaller contribution, while $\mathbf{f}_1$ and $\mathbf{f}_3$ contributions have increased. Furthermore, the total contribution of the first four $\mathbf{f}_l$ is now closer

to 100%. $\mathbf{f}_1$ and $\mathbf{f}_3$ increased more than the decrease of $\mathbf{f}_5$ and $\mathbf{f}_7$. The first and second spectral functions are now more able to describe φ.

For the ungauged spinning solution, all the E components follow the same behavior as before, Table 2.7. The first and second spectral functions are the major contributors and the strongest mixing occurs between them. Even so, comparatively to ω_1, there was a decrease in the individual E_l components and an increase in the mixing terms amplitude. With this two opposite behaviors, the total energy is now closer to 100%.

Table 2.7: Relative energy component of $\mathbf{f}_l$, in %, for $\omega_2 = 0.92$ and $g_e = 0.0$.

%	E_1	E_3	E_5	$E_1 \cdot E_3$	$E_1 \cdot E_5$	$E_3 \cdot E_5$	$E_1 \cdot E_3 \cdot E_5$	Total
E_l	96.5942	6.9717	0.4303	−3.5039	−0.0280	−0.0012	−0.4283	100.0348

The increase in the mixing terms also implies an increase in the spectral functions coupling. So, based on the current data, one can observe that at the minimum of E and Q, the Q-ball solutions possess the major coupling between spectral modes.

In a gauged spinning Q-ball, besides the existence of a scalar field (φ), there is also an electric field ($\vec{E}$) and a magnetic field ($\vec{B}$). The latter will be treated ahead. About the electric component of our gauged solutions $\left(g_e = \{0.010, 0.150\}\right)$, a multipolar decomposition of the electric potential V will be performed. In Fig. 2.16 is plotted, as a function of r and $\theta = \frac{\pi}{2}$, the electric potential amplitude $|V|$ (left) and the first four multipolar functions (right) that decompose the latter. For the two non-trivial values of g_e, the electric potential reaches an amplitude maximum of $|V_{max}| = 0.0372$ at $r = 2.5408$ for $g_e = 0.010$ and $|V_{max}| = 0.7570$ at $r = 2.4240$ for $g_e = 0.150$.

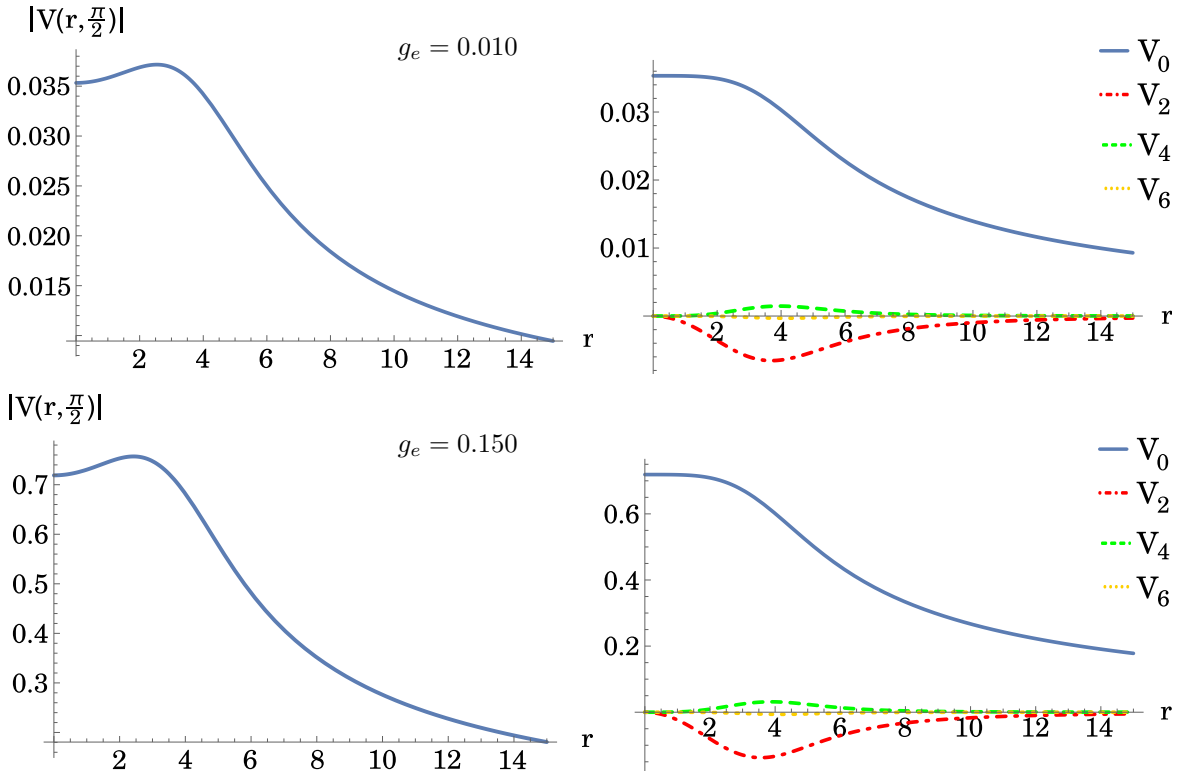

Figure 2.16: Electric potential V for $\omega_2 = 0.92$ and (top) $g_e = 0.010$; (bottom) $g_e = 0.150$. (Left) electric potential amplitude $\left|V(r, \frac{\pi}{2})\right|$; (right) first four multipolar functions $\mathbf{V}_l$ as a function of r.

Concerning the form of V and respective $\mathbf{V}_l$, the same initial well shape occurs. The latter is, again, mostly molded by $\mathbf{V}_0$ and $\mathbf{V}_2$ functions. Different from ω_1, one observes an increase in the $\mathbf{V}_4$ contribution in the region of $|V_{max}|$. Also related to the latter is the absence of a zero, $\mathbf{V}_4$ is now always positive. With this fact, and recording that for $\theta = \frac{\pi}{2}$, $\mathcal{P}_4^0 > 0$, one observes that $\mathbf{V}_4$ together with $\mathbf{V}_2$ are now originating a higher maximum. The well shape is more accentuated. Observe that for ω_2, $|V_{max}|$ is $\sim 1.05\times$ larger than $\big(V(0)\big)$, while for ω_1, $|V_{max}|$ is only ~ 1.02 times $V(0)$.

In relation to the V description by $\mathbf{V}_l$, and how this description evolves with g_e, observe Fig. 2.17. In it, is graphically represented, in 2D, the electric field lines, the equipotential lines and the electric potential obtained from the two descriptions. In the latter, the space is divide at $z = 0$: for $z < 0$ is the numerical V, and for $z > 0$ is the multipolar decomposition with four $\mathbf{V}_l$.

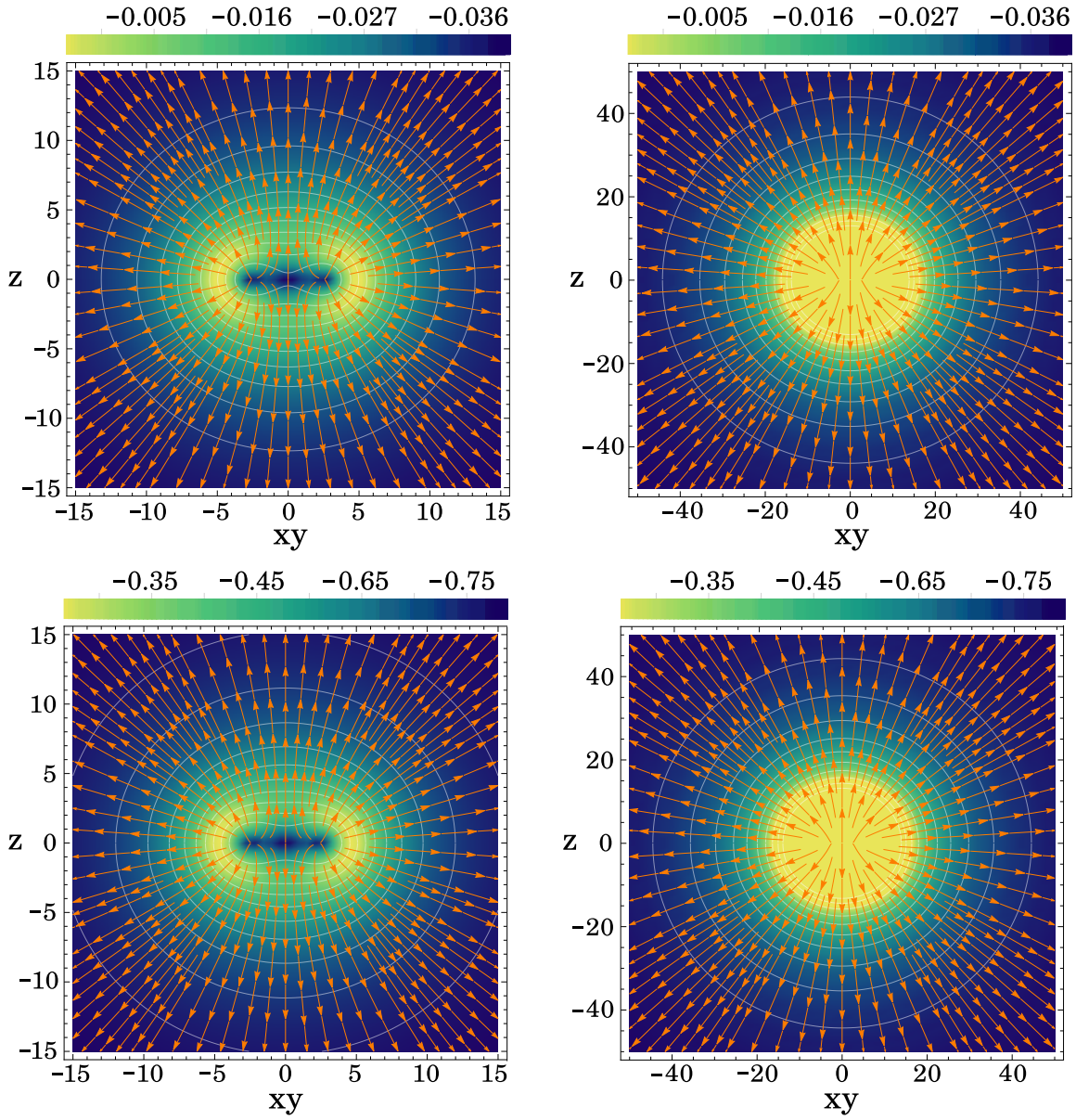

Figure 2.17: Graphical representation of the electric potential (color plot), equipotential lines, and electric field $\vec{E}$ lines for $\omega_2 = 0.92$ and (top) $g_e = 0.010$; (bottom) $g_e = 0.150$. (Left) composed graphic with the multipolar decomposition in the positive z-axis, and the numeric V in the negative z-axis. (Right) Zoom out of the numeric V. Outer blue region placed as contrast.

For ω_2 the two hemispheres are almost indistinguishable at naked eye, observe also Fig. 2.18. The equipotential lines are continuous at $z = 0$, and, V seems symmetric under reflection in the xy-plane. The only noticeable difference comes, again, from the electric field. At the corners, $\vec{E}$ presents a differences between the the numerically obtained V and the multipolar decomposed.

Also to notice is the "peanut" shape, a signature of the quadrupole function's impact. In relation to the increased importance of $\mathbf{V}_4$, Fig. 2.17 (left) does not present an observable alteration.

For the large scale (right) the electric potential and electric field tend to a monopole configuration. Actually, since this is a more compact object, for the same scale as in ω_1, Fig. 2.11 (right), the electric components present a greater monopole tendency.

In the 3D graphical representation of the equipotential surfaces and electric field, Fig. 2.18, one observes that, for large r the equipotential surfaces tend to spheres and the electric field to be purely radial. For the smaller values of r, the electric potential is higher and possess a toroidal shape.

As in the 2D case, besides the small alteration in the scale and intensity of the electric potential, no noticeable difference exists between the two g_e cases. On the other hand, if we compare with the smaller ω_1 case, it is observable the increase in the compactness of the peak. The toroidal region is larger in radius but smaller in thickness, where the latter is the 3D representation of the width of the peak in Fig. 2.16 (left).

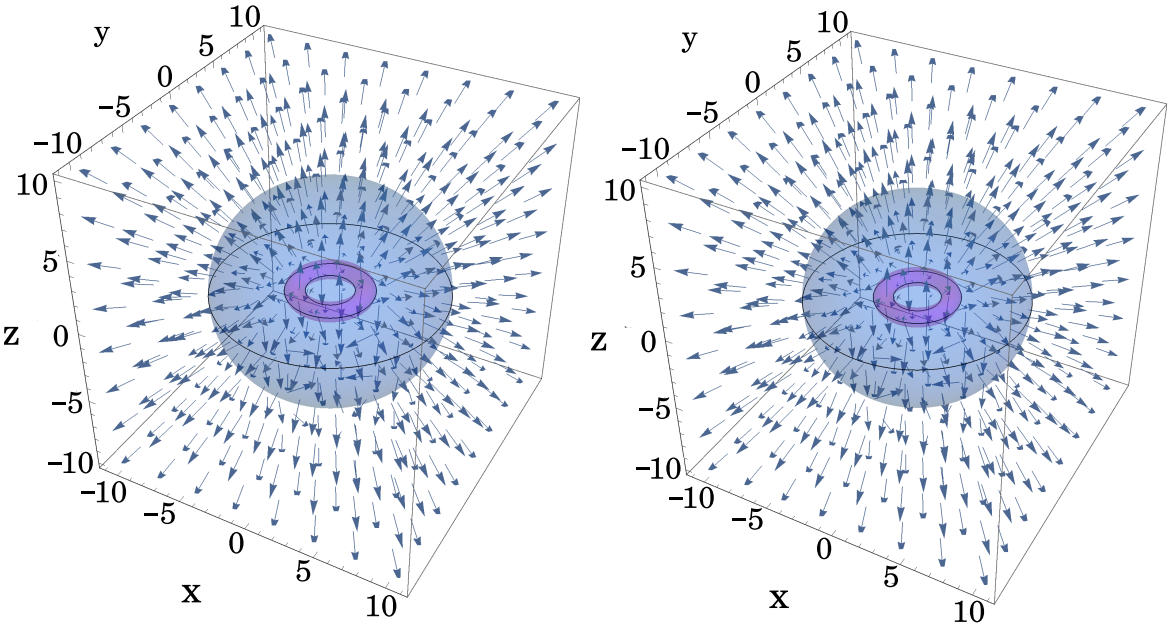

Figure 2.18: 3D graphical representation of the electric field and equipotential surfaces for $\omega_2 = 0.92$ and (right) $g_e = 0.010$; (left) $g_e = 0.150$. The equipotential surfaces represent 50% (blue) and 99% (violet) of $|V_{max}|$.

At last, in Fig. 2.19 is represented the magnetic field obtained for the two g_e's. Again, with the increase of r a tendency to a magnetic dipole emerges from $\vec{B}$. For these parameters solutions, in a first qualitative observation, one notices the increase in the $\vec{B}$ intensity and the respective growth of the xy-plane component with the increase of g_e.

Quantitatively, there was an increase in the magnetic dipole moment from $\mu_B = -0.0758$ for $g_e = 0.010$ to $\mu_B = -1.5546$ for $g_e = 0.150$, which is natural since there is more spinning electric charges. In relation to the magnetic quadrupole moment it possesses a value of $q_B = -0.0131$ for the small g_e value, and $q_B = -0.2510$ for $g_e = 0.150$, which represents an increase with the growth of g_e.

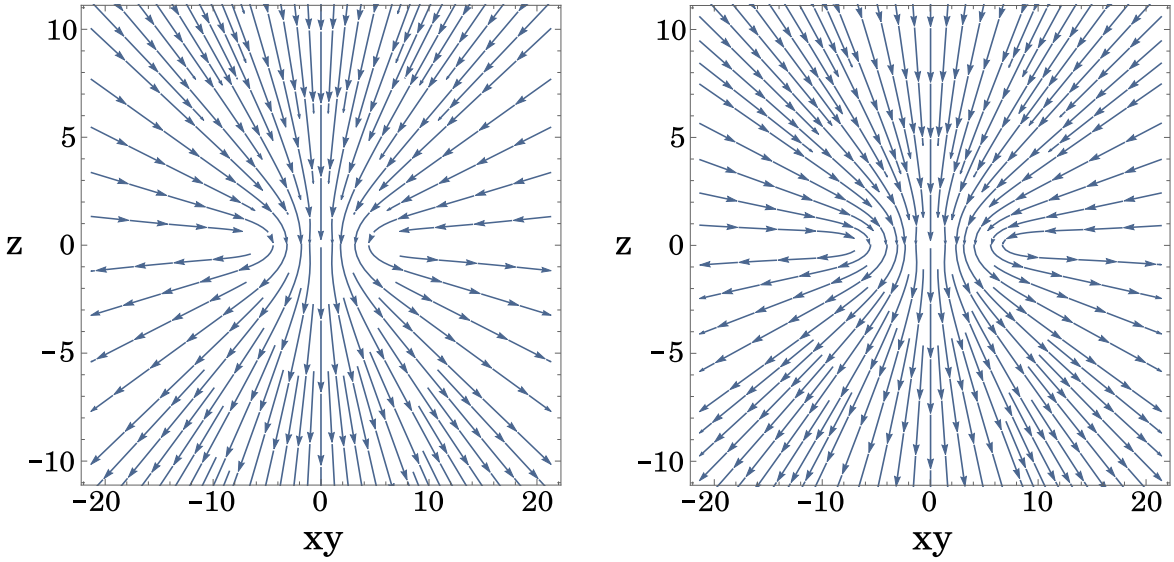

Figure 2.19: Magnetic field representation for $\omega_2 = 0.92$ and (left) $g_e = 0.010$; (right) $g_e = 0.150$.

If we then compare the evolution of q_B with the evolution of μ_B, one notices that for $g_e = 0.010$, the former is ~ 5.8 times smaller than the former, while for $g_e = 0.150$ the ratio is $\sim 6.24\times$. This time, even that the quadrupole moment has increased, the dipole moment has suffered a bigger growth, meaning that at infinity, $\vec{B}$, possess an increased dipole moment.

Table 2.8: Characteristic quantities of a(n) (un)gauged, spinning Q-ball with $\omega_2 = 0.92$.

g_e	Q	E	Q_e	μ_B	q_B	γ_B
0.0	175.1926	182.1101	0.0	0.0	0.0	0.0
0.010	175.3309	182.3105	−0.1395	−0.0758	−0.0131	0.0113
0.150	223.1432	283.7335	−2.6705	−1.5546	−0.2510	0.1985

In relation to all the characteristic quantities, one observes a magnitude increase with the growth of g_e. In comparison with the previous ω_1 note that, for both E and Q, even reaching a higher value of g_e, the resultant increase for ω_2 was smaller than the ω_1 case. There was an increase $\sim 50\%$ in the ω_2 case and an increase $\sim 80\%$ for the ω_1 case – between the $g_e = 0.0$ and the larger g_e solutions. Such a behavior can be associated with two facts: first, the value of $g_e = 0.150$ can be further way from g_e^{max} of ω_2 than $g_e = 0.035$ is from g_e^{max} of ω_1; and second, since the $\omega_1 = 0.60$ is at the start of the left divergence (see Fig. 2.3), the latter can be more unstable against the addition of electric charge than the $\omega_2 = 0.92$ case, that is situated at the minimum of the energy and Noether charge. At last, the gyromagnetic factor as suffered an increase with the increase of ω and g_e.

2.4.3 Solutions with $\omega_3 = 0.999$

Finally, at the right explosive divergence (see Fig. 2.3), a(n) (un)gauged, spinning Q-ball solution with $\omega_3 = 0.999$ will be decomposed – recall that, for $g_e = 0.0$, the maximum possible scalar field frequency is $\omega_+ < 1.0$. For the ungauged case, $E = 1015.6275$ and $Q = 1006.0801$. About the g_e domain for a gauged, spinning Q-ball with ω_3, the latter possess a maximum around $g_e^{max} = 0.23$. Due to that, we will consider the following three values $g_e = \{0.0, 0.010, 0.210\}$.

As a first analyses observe Fig. 2.20. In it, is shown for the three g_e values, the 3D graphical representation and radial cut at $\theta = \frac{\pi}{2}$ of φ. In the case with $g_e = 0.0$, $\varphi_{max} = 0.0749$ for $r = 24.2160$ with a radial decaying tail $r \sim 40$. For the gauged examples, $\varphi_{max} = 0.0814$ at $r = 22.5885$ for

$g_e = 0.010$ and $\varphi_{max} = 0.7993$ at $r = 3.4832$ for $g_e = 0.210$. For the latter, the radial decaying tail starts at $r \sim 10$, while for the former at $r \sim 40$.

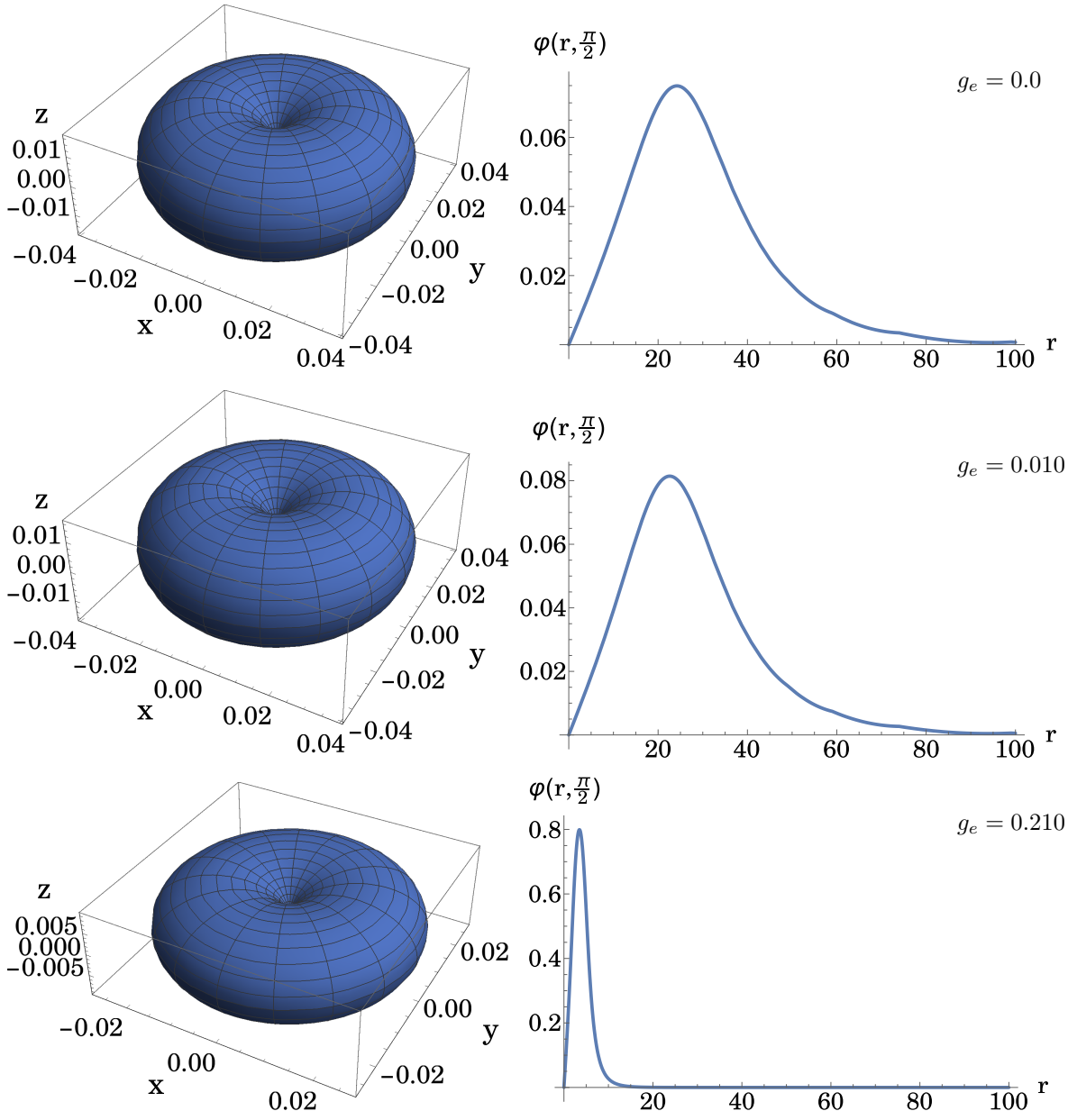

Figure 2.20: Graphical representation of φ for $\omega_3 = 0.999$ and (top) $g_e = 0.0$; (middle) $g_e = 0.010$, (bottom) $g_e = 0.210$. (Left panels) 3D graphical representation of φ at $r = 10$ – recall the axial symmetry; (right panels) radial profile with an angular cut at $\theta = \frac{\pi}{2}$.

Concerning the shape of φ for the $g_e = 0.0$ and $g_e = 0.010$ cases, it is noticeable an increase in the radial distribution and a decrease in the general amplitude of φ. The latter's possess a shallower and more diluted φ. On the other hand, with the increase of g_e a totally different behavior emerges, the spatial distribution of φ becomes compacter. The solution with $g_e = 0.210$ possess a thin and high peak, observe Fig. 2.20 (bottom).

By comparing with the smaller ω solutions, one observes for ω_3, a totally different behavior. While for ω_1 an increase in g_e originates an increase in the width and a decrease in the hight of the peak, for

ω_3 the opposite behavior occurs. The increase in g_e originates an increase in the compactness of φ.

As ω tends to ω_+, the self-interaction potential ability to support the highly oscillatory particles ceases, resulting in the dispersion of the soliton. On the other hand, the introduction of g_e originates an increase in the particle density ($|\varphi|$). The later will give an extra boost to the self-interaction potential, making it able to support the high ω's. However, the addition of g_e is a double-edged sword. Even that an increased value of g_e implies an amplified self-interaction potential, it also implies an increased electric repulsion that will ultimately disperse the soliton.

When the radial component is small, the self-interaction potential is strong and, together with the growth in φ, is able to support the increased electric repulsion and ω_3 dispersion. As r increases, the self-interaction potential intensity decreases, it is no longer able to support the repulsive/dispersive interactions and φ tends to zero. This creates a denser soliton but, globally, a soliton with fewer particles (Q). For the $g_e = 0.010$ case, the relative increase in the electric repulsion and particle density is small and is not easily observable.

If we perform the spectral decomposition for the three g_e solutions, one will observe the same general behavior as in Fig. 2.20. So, to easily observe the spectral functions of the $g_e = 0.210$ solution, the latter will be presented in a smaller radial scale, Fig. 2.21 (bottom right).

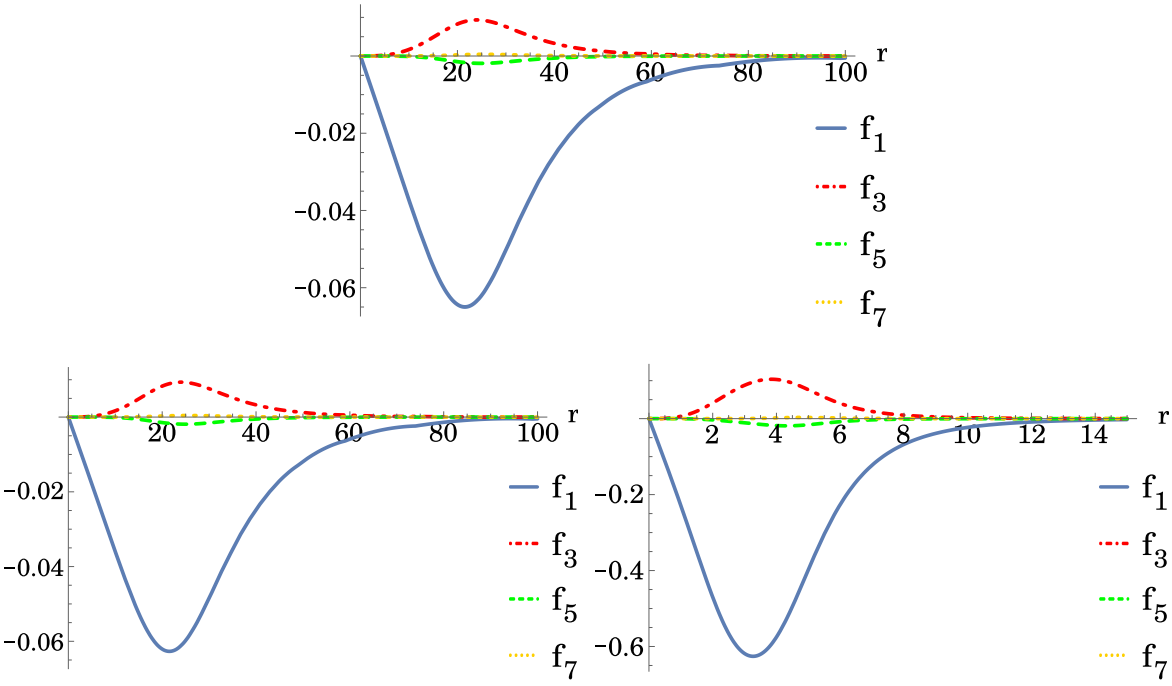

Figure 2.21: Spectral decomposition of the solution with $\omega_3 = 0.999$ into the first four spectral functions $\mathbf{f}_l$. (Top) $g_e = 0.0$; (bottom left) $g_e = 0.010$; (bottom right) $g_e = 0.210$.

About the general shape of the spectral functions, the same behavior as in all the ω cases is present. $\mathbf{f}_1$ is always negative, and is the main responsible for the shape of φ. $\mathbf{f}_3$ goes right after and is the second most important contributor for the shape of the scalar field. Even more, by looking at Table 2.9 and Fig. 2.21, it is possible to observe the increase in the $\mathbf{f}_3$ importance.

Concerning the higher spectral modes, it is possible to observe that $\mathbf{f}_7$ is again almost zero everywhere. On the other hand, $\mathbf{f}_5$ seems to suffer an increase in its impact with the g_e increase.

In relation to the spectral functions change with g_e, one observes a drift of the peak of $\mathbf{f}_3$ to the left. The latter is now closer to the radial position of the peak of $\mathbf{f}_1$, which creates a steeper decaying tail. The object is becoming more and more compact.

In Table 2.9 is presented the Noether charge component of each spectral function. As always, the

major contribution comes from the first (greater) and second spectral functions.

Table 2.9: Relative Noether charge component of $\mathbf{f}_l$, in %, for $\omega_3 = 0.999$ and three different g_e values.

g_e	$\mathbf{f}_1$	$\mathbf{f}_3$	$\mathbf{f}_5$	$\mathbf{f}_7$	Total
0.0	95.2489	4.4905	0.2454	0.0144	99.9992
0.010	95.1298	4.4993	0.2589	0.0156	99.9934
0.210	92.8488	6.7776	0.3609	0.0127	99.9999

If we now compare $\mathbf{f}_l$ contribution for ω_3 with the previous ω examples, for the two smaller values of g_e, one observes an increase in the $\mathbf{f}_1$ contribution and a decrease in the $\mathbf{f}_3$ contribution. Also to notice is the increase in the higher spectral functions contribution. The decrease in $\mathbf{f}_l$ contribution is being mainly complemented by the increase in first and third spectral functions.

Concerning the $\mathbf{f}_l$ contribution variation with the change of g_e, it is possible to observe, again, that an increase in g_e originates a decrease in the $\mathbf{f}_1$ contribution, and an increase in the higher modes. This behavior, together with the drift of $\mathbf{f}_3$ to the left, is at the origin of the increased compactness of φ. At last, note that the first and fourth spectral functions always suffer a decrease in its importance with the increase of g_e, while $\mathbf{f}_3$ and $\mathbf{f}_5$ suffer an increase.

Finally, let us observe the energy component of each spectral function (E_l) and crossing terms for $g_e = 0.0$, Table 2.10. In the latter, it is noticeable an increase in the separation of the $\mathbf{f}_l$ functions. The mixing terms are now much smaller and tend to zero, while the "pure" energy terms (E_l) tend to sum 100%.

Table 2.10: Relative energy component of $\mathbf{f}_l$, in %, for $\omega_3 = 0.999$ and $g_e = 0.0$.

%	E_1	E_3	E_5	$E_1 \cdot E_3$	$E_1 \cdot E_5$	$E_3 \cdot E_5$	$E_1 \cdot E_3 \cdot E_5$	Total
E_l	95.3071	4.4986	0.2482	-0.0570	-0.0010	-3.4101×10^{-6}	-0.0063	99.9896

To better understand this uncoupling behavior, recall that the main contributor for it are the fourth and sixth powers of φ present in U. Since these are high powers of φ, they are highly dependent in the magnitude of the latter: if φ is small, the high powers of it will be smaller; if φ is large, the high powers of it will be larger. On the other hand, observe that with the increase of ω, φ to becomes shallower, *i.e.*, the φ magnitude is becoming small everywhere. The high φ powers are becoming less and less important, which results in the decrease of the mixing. About the mixing originated by the angular derivative, it is not as directly dependent on the amplitude of each spectral function as U, and will create a residual mixing.

For the electric component of our gauged, spinning Q-ball solutions $\left(g_e = \{0.010, 0.210\}\right)$, a multipolar decomposition of the electric potential V will be performed, Fig. 2.22. In general, besides the different radial scales, both gauged solutions possess the usual form. An initial well shape which is followed by an $\frac{1}{r}$ decaying tail. At the maximum of the well (global maximum) the electric potential amplitude reaches $|V_{max}| = 0.0294$ at $r = 17.6649$ for $g_e = 0.010$ and $|V_{max}| = 1.0780$ at $r = 2.6930$ for $g_e = 0.210$. Concerning the depth of the initial well, one observes, again, an increase in the relative difference between the maximum and $V(0)$. The former is now, for $g_e = 0.210$, around $1.08\times$ larger than the latter. The previous difference for the $g_e = 0.010$ case is $\sim 1.05\times$, a value smaller than the higher g_e case, due to the relative small impact of $g_e = 0.010$.

As before, the main contributors for the shape of V are $\mathbf{V}_0$ and $\mathbf{V}_2$. In relation to the higher $\mathbf{V}_l$, one can observe that $\mathbf{V}_6$ continues to be the smaller and almost without any visual impact. The fact that the depth of the initial well shape has increase with the increase in g_e, indicates that, together, $\mathbf{V}_2$ and $\mathbf{V}_4$ have increased and $\mathbf{V}_0$ has decreased.

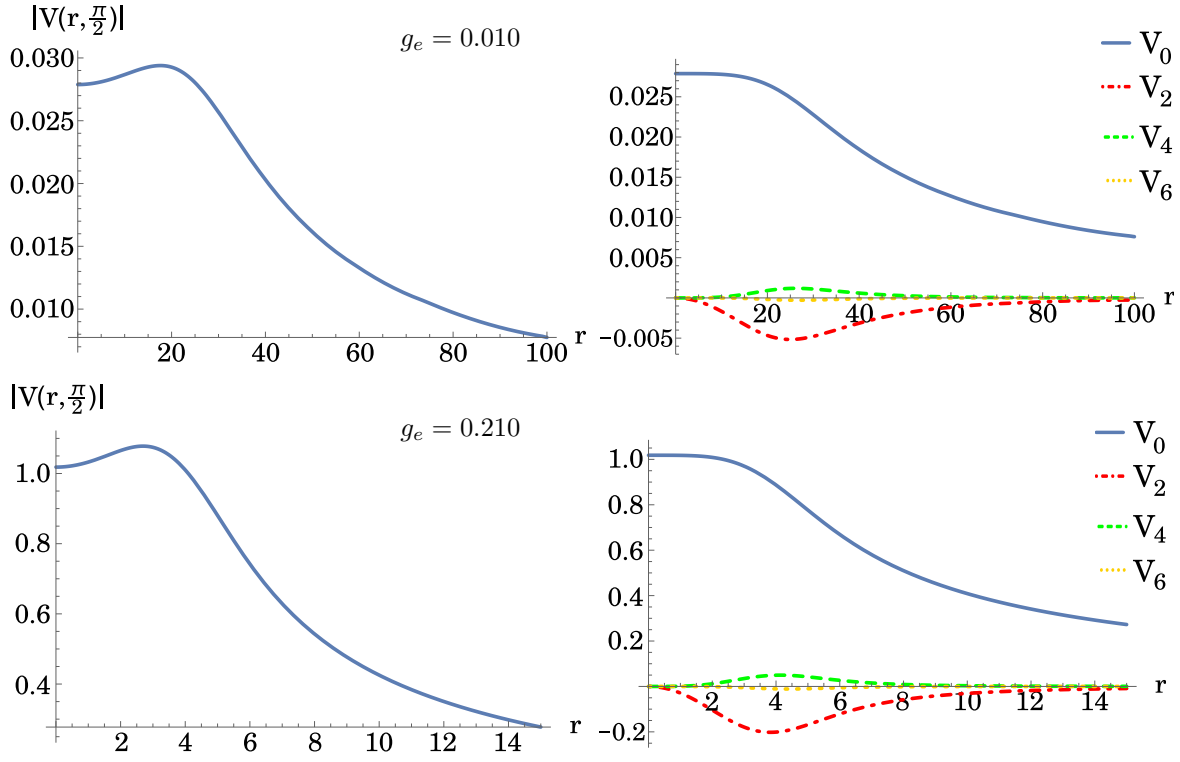

Figure 2.22: Electric potential V for $\omega_3 = 0.999$ and (top) $g_e = 0.010$; (bottom) $g_e = 0.210$. (Left) electric potential amplitude $\left|V(r, \frac{\pi}{2})\right|$; (right) first four multipolar functions $\mathbf{V}_l$ as a function of r.

After decomposing V into the multipolar functions ($\mathbf{V}_l$), one can perform a comparative analyses of the 2D and 3D behavior between, the numerically obtained and the decomposed V. To do that, let us first analyze the 2D representation of V, the equipotential lines and electric field $\vec{E}$. In Fig. 2.23 is presented a cut along the z-axis ($\phi = c^{te.}$) of the latter's in two different scales. In Fig. 2.23 (left), for $z < 0$, is presented the numerically obtained V, while for $z > 0$, is the multipolar decomposited V, with the first four $\mathbf{V}_l$. Remember that the outer blue region is not placed as a high electric potential, but as contrast to the yellow region.

As before, for large distances, both the equipotential lines, the electric field and the electric potential tend to the ones obtained through an electric monopole, observe Fig. 2.23 (bottom right). The electric field lines tend to become purely radial while the equipotential lines, as well as the V, tend to be circular. On the other hand, with the decrease in r a more complex structure emerges.

In relation to the shape of V, besides the change in the radial scale, no noticeable alteration in its form occurs, it still has the same "peanut" shape that comes from the contribution of $\mathbf{V}_2$.

Related with the $g_e = 0.010$ case is Fig. 2.23 (top right). This time, since the optimal scale to observe the generality of the 2D behavior is very large ($r \in [0, 100]$), one can instead of performing a zoom out, perform a zoom in. In it, one can study in more detail the internal electric potential, equipotential lines and electric field. Observe that for small distances, the latter's possess a more complex structure than a monopole, being possible to distinguish between three regions of high V: at the center, and two symmetric offset regions in the xy-plane.

If we take a closer look at the offset regions, one observes that all the electric field lines come from it, this 3D toroidal region – Fig. 2.24 (right) – corresponds to the well in the radial cut of V, Fig. 2.23. At $r = 0$ the electric potential is high and possess a value $V(0)$, it then increases and reaches the maximum $|V_{max}|$ at the center of the offset regions. In the latter, the V is at it maximum and the electric field lines seem to come from it. Due to these two highly electrical charged regions, from the interactive repulsion a zone in between is created, this corresponds to the bottom of the well.

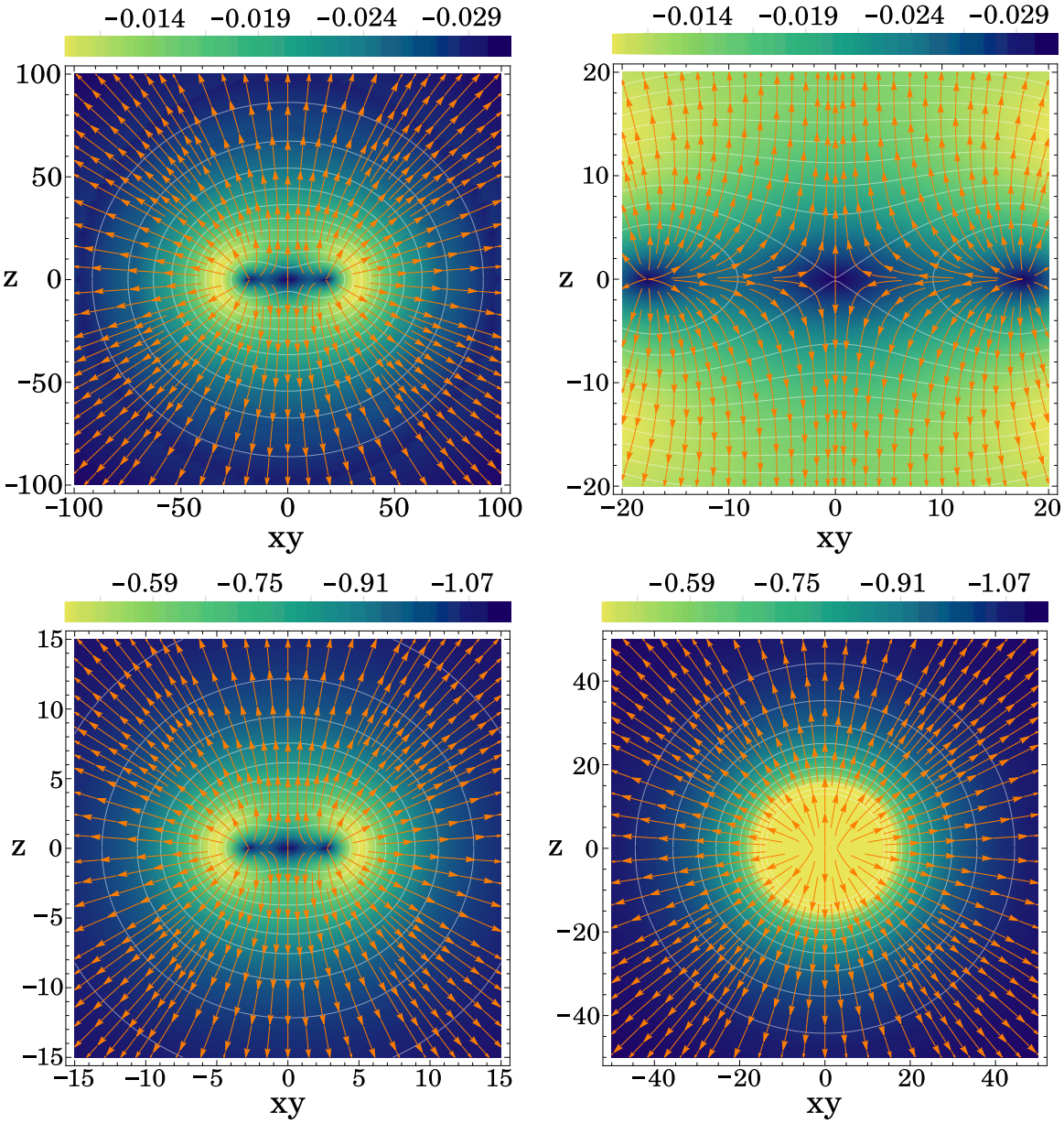

Figure 2.23: Graphical representation of the electric potential (color plot), equipotential lines, and electric field $\vec{E}$ lines for $\omega_3 = 0.999$ and (top) $g_e = 0.010$; (bottom) $g_e = 0.210$. (Left) composed graphic with the multipolar decomposition in the positive z-axis, and the numeric V in the negative z-axis. (Right) Zoom out of the numeric V. Outer blue region placed as contrast.

For the $g_e = 0.210$ value, the intensity of the electric potential has increased in the peak, and the well is now deeper. Even so, the width of the peak has decreased, meaning a higher electric potential in a smaller region. This fact, together with presence of a finite width of the bottom of the well, turns the two offset regions smaller. With the decreasing of the width of the maximum, so decreases the repulsive interaction, letting the electric potential at the center to be wider.

Concerning the multipolar decomposition evolution with g_e, one observes a good description of V through the first four multipolar functions. The equipotential lines are continuous at $z = 0$ and the electric potential is symmetric under the reflection in the xy-plane. In relation to the electric field, it still presents a small difference at the corners.

In Fig. 2.24 is shown the 3D graphical representation of two equipotential surfaces (for 50%, blue, and 99%, purple, of $|V_{max}|$) and the electric field $\vec{E}$.

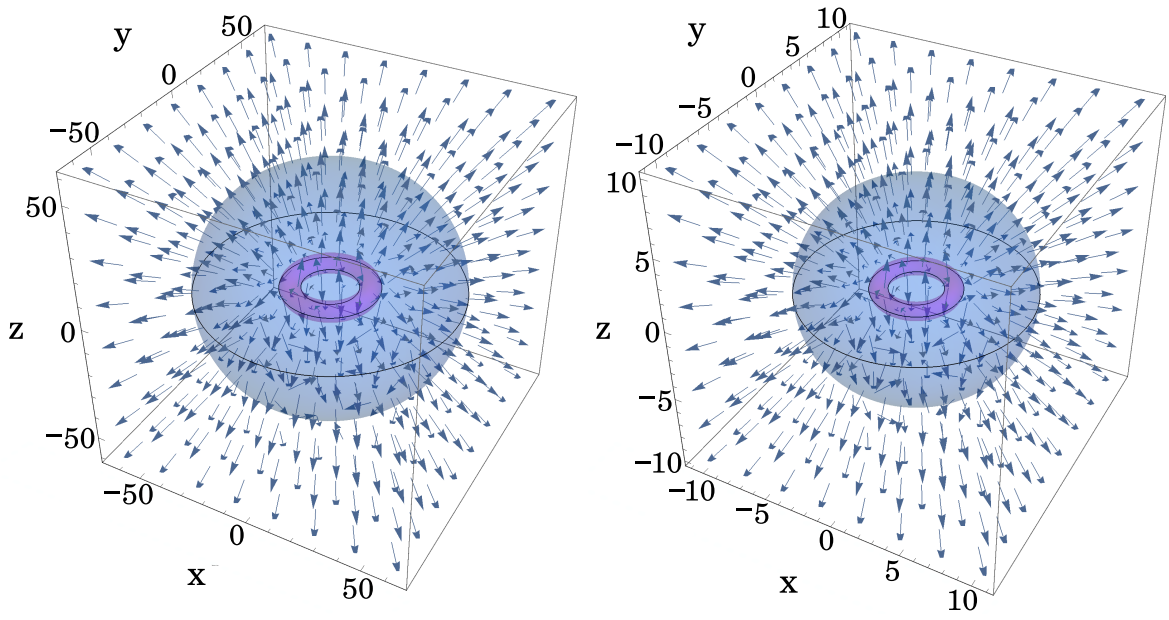

Figure 2.24: 3D graphical representation of the electric field and equipotential surfaces for $\omega_3 = 0.999$ and (right) $g_e = 0.010$; (left) $g_e = 0.210$. The equipotential surfaces represent 50% (blue) and 99% (violet) of $|V_{max}|$.

In the later, it is possible to observe the same shape as before, the large equipotential surface (blue) is almost spherical, while the inner equipotential surface is toroidal. As we observe the 3D representation of V, it is possible to notice that the toroidal shape that corresponds from the 99% of $|V_{max}|$, is increasing its central radius while decreasing its inside radius.

In Fig. 2.25, one can observe magnetic field obtained by the numerical data, for the two g_e values.

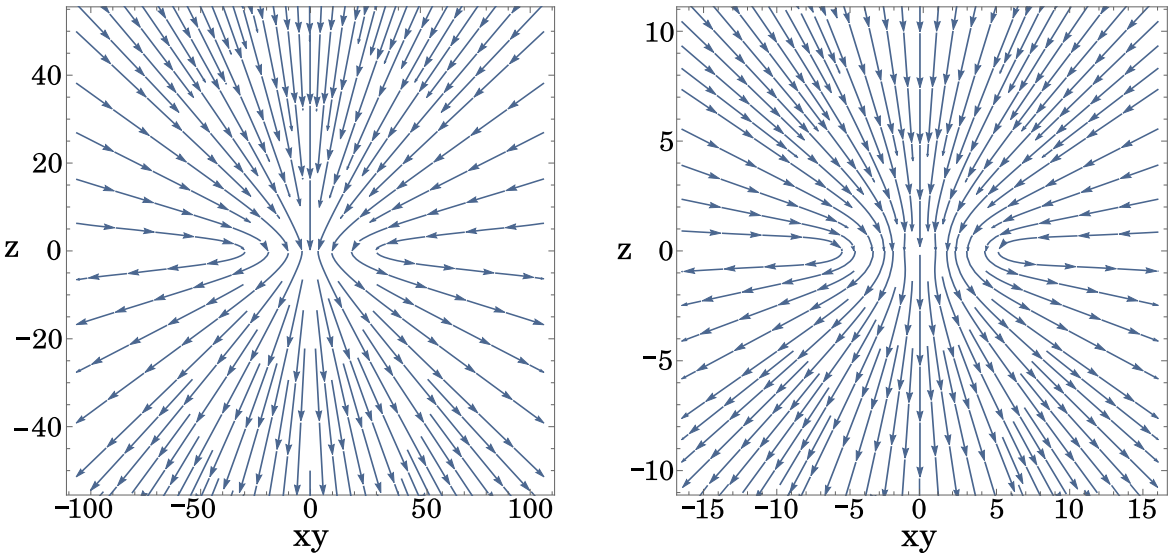

Figure 2.25: Magnetic field representation for $\omega_3 = 0.999$ and (left) $g_e = 0.010$; (right) $g_e = 0.210$.

About $\vec{B}$, note an increase in the compactness of the magnetic field lines with the increase of g_e. Besides that, the magnetic dipole μ_B is -0.3815 for the smaller g_e, and $\mu_B = -2.3305$ for the high $g_e = 0.210$. Such a huge change is mainly originated by the small impact of the $g_e = 0.010$ coupling constant.

Concerning the magnetic quadrupole moment, it is $q_B = 4.0019$ for $g_e = 0.010$ and $q_B = -0.4540$ for the large $g_e = 0.210$. In relation to the former, observe that its value is almost $10\times$ larger than the magnetic dipole moment. Due to the high spatial distribution of the φ (and consequently charge distribution), when one performs the asymptotically decay at the maximum r, it can not be "considered infinity". In other words, at the limit of our radial domain, for $g_e = 0.010$, the magnetic function A_ϕ is still sensing the charge distribution, and a good fit can not be performed.

About the magnetic quadrupole moment for the $g_e = 0.210$, due to the increased compactness, it possesses a much smaller value, Table 2.11. It is $\sim 5.1\times$ smaller than the magnetic dipole, a value pairwise with the previous ω_2 case.

Table 2.11: Characteristic quantities of a(n) (un)gauged, spinning Q-ball with $\omega_3 = 0.999$.

g_e	Q	E	Q_e	μ_B	q_B	γ_B
0.0	1006.0810	1015.6275	0.0	0.0	0.0	0.0
0.010	957.7300	959.2090	-0.7623	-0.4759	4.0019	0.0125
0.210	244.7340	383.8032	-4.0898	-2.3305	-0.4540	0.3039

For the last value of ω a strange behavior occurs. Even that as we increase g_e the maximum amplitude of the scalar field increases, and in this case it increases a lot, the total number of particles decreases. There are more particles, but in a smaller region. The Noether charge has decreased.

As we look to energy, the same behavior occurs, for the larger value of g_e there is a smaller energy. It was pointed out in [21], where a plot for the E *vs.* g_e was performed and an energy decrease was observed.

It is also interesting to notice that the individual particle charge has increased. So, by observing the electric potential plot, one can conclude that there is more charge at the same place, implying a rise in the electrostatic energy. As mentioned before, this relation between the new self-interaction strength and the repulsive electrostatic force, will result in the destruction of the soliton as we increase g_e. Even so, there is a region where this two phenomena stabilize and create an energy minimum.

About the gyromagnetic factor, for the smaller g_e it does not possess significance due to the wrong μ_B value. However for the $g_e = 0.210$ case, it is the biggest so far. It seems that the increase in g_e and ω creates a larger γ_B.

2.5 Solutions with $\omega \geqslant 1.0$

As observed in the previous section (Sec. 2.4.3) there are, for the same ω, gauged spinning Q-balls with a lower energy and Noether charge than the ungauged spinning case, observe Table 2.11. In the latter, the E and Q for the case with $g_e = 0.210$ is $\sim 3.3\times$ smaller than the ungauged case.

For an ungauged, (un)spinning Q-ball, the self-interaction potential – due to the mass μ term – creates a scalar field frequency maximum, ω_+. Recall that, as $\omega \to \omega_+$, the ungauged, (un)spinning Q-ball energy and Noether charge diverges (Sec. 2.2). However, it is observable, that the introduction of g_e creates the possibility of solutions with high values of ω. This raises the possibility to obtain solutions with $\omega \geqslant \omega_+$.

To test this premise, it was obtained two solutions for the gauged spinning Q-ball with $g_e = 0.210$. One of the solutions possesses a scalar field frequency of $\omega = 1.00$, while the other has $\omega = 1.01$. Both greater than any reachable value of ω in the ungauged case.

Let us analise the greatest value, $\omega = 1.01$. Note that, $g_e = 0.210$ is probably not the value of the coupling constant to which a gauged, spinning Q-ball possess its energy minimum. However, since it is the one we studied in ω_3, we will use it. This solution possess $E = 352.6925$ and $Q = 231.6670$, values that are still smaller than the ungauged, spinning case ($g_e = 0.0,\ \omega_3$).

Let us start by the scalar field φ. The latter has a maximum amplitude of $\varphi_{max} = 0.7509$ at $r = 3.5451$, and the profile can be observed in Fig. 2.26.

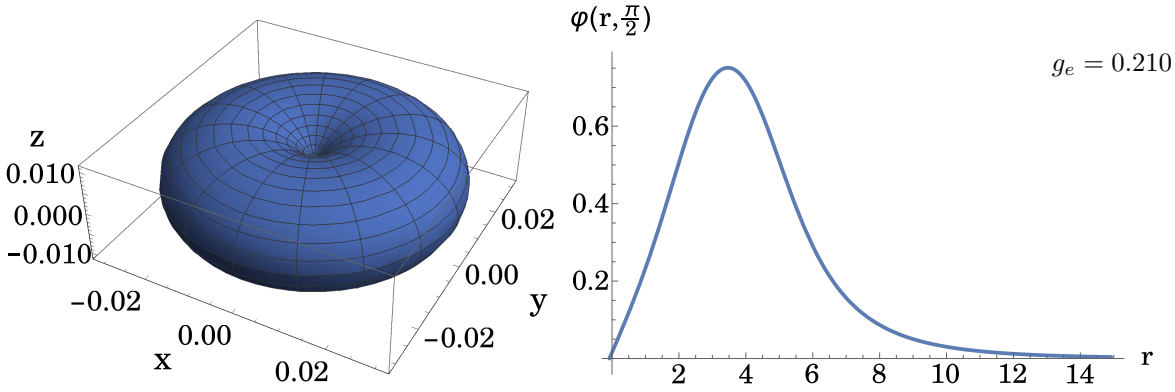

Figure 2.26: Graphical representation of φ for $\omega = 1.01$ and $g_e = 0.210$. (Left panels) 3D graphical representation of φ at $r = 10$ – recall the axial symmetry; (right panels) radial profile with an angular cut at $\theta = \frac{\pi}{2}$.

The shape of φ is still compacter than the ungauged, spinning Q-ball with ω_3. The maximum amplitude is higher and the position where the maximum and the decaying tail are positioned are almost $10\times$ smaller. On the other hand, by comparing with the ω_3 and $g_e = 0.210$ case, one observes a decrease in the compactness. The maximum amplitude has decreased and the peak is now wider.

Such a behavior is easily justified by the increased repulsive interactions from the increased number of electrically charged particles, and the increase in the dispersiveness from the high ω. Even so, it seems that a solution with these g_e and ω parameters is energetically stabler than a high ω ungauged, spinning Q-ball.

To better understand the internal φ, let us decompose the latter into its spectral functions $\mathbf{f}_l$. In Fig. 2.27 is represented the first four spectral functions that decompose, into associated Legendre functions, the scalar field.

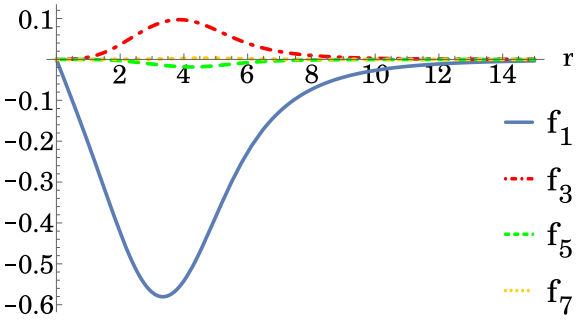

Figure 2.27: Spectral decomposition of the solution with $\omega = 1.01$ and $g_e = 0.210$, into the first four spectral functions $\mathbf{f}_l$.

The $\mathbf{f}_l$ general shape possesses the same behavior as before. $\mathbf{f}_1$ is always negative and is the major contributor to the form of φ. It is then followed by $\mathbf{f}_3$ that takes the second most important role.

To study, in a more quantitative way the impact of each spectral function to the shape of φ, one can calculate the Noether charge contribution of each $\mathbf{f}_l$, Table 2.12.

In comparison with the ω_3 and $g_e = 0.210$ case, the percentage of Q that belongs to the first mode has increased, while the Noether charge from the second has decreased. In the other hand, the Q that comes from the third and fourth function has suffered an increase.

Table 2.12: Relative Noether charge component of $\mathbf{f}_l$, in %, for $\omega = 1.01$ and $g_e = 0.210$.

g_e	$\mathbf{f}_1$	$\mathbf{f}_3$	$\mathbf{f}_5$	$\mathbf{f}_7$	Total
0.210	92.9619	6.6392	0.3803	0.0159	99.9972

Even that the first spectral function component has slightly increased, the total Noether charge coming from the first four spectral functions has decreased. Besides that, the increase in the $\mathbf{f}_1$ component was small. As the soliton evolves to more unstable solutions, less and less part of φ will be associated with $\mathbf{f}_1$. By observing our data it seems that, unstable solutions require and increased amount of spectral functions to be described.

Let us now look at the multipolar decomposition of V, Fig. 2.28. In it, is present an angular cut at $\theta = \frac{\pi}{2}$ of V (left) and the multipolar functions $\mathbf{V}_l$ (right).

For this parameter solutions, the electric potential has $|V_{max}| = 0.9965$ at $r = 2.7682$. The latter is then smaller than the lower ω counterpart. However, taking into account that the related scalar field is also lower, it is easily understood that, even with a higher amount of scalar charged particles (Noether charge), these are not as compacted as before.

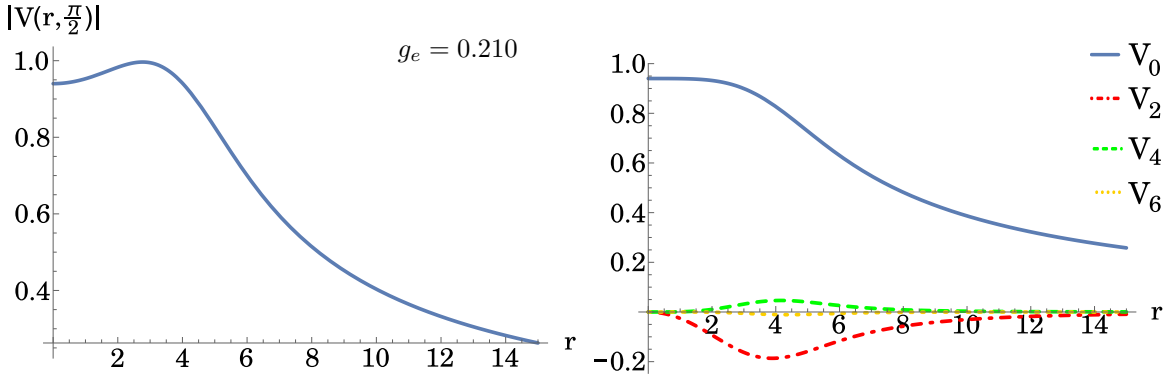

Figure 2.28: Electric potential V for $\omega = 1.01$ and $g_e = 0.210$. (Left) electric potential amplitude $\left|V(r, \frac{\pi}{2})\right|$; (right) first four multipolar functions $\mathbf{V}_l$ as a function of r.

In relation to the form of the electric potential and the multipolar functions $\mathbf{V}_l$, the same shape as before occurs. For V there is an initial well, it reaches its highest value and then decays. For this parameter values the top of the well corresponds to $\sim 1.05\times\ V(0)$, which represents a decrease in the relative high of the peak in comparison to the ω_3 counterpart.

As always, the major components for the shape of φ are $\mathbf{V}_0$ and $\mathbf{V}_2$. The latter together with $\mathbf{V}_4$, creates the top of the well.

After performing the multipolar decomposition, we can compare between the numeric and the multipolar decomposed V. In Fig. 2.29 is graphically represented, in a 2D (left), a cut along z-axis ($\phi = c^{te.}$) of V, where for $z > 0$ is the one obtained through the multipolar decomposition, and for $z < 0$ through the numerical FORTRAN code. On Fig. 2.29 (right) is graphically represented, in 3D, two equipotential surfaces (at blue 50% and at purple 99% of $|V_{max}|$) and the electric field lines.

Note that the outer blue region in Fig. 2.29 (left) is not placed as a high electric potential, but as contrast to the yellow region.

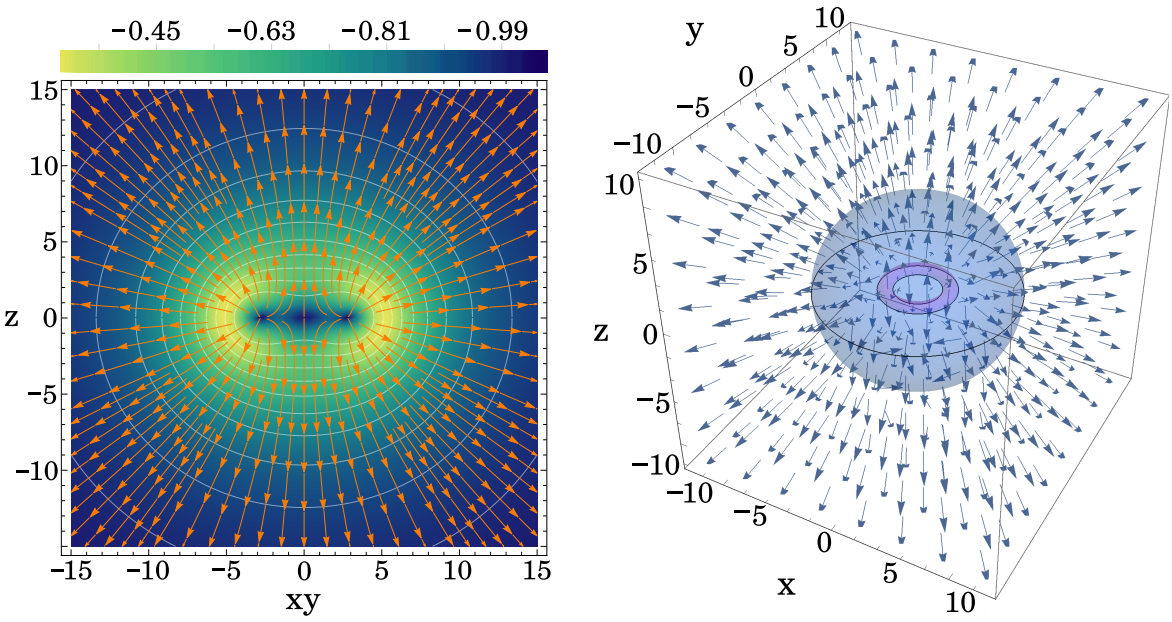

Figure 2.29: Graphical representation of the scalar field gradient, the equipotential lines and the electric field lines for $\omega = 1.01$ and $g_e = 0.210$. (Left) composed plot, the positive z value are obtained with the multipolar decomposition while the negative z values are obtained by V. Outer blue region placed as contrast. (Right) 3D graphical representation of the electric field and two equipotential surfaces with 50% of $|V_{max}|$ (blue) and 99% of $|V_{max}|$ (purple).

As for all the studied cases, at large distances the equipotential lines/surfaces tend to circumferences/spheres and the electric field tend to become purely radial, the electric component tends to a monopole configuration.

As one decreases the value of r, it is presented a more complex shape. As before, there are three regions of the space where V is high (at the center and the in-line offset regions). Concerning the central high electric potential region, its size has increased, the bottom of the well is now wider and the peak skinnier. For the small θ values, it is now possible to observe an higher impact of $\mathbf{V}_2$. Due to the increase in its respective amplitude, the quadrupole function can now affect smaller values of $\mathcal{P}_2^0$, resulting in a wider central region.

About the 3D form, Fig. 2.29 (right), it is observable the same shape as before. A small central toroidal shape, this time with an increased central radius and decreased inner radius, and a spherical outer surface.

In Fig. 2.30, one can observe the magnetic field obtained by the numerical data for the gauged, spinning Q-ball solution with $g_e = 0.210$ and $\omega = 1.01$. Again, as one increases r, the magnetic field originated from A_ϕ tends to present a similar shape to a dipole.

In relation to the magnetic moments, one obtains a magnetic dipole moment of $\mu_B = -2.1551$ and a magnetic quadrupole moment of $q_B = -0.4387$. In comparison with the previous ω_3 case, one observes a small decrease in the two magnetic moments. For this ω example one obtains a magnetic quadrupole moment $\sim 4.9\times$ smaller than the magnetic dipole moment. Again in the same level, even that smaller, as the ω_3 case.

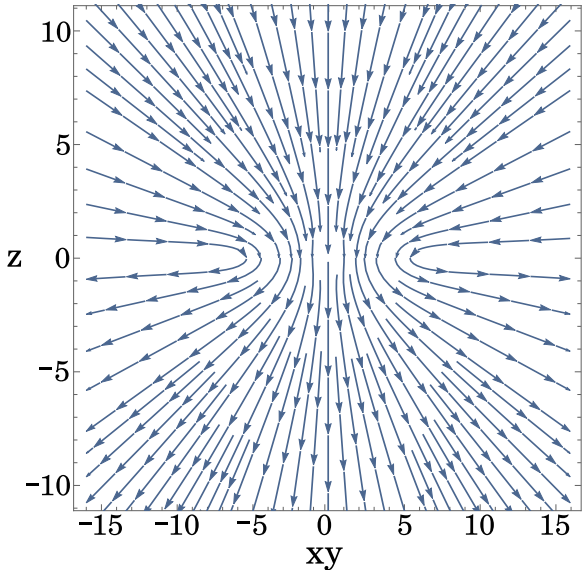

Figure 2.30: Magnetic field representation of $\omega = 1.01$ and $g_e = 0.210$.

Furthermore, in Table 2.13 one observes that, the magnetic dipole moment $\mu_B = -2.1551$ for the same g_e, is smaller than the ω_3.

Table 2.13: Characteristic quantities of a gauged, spinning Q-ball with $\omega = 1.01$ and $g_e = 0.210$.

	Q	E	Q_e	μ_B	q_B	γ_B
$g_e = 0.210$	231.6670	352.6925	−3.8714	−2.1551	−0.4387	0.3551

In relation to the Noether charge and energy reduction, instead of evolving to a stabler configuration this time the Q-ball solution is being affected by the two repulsive behaviors of the scalar and electric fields. With the increase in the scalar frequency ω, the dispersive interactions increase, and the spatial region and scalar field density that the self-interaction potential (U) can support a highly oscillatory solution is decreasing. Such a decrease is then present in the amount of scalar particles that U can hold, resulting in the decrease of the characteristic quantities.

While in the ungauge, spinning Q-ball solutions, the increase in ω originates shallower and diluted solutions, with high values of energy and Noether charge. For a gauged spinning Q-ball one obtains a compact and high scalar field object that the self-interaction potential can not hold at long distances. As one increases ω, the gauged spinning Q-ball tend so suffer an evaporation and to lose particles. At last, in relation to the gyromagnetic factor, it keeps growing, and seems to tend to some limiting value for the last possible ω and g_e parameter solution.

Chapter 3

Boson stars

When gravity is coupled to a scalar field a lump of scalar energy is possible even *without* explicit non-linearities of the scalar field's field theory. Such non-linearities, necessarity to counter balance the dispersive nature of the scalar field are naturally introduced by the non-linear gravitational interaction. In other words, the scalar field "sees" itself due to its self-gravitating energy that curves the spacetime wherein the scalar field lives. These self-gravitating lumps of energy are called *boson stars (BSs)*.

A boson star is an hypothetical astrophysical object, with no observational support so far, that is formed of bosons (while conventional stars are formed with fermions). One possible candidate particle that could yield such stars is the "axion", also a candidate for " non-barionic dark mater" [22].

Historically, the genesis of boson stars can be traced to the work of John Wheeler. In 1955 [23], he investigated the existence, within general relativity (GR) coupled to classical electromagnetism of "*classical, singularity free, exemplar of the "bodies" of classical physics*". He named such (material) source-free entities *geons*, after "**g**ravitational **e**lectr**o**magnetic e**n**titie**s**" and wrote:

> *" The simplest variety is most easily visualized as a standing electromagnetic wave, or beam of light, bent into a closed circular toroid of high energy concentration. It is held in this form by the gravitational attraction of the mass associated with the field energy itself. It is a self-consistent solution of the problem of coupled electromagnetic and gravitational fields (...)"* [p.512]

Wheeler, however, could not provide a complete solution of the Einstein-Maxwell equations describing geons, which motivated subsequent attempts at obtaining not only electromagnetic (*e.g.* [24, 25]), but also neutrino [26] and purely gravitational geons [27]. In asymptotically flat (electro-)vacuum, such discussion is not fully settled. The dominating view is that no topologically trivial, *stable* geons exist (see *e.g.* [28, 29]).

The original proposal of geons does not require *precise* stationarity. In fact, (electro-)vacuum stationarity, asymptotically flat, everywhere regular configurations are ruled out by classical theorems in GR [30, 31]. But a realization of stationary geons was discovered in the Einstein-Klein-Gordon system [32, 33]. These topologically trivial, localized gravitating scalar solitons: BSs [34, 35].

BSs have a stable branch (against linear perturbations) [36, 37]. Their existence is based on three key properties:

i) the field is composed of standing waves oscillating with some frequency;

ii) there is a confining mechanism for the field;

iii) the energy-momentum tensor is invariant under the timelike Killing vector field.

Property **i)**, realises Wheeler's vision: the energy lump of self-gravitating standing waves. The oscillation originates an effective pressure that counter-acts the tendency for gravitational collapse, within GR – and without resorting to energy conditions violating matter. Mathematically, the explicit harmonic time dependence in the field, evades virial-type arguments that rule out the absence of solitons [31]; such arguments are gravitational extensions of Derrick's theorem in field theory [38, 39].

In Wheeler's vision the standing waves' self-gravity should be enough to create a (sufficiently) stable energy lump. But the limited success with electro-vacuum geons indicates this is insufficient; a confining mechanism is necessary – property **ii)**. For BSs, this mechanism is (typically) the field's mass μ, creating a potential barrier at spatial infinity and gravitationally binding waves with frequency $\omega < \mu$.

Still, these two properties do not suffice to create a *stable* energy lump. Field oscillations generate, via the non-linearities of GR, higher frequency harmonics, which leak towards infinity overcoming the gravitational potential well (and the mass potential barrier). This is explicitly seen in *oscillatons* [40], real scalar field configurations with fundamental oscillation frequency. Property **iii)** prevents this. It is realised, for BSs, by having two standing waves with the same frequency but opposite phases, cancelling out all dynamics at the level of the energy-momentum tensor.

One way in which BSs depart significantly from Wheeler's vision is that they are composed of waves with a *single* frequency – BSs are composed of many coherent modes. Depending on the frequency and on the particular model, there is a discrete set of BS solutions with that frequency, corresponding to a fundamental states of BSs.

Boson stars may have been formed through gravitational collapse in the primordial Universe. At least in theory, a supermassive boson star could exist at the core of a galaxy. Dark matter halos surrounding most galaxies could be gigantic "boson stars" [41].

In this chapter, boson star solutions are constructed and analysed. The ADM mass M (Noether charge Q) *vs.* the scalar field frequency ω phase diagram for the fundamental BS states are constructed. To do that, this chapter is organised as follows: first, the boson star model, respective basic equations and characteristic quantities are obtained in Sec. 3.1. Then the required boundary conditions are imposed, and the numerical method is presented. At last, the obtained numerical results are presented and analysed.

3.1 Model

The Einstein-Klein-Gordon action for a massive scalar field minimally coupled with gravity is given as

$$S = \int d^4x \sqrt{-g} \left[\frac{R}{16\pi} - \frac{1}{2} g^{\alpha\beta} \left(\Phi^*_{,\alpha} \Phi_{,\beta} + \Phi^*_{,\beta} \Phi_{,\alpha} \right) - \mu^2 \Phi^* \Phi \right] , \tag{3.1}$$

where R is the Ricci scalar of the spacetime represented by the metric $g_{\alpha\beta}$ with metric determinant g. The complex scalar field is Φ and possesses a particle mass μ, that is consistent with the $\mathbf{U}(1)$ invariance of the field in the complex plane. Variation of the action (3.1) with respect to the metric and the scalar field leads to the well known Einstein field equations (3.2) and the familiar Klein-Gordon equation (3.3),

$$G_{\alpha\beta} = 8\pi \left[\Phi^*_{,\alpha} \Phi_{,\beta} + \Phi^*_{,\beta} \Phi_{,\alpha} - g_{\alpha\beta} \left(\frac{1}{2} g^{\gamma\sigma} (\Phi^*_{,\gamma} \Phi_{,\sigma} + \Phi^*_{,\sigma} \Phi_{,\gamma}) + \mu^2 \Phi^* \Phi \right) \right] , \tag{3.2}$$

$$\Box \Phi = \mu^2 \Phi \, . \tag{3.3}$$

$G_{\alpha\beta}$ corresponds to the Einstein tensor and $\Box$ to the box operator. Equations (3.2) forms a system of 10 non-linear partial differential equations (PDE) for the space-time metric component $g_{\alpha\beta}$ coupled to the scalar field via the stress-energy tensor

$$T_{\alpha\beta} = \frac{1}{2} (\Phi^*_{,\alpha} \Phi_{,\beta} + \Phi^*_{,\beta} \Phi_{,\alpha}) - \frac{g_{\alpha\beta}}{2} \left[g^{\gamma\sigma} (\Phi^*_{,\gamma} \Phi_{,\sigma} + \Phi^*_{,\sigma} \Phi_{,\gamma}) + \mu^2 \Phi^* \Phi \right] . \tag{3.4}$$

Before we obtain the characteristic quantities, let us present the general ansatz. For the metric ansatz, one chooses the spherically symmetric solutions with two unknown functions:

$$ds^2 = -N(r) \sigma^2(r) dt^2 + \frac{dr^2}{N(r)} + r^2 (d\theta^2 + \sin^2 \theta d\phi^2) \, , \tag{3.5}$$

with $N(r) \equiv 1 - \frac{2m(r)}{r}$, being $m(r)$ the space-time ADM mass, *mass function*, and $\sigma(r)$ the *metric function*. For the scalar field, the key is to assume an harmonic ansatz,

$$\Phi(r,t) = \varphi(r) e^{-i\omega t} \ , \tag{3.6}$$

Due to the action invariance under the $\mathbf{U}(1)$ global symmetry $\Phi \to \Phi e^{i\alpha}$, which leads to a conserved Noether current $j_\alpha = -i(\Phi^* \partial_\alpha \Phi - \Phi \partial_\alpha \Phi^*)$. The spatial integration of the time component of j^α, gives arise to the conserved Noether charge Q,

$$Q = \int d^3x \ j_0 \ = 8\pi\omega \int_0^\infty dr\, r^2 \frac{\varphi^2}{N\sigma} \ , \tag{3.7}$$

where $\varphi(r)$ is a real scalar function that corresponds to the radial profile of the star and ω is the scalar field frequency. Note that Φ is a complex scalar field, and hence, the Lagrangian $\left(\mathcal{L} = -g^{\alpha\beta}\Phi^*_{,\alpha}\Phi_{,\beta} - \mu^2\Phi^*\Phi\right)$ is equivalent to a model with two real scalar fields $\Phi = \Phi^R + i\Phi^I$, where Φ^R and Φ^I are real scalar fields. From the two real scalars viewpoint, they are both time periodic but have opposite phases. The time dependence cancels at the level of the energy momentum tensor, being therefore compatible with a stationary metric. Thus $k \equiv \partial/\partial_t$ is a Killing vector field, but it does not preserve the scalar field – the metric and the matter field do not share the same symmetries.

The energy density measured by a static observer $\rho = -T^t_t$, comes as

$$\rho = N(\varphi')^2 + \left(\mu^2 + \frac{\omega^2}{N\sigma^2}\right) \ . \tag{3.8}$$

With the ansatz for the scalar field (3.6) and for the metric (3.5), one can extremize the action (3.1) and obtain a system of coupled Einstein-matter ordinary differential equations (ODEs). The latter, due to the current ansatz, simplifies (compared with other choices as isotropic coordinates), and give the two "essential" Einstein equations:

$$m' = 4\pi r^2 \left(N(\varphi')^2 + \mu^2\varphi^2 + \frac{\omega^2\varphi^2}{N\sigma^2}\right) \ , \tag{3.9}$$

$$\sigma' = 8\pi\sigma r \left((\varphi')^2 + \frac{\omega^2\varphi^2}{N^2\sigma^2}\right) \ . \tag{3.10}$$

The Klein-Gordon equation with a simple mass term completes the required three equations,

$$\varphi'' = -\frac{2\varphi'}{r} - \frac{N'\varphi'}{N} - \frac{\sigma'\varphi'}{\sigma} + \frac{\mu^2\varphi}{N} - \frac{\omega^2\varphi}{N^2\sigma^2} \ . \tag{3.11}$$

3.2 Boson star solution

3.2.1 Boundary conditions and numerical method

The solution for the three coupled ordinary differential equations (ODEs) can be obtained numerically after imposing suitable boundary conditions. At the origin, the unknown functions are:

$$m(0) = 0 \ , \qquad \sigma(0) = \sigma_0 \ , \qquad \varphi(0) = \varphi_0 \ , \tag{3.12}$$

while at the infinity one imposes

$$m(\infty) = M \ , \qquad \sigma(\infty) = 1 \ , \qquad \varphi(\infty) = 0 \ , \tag{3.13}$$

with $\sigma(0)$ and M fixed by the numerics. The above condition for the metric function σ fixes the symmetry of scale invariance $\{\sigma, \omega\} \to \lambda\{\sigma, \omega\}$, with λ a positive constant. Concerning the asymptotic scalar field condition, the latter is used to guarantee the asymptotic flatness and finite energy condition.

Additionally, an analysis of the field equations near the origin leads to an extra condition for the scalar field,

$$\left.\frac{d\varphi(r)}{dr}\right|_{r=0} = 0 \ , \tag{3.14}$$

To numerically solve the set of coupled ODE's, a standard Runge-Kutta method is used [42]. The latter consists on a stable 4^{th} order algorithm, meaning that the local truncation error is on the order $\mathcal{O}(h^5)$, while the total accumulated error is of the order of $\mathcal{O}(h^4)$, where h is the step size. With the 4^{th} *order Runge-Kutta method (RK4)* one can in a, stable calculation, solve a set of ODEs with the desire precision (for this work $h = 10^{-4}$ meaning an accumulated error of $\sim 10^{-16}$).

This Runge-Kutta algorithm uses a generic point (k) and an estimate inclination to numerically integrate the next point $(k+1)$. This estimate inclination results from the weighted average of four increments between the point k and $k+1$. Each increment is the product of the size of the interval, h, and an estimated slope specified by the right-hand of the ODE to integrate (3.9)-(3.11).

To numerical solve the set of ODEs (3.9)-(3.11) with the RK4 method, one has to insert the initial conditions and the correspondent derivative values for the inclination estimation. Concerning the latter, to have a good estimative, the inclination will have to be calculated in three sub-points (four increments counting with the initial point derivative) between the initial position $(k = 0)$ and the first point $(k = 1)$. To obtain them one can find a power series solution of the field equations near the origin:

$$m(r) \simeq \frac{4\pi\left(\mu^2\sigma_0^2+\omega^2\right)}{3\sigma_0}\varphi_0^2\, r^3 + \mathcal{O}(r^5) \ , \tag{3.15}$$

$$\sigma(r) \simeq \sigma_0 + \frac{4\pi\omega\varphi^2}{\sigma_0} r^2 + \mathcal{O}(r^4) \ , \tag{3.16}$$

$$\varphi(r) \simeq \varphi_0 + \frac{1}{6}\left(\mu^2 - \frac{\omega^2}{\sigma_0^2}\right)\varphi_0 r^2 + \mathcal{O}(r^4) \ . \tag{3.17}$$

Then, one integrates the coupled ODEs with the RK4 solver, with the input parameters φ_0, ω, and σ_0. Each BS solution is defined by two parameters (ω, n). For a given scalar field frequency, the solution forms a discrete set indexed by the number of nodes n, of the matter function. Here we shall mostly discuss the *fundamental mode* $n = 0$, except in Fig. 3.2.

Note that the resolution of the coupled ODEs by the RK4 method is only initial conditions dependent. So, to ensure that the asymptotic conditions are fulfilled, one relies on a shooting method [42]. With the latter, at the level of machine precision, the scalar field value vanishes at some large r, (3.13). The shooting method is implemented in terms of the scalar field amplitude at the origin φ_0, for fixed ω and $\sigma_0 = 1$. This is actually a 1-parameter shooting, with shooting parameter φ_0.

To perform the shooting method one fixes all the initial parameters and integrates with the RK4 method until some large radius r_{max}. At r_{max}, one compares the obtained value of the scalar field $\varphi(r_{max})$ with the condition at infinity (3.13). If, to machine precision, the value of $\varphi(r_{max})$ fulfills the condition (3.13) the initial parameters are parameter solutions of a BS and one can try to find the next set of parameter solutions. If $\varphi(r_{max})$ does not fulfill the asymptotic condition (3.13), then the initial scalar field parameter is changed and the process is repeated. By obtaining a set of BS solution parameters one can then follow the change of the latter's and obtain all the desired BS solutions.

At some large value of r, $\varphi(r_{max}) = 0$, to machine precision, but $\sigma(r_{max}) = \sigma_{fin} \neq 1$. But there is a scaling symmetry of the field equations ($\sigma \to \sigma/\lambda$, $\omega \to \omega/\lambda$) that maps the solution to another ω and $\sigma(r_{max}) = 1$.

One can find various (or none) solutions, corresponding to different ADM masses M, for the same number of nodes and for a given frequency.

3.2.2 Numerical results

The solutions obtained are, in all cases, topologically trivial, with $0 \leqslant r < \infty$. They possess no horizon, while the size of the $\mathcal{S}^2$-sector of the metric shrinking to zero as $r \to 0$, *cf.* (3.5). The

latter limit is just the standard coordinate singularity of spherical coordinates. Indeed, solutions are everywhere regular and asymptotically flat.

The domain of existence of the solutions corresponds to a spiral in an ADM mass M (and Noether charge Q) *vs.* frequency ω, diagram, starting from $M = 0$ for $\omega = \mu = 1$, in which limit the field becomes very diluted and the solution trivializes, Fig. 3.1 (left). At some intermediate frequency, a maximal mass is attained. These masses and corresponding frequencies are given in the second and third columns of Table 3.1.

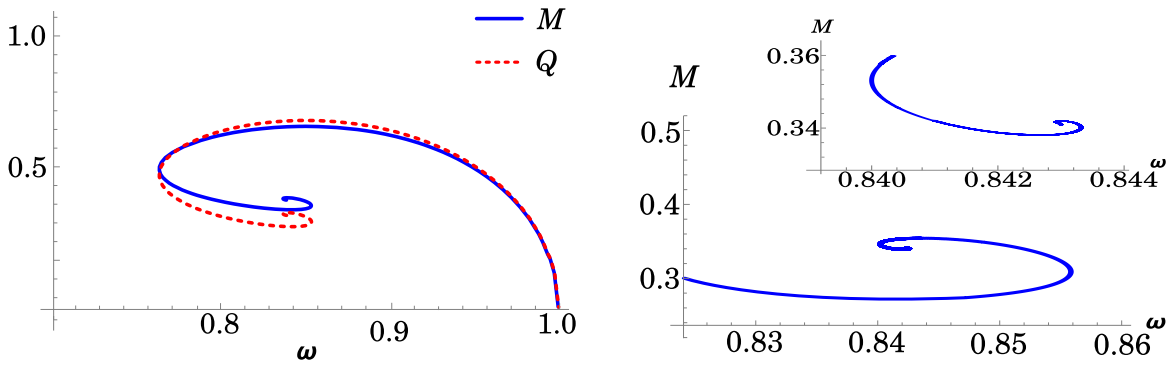

Figure 3.1: (Left) The ADM mass M (blue line) and the Noether charge Q (red dash) *vs.* field frequency ω for the minimal scalar field. (Right) Zoom in of the ingoing spiral in the M *vs.* ω.

Note that all the excited states of a BS, possess a lower initial amplitude $\varphi_0^{exc.}$ than the fundamental mode φ_0, however, due to the presence of subsequent peaks, both the ADM mass and the Noether charge are going to be greater for the excited states than for the fundamental states. In Fig. 3.2 (right) it is observable a boson star excited state with 7 visible nodes. The exact number of nodes is difficult to estimate, since the peaks most further away (in radius) possess a small amplitude.

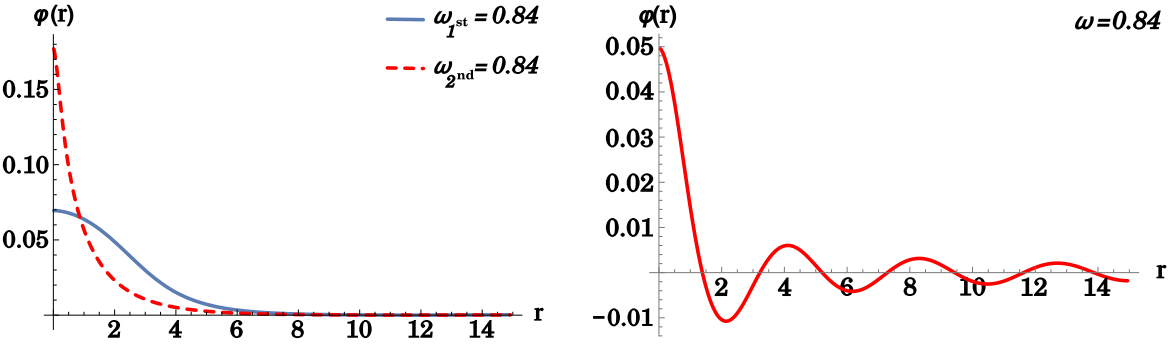

Figure 3.2: Graphical representation of φ. (Left) Two Boson star fundamental modes with the same scalar field frequency ω, where $\omega_{1^{st}}$ to a solution obtained in the first branch – starting at $\omega = 1$ – and $\omega_{2^{nd}}$ to a BS solution obtained in the second branch – after the first backbending. (Right) excited BS state with $\omega_{1^{st}} = 0.84$ with 7 visible nodes.

Besides the maximum mass, there is also a minimum frequency, below which no solution is found, $\omega_{min} \approx 0.767\mu$. At this point, the spiral backbends into a second branch, after which it evolves until a new backbending. In our numeric calculations, we were able to obtain further backbendings and branches. The frequencies of the first (minimal frequency), second and third backbendings are shown in Table 3.1. Likely, these spirals approach, at their center, a critical singular solution. However, as one progresses in the ingoing spiral, the BS gets more and more compact, increasing the scalar field gradients which in turn requires additional integration steps and machine precision. We have not been

able to follow the spiral that far.

Table 3.1: Second to fourth columns: frequencies of the first (minimal frequency), second and third backbending in the M*vs.* ω diagram of Fig. 3.1 (left). All quantities are present in units of μ.

$M^{\max}$	$\omega(M^{\max})$	$\omega_{1^{\rm st}}$	$\omega_{2^{\rm nd}}$	$\omega_{3^{\rm rd}}$	$M=Q$	ω_{crit}
0.633	0.853	0.768	0.856	0.840	0.552	0.778

Concerning the maximum ADM mass M, the latter depends solely on the scalar field mass μ and is of the form [32]

$$M_{max} = \alpha_0 \times 10^{-19} M_\odot \left(\frac{GeV}{\mu}\right) , \tag{3.18}$$

with $\alpha_0 \simeq 0.633$. Thus, only ultra light bosons, with mass $\mu \lesssim 10^{-19}\ GeV$, can source stellar mass BSs. These occur in a variety of "beyond the Standard Model" scenarios, most notably in the string axiverse [43].

How can a single frequency state, with ultra-light boson mass create star-like objects? Because it has a very large occupation number, which can be estimated by computing the Noether charge (Q) associated to the $\mathbf{U}(1)$ global symmetry of the scalar model, that rotates the two modes. Upon quantization, this becomes an integer. Along with the spiral line of Fig. 3.1 (left) the occupation number varies similarly to the ADM mass, Fig. 3.1 (right). At its maximum, taking (say) $\mu \sim 10^{-19}\ GeV$, implies a large number the order of $Q \sim 10^{76}$. Macroscopic BSs are therefore macroscopic quantum states, indeed macroscopic Bose-Einstein condensates.

Observe that the Noether charge Q is a measure of particle number. As such, it can also give us a criterion for stability. If the Noether charge multiplied by the quanta mass μ is smaller than the ADM mass M, then the solution has excess energy and it should be unstable against fission. For a Boson star, close to the maximal frequency, $\omega = \mu$, the solution possess a Noether charge larger than the ADM mass (in units of μ). This corresponds to a regime where there is biding energy, a necessary, albeit not sufficient condition for stability. At some critical point ω_{crit}, however, the Noether charge and ADM mass curve cross and M becomes larger than Q, corresponding to solutions with excess energy and hence unstable. The crossing frequency, and corresponding $M = Q$ are given in the seventh and eight columns of Table 3.1.

At last, returning to a more fundamental level, in Wheeler's vision, the concept of geon "*completes the scheme of classical physics by providing for the first time an acceptable classical theory of the concept of body*" [p.536], but "*one's interest in following geons into quantum domain will depend upon one's view of the relation between very small geons and elementary particles*" [p.512]. The prevailing view, at present, is that the classical GR geometric picture is inadequate for the quantum world, where quantum fluctuations are of the order of the space-time metric. Moreover, there are no doubts that a successful description of elementary particles has been provided by Quantum Field Theory. But one may not exclude that a more conceptually fulfilling, likely complementary, description of a single particle is possible. In this respect, geons may still have a role to play in bridging the classical and quantum world.

Chapter 4

Conclusion

Throughout this thesis, one has performed a Q-ball spectroscopy, and a boson star construction. In relation to the Q-ball chapter, the spectral, multipolar and asymptotic decomposition of the scalar field, the electric potential and the magnetic field (respectively) was demonstrated and tested. The tests demonstrate the power of these techniques to separate the angular and radial coordinate dependency into two independent functions, and by being able to recover the shape and characteristic quantities of each field. The spectral and multipolar decomposition have been able to achieve an accuracy $\sim 10^{-3}$ with just four terms.

For the scalar field, a spectral decomposition – decomposition into associated Legendre functions with $m = 1$ and l odd – was performed. With the spectral functions, the internal scalar field distribution was studied. Concerning the spectral functions contribution, one finds, consistently, that the majority of the energy and Noether charge are associated with the first ($\sim 95\%$) and the second ($\sim 5\%$) spectral functions. Concerning the energy contribution, there is a part that comes from the coupling between different spectral modes. This coupling seems to decrease as ω tends to the extremes.

For the electric field, a multipolar decomposition – decomposition into associated Legendre functions with $m = 0$ and l even – was made. With the multipolar functions obtained from the decomposition it was possible to decompose and analyse the modes that form the electric potential. It was observed that, the monopole term is the major contributor for the general shape of the electric potential, while the quadrupole function is the main responsible for the internal charge distribution. Concerning the magnetic field an asymptotic decay study was performed. With the latter was possible to obtain the magnetic dipole moment and the magnetic quadrupole moment. Even that we have been able to obtain the electric field multipoles and the magnetic field decay, no energy coupling study was performed. However, after performing the vectorial multipolar decomposition, such a study is possible and can give a better insight of the relations between the three fields that constitute a Q-ball.

For the solutions under study, one was able to obtain the gyromagnetic factor. For the latter, it was not possible to achieve an asymptotic value, however, a tendency to increase with the gauge coupling constant was present. That, together with the ability to obtain a gauged, spinning Q-ball solution with scalar field frequency greater than the particles mass, creates the possibility to achieve and analyse the extremal parameters solution.

In the second part of this thesis, through a written C language code, a fundamental state boson star was constructed and the phase parameter diagram obtained. In the latter an inward spiral was obtained. This inward spiral seems to converge to a single point, however, due to the computational limitations such a point was not achieved. In the inward spiral three backbendings haven been obtained, as well as the critical frequency for which the energy and the Noether charge match. An excited boson star state with seven visible nodes was also possible to be obtained. For the latter solution, the phase diagram was not obtained, being part of a future work.

In [1], it was presented the fundamental state phase diagram for the boson star (with null spin), and two extra solutions. The bosonic object with particle spin-1, the Proca star, and a fermionic object with particle spin-$\frac{1}{2}$, a Dirac star. For these exotic stars, a brief presentation of the solutions was made, opening the door for future research.

Appendix A

Associated Legendre Functions

Utilized associated Legendre functions:

$$\mathcal{P}_0^0(\cos\theta) = 1 \ , \tag{A.1}$$

$$\mathcal{P}_1^1(\cos\theta) = -\sin\theta \ , \tag{A.2}$$

$$\mathcal{P}_2^0(\cos\theta) = \frac{1}{2}\left(3\cos^2\theta - 1\right) \ , \tag{A.3}$$

$$\mathcal{P}_3^1(\cos\theta) = -\frac{3}{2}\sin\theta\left(5\cos^2\theta - 1\right) \ , \tag{A.4}$$

$$\mathcal{P}_4^0(\cos\theta) = \frac{1}{8}\left(35\cos^4\theta - 30\cos^2\theta + 3\right) \ , \tag{A.5}$$

$$\mathcal{P}_5^1(\cos\theta) = -\frac{15}{8}\sin\theta\left(21\cos^4\theta - 14\cos^2\theta + 1\right) \ , \tag{A.6}$$

$$\mathcal{P}_6^0(\cos\theta) = \frac{1}{16}\left(231\cos^6\theta - 315\cos^4\theta + 105\cos^2\theta - 5\right) \ , \tag{A.7}$$

$$\mathcal{P}_7^1(\cos\theta) = -\frac{7}{16}\sin\theta\left(429\cos^6\theta - 495\cos^4\theta + 135\cos^2\theta - 5\right) \ , \tag{A.8}$$

$$\mathcal{P}_8^0(\cos\theta) = \frac{1}{128}\left(35 - 1260\cos^2\theta + 6930\cos^4\theta - 12012\cos^6\theta + 6435\cos^8\theta\right) \ , \tag{A.9}$$

$$\mathcal{P}_9^1(\cos\theta) = -\frac{45}{128}\sqrt{1-\cos^2\theta}\left(7 - 308\cos^2\theta + 2002\cos^4\theta - 4004\cos^6\theta + 2431\cos^8\theta\right) \ , \tag{A.10}$$

$$\mathcal{P}_{10}^0(\cos\theta) = \frac{1}{256}\Big[-63 + 3465\cos^2\theta + 143\cos^4\theta\left(-210 + 630\cos^2\theta - 765\cos^4\theta + 323\cos^6\theta\right)\Big] \ , \tag{A.11}$$

$$\mathcal{P}_{11}^1 = -\frac{33}{256}\left(-21 + 1365\cos^2\theta - 13650\cos^4\theta + 46410\cos^6\theta - 62985\cos^8\theta + 29393\cos^{10}\theta\right)\sqrt{\sin^2\theta} \ . \tag{A.12}$$

Bibliography

[1] Carlos A. R. Herdeiro, Alexandre M. Pombo, and Eugen Radu. Asymptotically flat scalar, Dirac and Proca stars: discrete vs. continuous families of solutions. *Accepted in Phys. Lett. B*, 2017.

[2] P. G. Drazin and R. S. Johnson. *Solitons: An Introduction*. Cambridge university press, 1989.

[3] T. H. R. Skyrme. A Nonlinear field theory. *Proc. Roy. Soc. Lond.*, A260:127–138, 1961.

[4] Sidney R. Coleman. Q-Balls. *Nucl. Phys.*, B262:263, 1985. [Erratum: Nucl. Phys.B269,744(1986)].

[5] Joshua A. Frieman, G. B. Gelmini, Marcelo Gleiser, and Edward W. Kolb. Solitogenesis: Primordial Origin of Nontopological Solitons. *Phys. Rev. Lett.*, 60:2101, 1988.

[6] Alexander Kusenko and Mikhail E. Shaposhnikov. Supersymmetric Q-balls as dark matter. *Phys. Lett.*, B418:46–54, 1998.

[7] Richard A Battye and Paul M Sutcliffe. Q-ball dynamics. *Nuclear Physics B*, 590(1-2):329–363, 2000.

[8] Minos Axenides, Stavros Komineas, Leandros Perivolaropoulos, and Manolis Floratos. Dynamics of nontopological solitons: Q-balls. *Physical Review D*, 61(8):085006, 2000.

[9] D. Bazeia, L. Losano, M. A. Marques, and R. Menezes. Split Q-Balls. *Phys. Lett.*, B765:359–364, 2017.

[10] G. R. Dvali, Alexander Kusenko, and Mikhail E. Shaposhnikov. New physics in a nutshell, or Q-ball as a power plant. *Phys. Lett.*, B417:99–106, 1998.

[11] Ki-Myeong Lee, Jaime A. Stein-Schabes, Richard Watkins, and Lawrence M. Widrow. Gauged Q-Balls. *Phys. Rev.*, D39:1665, 1989.

[12] I. E. Gulamov, E. Ya. Nugaev, A. G. Panin, and M. N. Smolyakov. Some properties of U(1) gauged Q-balls. *Phys. Rev.*, D92(4):045011, 2015.

[13] I. E. Gulamov, E. Ya. Nugaev, and M. N. Smolyakov. Theory of U(1) gauged Q-balls revisited. *Phys. Rev.*, D89(8):085006, 2014.

[14] A. G. Panin and M. N. Smolyakov. Problem with classical stability of U(1) gauged Q-balls. *Phys. Rev.*, D95(6):065006, 2017.

[15] Mikhail S. Volkov and Erik Wohnert. Spinning Q-balls. *Phys. Rev.*, D66:085003, 2002.

[16] Tuomas Multamäki and Iiro Vilja. Analytical and numerical properties of Q-balls. *Nuclear Physics B*, 574(1):130–152, 2000.

[17] Francesca Doddato and John McDonald. Dark Matter Gravitinos and Baryons via Q-ball decay in the Gauge-Mediated MSSM. *JCAP*, 1307:004, 2013.

[18] Masahiro Kawasaki and Masaki Yamada. *Q*-ball Decay Rates into Gravitinos and Quarks. *Phys. Rev.*, D87(2):023517, 2013.

[19] M Schauder, R Weiß, and W Schönauer. The CADSOL program package. *Universität Karlsruhe, Interner Bericht*, (46/92):26, 1992.

[20] Willi Schönauer and Torsten Adolph. How we solve PDEs. *Journal of computational and applied mathematics*, 131(1):473–492, 2001.

[21] Eugen Radu and Mikhail S. Volkov. Existence of stationary, non-radiating ring solitons in field theory: knots and vortons. *Phys. Rept.*, 468:101–151, 2008.

[22] Edward W. Kolb and Igor I. Tkachev. Axion miniclusters and Bose stars. *Phys. Rev. Lett.*, 71:3051–3054, 1993.

[23] J. A. Wheeler. Geons. *Phys. Rev.*, 97:511–536, 1955.

[24] Frederick J. Ernst. Linear and Toroidal Geons. *Phys. Rev.*, 105:1665–1670, 1957.

[25] M. A. Melvin. Pure magnetic and electric geons. *Phys. Lett.*, 8:65–70, 1964.

[26] Dieter R. Brill and John A. Wheeler. Interaction of neutrinos and gravitational fields. *Rev. Mod. Phys.*, 29:465–479, 1957.

[27] Dieter R. Brill and James B. Hartle. Method of the Self-Consistent Field in General Relativity and its Application to the Gravitational Geon. *Phys. Rev.*, 135:B271–B278, 1964.

[28] Paul R. Anderson and Dieter R. Brill. Gravitational geons revisited. *Phys. Rev.*, D56:4824–4833, 1997.

[29] G. P. Perry and F. I. Cooperstock. Stability of gravitational and electromagnetic geons. *Class. Quant. Grav.*, 16:1889–1916, 1999.

[30] Albert Einstein and Wolfgang Pauli. On the non-existence of regular stationary solutions of relativistic field equations. *Annals of Mathematics*, pages 131–137, 1943.

[31] Markus Heusler. No hair theorems and black holes with hair. *Helv. Phys. Acta*, 69(4):501–528, 1996.

[32] David J. Kaup. Klein-Gordon Geon. *Phys. Rev.*, 172:1331–1342, 1968.

[33] Remo Ruffini and Silvano Bonazzola. Systems of selfgravitating particles in general relativity and the concept of an equation of state. *Phys. Rev.*, 187:1767–1783, 1969.

[34] F. E. Schunck and E. W. Mielke. General relativistic boson stars. *Class. Quant. Grav.*, 20:R301–R356, 2003.

[35] Steven L. Liebling and Carlos Palenzuela. Dynamical Boson Stars. *Living Rev. Rel.*, 15:6, 2012.

[36] Marcelo Gleiser and Richard Watkins. Gravitational Stability of Scalar Matter. *Nucl. Phys.*, B319:733–746, 1989.

[37] T. D. Lee and Yang Pang. Stability of Mini - Boson Stars. *Nucl. Phys.*, B315:477, 1989. [,129(1988)].

[38] G. H. Derrick. Comments on nonlinear wave equations as models for elementary particles. *J. Math. Phys.*, 5:1252–1254, 1964.

[39] RH Hobart. On the instability of a class of unitary field models. *Proceedings of the Physical Society*, 82(2):201, 1963.

[40] E. Seidel and W. M. Suen. Oscillating soliton stars. *Phys. Rev. Lett.*, 66:1659–1662, 1991.

[41] Jae-weon Lee and In-gyu Koh. Galactic halos as boson stars. *Physical Review D*, 53(4):2236, 1996.

[42] Claes Johnson. *Numerical solution of partial differential equations by the finite element method.* Courier Corporation, 2012.

[43] Asimina Arvanitaki, Savas Dimopoulos, Sergei Dubovsky, Nemanja Kaloper, and John March-Russell. String Axiverse. *Phys. Rev.*, D81:123530, 2010.